## ABSTRACT

## METAL BASED REACTIVE NANOCOMPOSITES PREPARED BY CRYOMILLING

**by**
**Shasha Zhang**

Aluminum is one of the most commonly used metal fuel additives for propellants, explosives, and pyrotechnics. Recent interest has been focused on replacements for aluminum as fuel additives to achieve higher combustion temperatures and stronger pressure pulses for applications in advanced munitions systems. Two applications are addressed in this work. In the applications for explosives designed to defeat stockpiles of chemical and biological weapons, it is of interest to develop multifunctional materials combining the high energy density of metal fuels with the biocidal activity of halogens. A challenge of this effort is to design and prepare powder-like Al-$I_2$ materials which can be used as drop-in replacements for pure aluminum powders in aluminized energetic formulations. For another application, it is desired to tailor combustion dynamics of aluminum in order to fully exploit its high reaction energy by modifying its surface and structure. Hydrocarbons with good volatility and reactivity are selected as additives to composite aluminum-based powders to achieve improved combustion dynamics.

For both applications, mechanical milling offers a scalable and versatile method for modifying aluminum. The mechanical milling-based approach is explored in this effort using milling at the liquid nitrogen temperatures, or cryomilling, which enables mixing aluminum with materials that are unstable or difficult to process at room temperatures. Two types of composite materials are prepared and characterized: Al-$I_2$

and Al-hydrocarbon (where wax, low density polyethylene and cyclooctane were used as different hydrocarbon components).

Powders prepared by cryomilling are evaluated using Thermogravimetry Analysis (TGA), Scanning Electron Microscopy (SEM) and X-Ray Diffraction (XRD). TGA results suggest that iodine is bound to Al, while hydrocarbon is present as a coating on the surface of fine Al grains and composite particles. Very fine, nano-scale particles can be prepared for composites milled at the liquid nitrogen temperature.

Ignition temperatures are determined at heating rates in the range of 2000 - 35000 K/s using an electrically heated filament. Constant volume explosion experiments are used to characterize combustion performance of the produced powders. Materials are fed into an oxygen-acetylene flame to observe their burning characteristics and to measure the combustion temperature. The burn time and temperature as a function of particle size are measured using a single particle combustion measurement. Al-$I_2$ powders are supplied to University of Cincinnati for independent evaluation of the biocidal properties of their combustion products.

Ignition temperatures of the prepared materials are substantially reduced compared to Al. Burn rates for individual particles are comparable or somewhat lower than for pure Al. Combustion temperatures for the prepared composites are close to those of pure Al. Independent tests show that Al-$I_2$ materials added to hydrocarbon flame substantially improve inactivation of the aerosolized biologically viable spores. The experiments show that combustion dynamics of the prepared Al-hydrocarbon composites is improved compared to pure Al powders.

# METAL BASED REACTIVE NANOCOMPOSITES PREPARED BY CRYOMILLING

**by**
**Shasha Zhang**

**A Dissertation**
**Submitted to the Faculty of**
**New Jersey Institute of Technology**
**in Partial Fulfillment of the Requirements for the Degree of**
**Doctor of Philosophy in Chemical Engineering**

**Otto H. York Department of**
**Chemical, Biological and Pharmaceutical Engineering**

**May 2013**

.

**APPROVAL PAGE**

**METAL BASED REACTIVE NANOCOMPOSITES PREPARED BY CRYOMILLING**

**Shasha Zhang**

---

Dr. Edward Dreizin, Thesis Advisor — Date
Professor of Chemical, Biological and Pharmaceutical Engineering, NJIT

---

Dr. Mirko Schoenitz, Committee Member — Date
Research Professor of Chemical, Biological and Pharmaceutical Engineering, NJIT

---

Dr. Suhithi Peiris, Committee Member — Date
Thrust Area Manager, Defense Threat Reduction Agency, VA

---

Dr. Ecevit Bilgili, Committee Member — Date
Assistant Professor of Chemical, Biological and Pharmaceutical Engineering, NJIT

---

Dr. Robert B. Barat, Committee Member — Date
Professor of Chemical, Biological and Pharmaceutical Engineering, NJIT

## BIOGRAPHICAL SKETCH

**Author:** Shasha Zhang

**Degree:** Doctor of Philosophy

**Date:** May 2013

**Undergraduate and Graduate Education:**

- Doctor of Philosophy in Chemical Engineering,
  New Jersey Institute of Technology, Newark, NJ, 2013
- Master of Science in Applied Chemistry,
  Tianjin University, Tianjin, P. R. China, 2008
- Bachelor of Science in Chemical Engineering and Technology,
  Tianjin University, Tianjin, P. R. China, 2006

**Major:** Chemical Engineering

**Presentations and Publications:**

**Journal publications:**

Aly, Y., Zhang, S., Schoenitz, M., Hoffmann, V.K., Dreizin, E.L., "Iodine-containing aluminum-based fuels for enhanced inactivation of bioaerosols", *Combustion and Flame*, submitted, 2013

Nie, H., Zhang, S., Dreizin, E.L., "Identifying Diffusing Species between Al and Water", *International Journal of Hydrogen Energy,* submitted, 2013

Zhang, S., Dreizin, E.L., "On Mechanism of Heterogeneous Oxidation of Aluminum Powders", *Journal of Physical Chemistry C*, submitted, 2013

Zhang, S., Dreizin, E.L., "Nano-structured Aluminum Powders with Modified Protective Surface Layers", *Combustion Science and Technology*, accepted, 2013

Zhang, S., Schoenitz, M., Dreizin, E.L., "Ignition and Combustion of Al-hydrocarbon Composite Reactive Powders", *International Journal of Energetic Materials and Chemical Propulsion,* vol. 11, pp. 353-373, 2012

Grinshpun, S. A., Adhikari, A., Yermakov, M., Reponen, T., Dreizin, E., Schoenitz, M., Hoffmann, V., Zhang, S., "Inactivation of aerosolized Bacillus atrophaeus (BG) endospores and MS2 viruses by combustion of reactive materials", *Environmental Science & Technology*, vol. 46, pp. 7334-7341, 2012

Zhang, S., Badiola, C., Schoenitz, M., Dreizin, E.L., "Oxidation, Ignition, and Combustion of Al·$I_2$ Composite Powders", *Combustion and Flame*, vol. 159, pp. 1980-1986, 2012

Dreizin, E.L., Badiola, C., Zhang, S., Aly, Y., "Particle Combustion Dynamics of Metal-Based Reactive Materials", *International Journal of Energetic Materials and Chemical Propulsion*, vol. 10, pp. 297-319, 2011

Zhang, S., Schoenitz, M., Dreizin, E.L., "Iodine Release, Oxidation, and Ignition of Mechanically Alloyed Al-I Composites", *Journal of Physical Chemistry C*, vol. 114, pp. 19653-19659, 2010

Zhang, S., Schoenitz, M., Dreizin, E.L., "Mechanically alloyed Al-I composite materials", *Journal of Physics and Chemistry of Solids*, vol. 71, pp. 1213-1220, 2010

Zhao, B., Feng, Y., Zhang, S., "Novel Synthesis and Characterization of 1,3-Bis(2-dihydrothiazolyl)thiaalkoxy-p-tert-butylcalix[4]arenes", *Synthetic Communications*, vol. 37, pp. 3479-3484, 2007

**Conference proceedings:**

Zhang, S., Schoenitz, M., Dreizin, E.L., "Nano-Structured Aluminum Powders with Modified Protective Surface Layers", *MRS Fall Meeting Proceedings*, 2012

Zhang, S., Badiola, C., Schoenitz, M., Dreizin, E.L., "Al·$I_2$ Composites as Fuel Additives with Biocidal Combustion Products", *7th US National Technical Meeting of the Combustion Institute*, 2011

Dreizin, E.L., Zhang, S., "Reactive Materials for Enhanced Blast Explosives", *JANNAF paper*, 2011

Zhang, S., Schoenitz, M., Dreizin, E.L., "Metastable Aluminum-based Reactive Composite Materials Prepared by Cryomilling", *50th AIAA Aerospace Sciences*, art. no. AIAA 2012-1130, 2012

Badiola, C., Zhang, S., Gill, R., Dreizin, E.L., "Combustion Rates and Temperatures of Reactive Materials Particles", *49th AIAA Aerospace Sciences*, art. no. AIAA 2011-175, 2011

Zhang, S., Schoenitz, M., Dreizin, E.L., "Mechanically alloyed Al-I composite materials", *48th AIAA Aerospace Sciences,* art. no. AIAA 2010-0618, 2010

**Presentations:**

Zhang, S., Schoenitz, M., Dreizin, E.L., "Nano-Structured Aluminum Powders with Modified Protective Surface Layers", *Material Research Society (MRS) Fall Meeting,* Boston, MA, November 2012

Zhang, S., Dreizin, E.L., "Oxidation Mechanism of Metal Particles Derived from Thermal Analysis", *AIChE Annual Meeting*, Pittsburgh, PA, October 2012

Zhang, S., Schoenitz, M., Dreizin, E.L., "Al-based Reactive Powders with Hydrocarbon-Modified Surface Layers", *Defense Threat Reduction Agent Basic Research Technical Review*, Springfield, VA, July 2012

Zhang, S., Schoenitz, M., Dreizin, E.L., "Ignition and Combustion of Al-hydrocarbon Composite Reactive Powders", *9 International Symposium on Special Topics in Chemical Propulsion (9$^{th}$ ISICP)*, Quebec, Canada, July 2012

Zhang, S., Schoenitz, M., Dreizin, E.L., "Al-based Reactive Powders with Hydrocarbon-Modified Surface Layers", *Gordon Research Conference on Energetic Materials*, West Dover, VT, June 2012

Zhang, S., Schoenitz, M., Dreizin, E.L., "Metastable Aluminum-based Reactive Composite Materials Prepared by Cryomilling", *50$^{th}$ AIAA Aerospace Sciences Meeting,* Nashville, TN, January 2012

Zhang, S., Schoenitz, M., Dreizin, E.L., "Metastable Aluminum-based Reactive Composite Materials Prepared by Cryomilling", *AIAA Region I YPSE Conference*, Laurel, MD, November 2011

Zhang, S., Badiola, C., Schoenitz, M., Dreizin, E.L., "Al·$I_2$ Composites as Fuel Additives with Biocidal Combustion Products", *7$^{th}$ US National Technical Meeting of the Combustion Institute*, Atlanta, GA, March 2011

Zhang, S., Schoenitz, M., Dreizin, E.L., "Al-I Composite as Fuel Additives with Biocidal Combustion Products", *American Institute of Chemical Engineers Annual Meeting,* Salt Lake City, UT, November 2010

Zhang, S., Schoenitz, M., Dreizin, E.L., "Al-I Composite as Fuel Additives with Biocidal Combustion Products", *Gordon Research Conference on Energetic Materials*, Tilton, NH, July 2010

Zhang, S., Schoenitz, M., Dreizin, E.L., "Al-I Composite as Fuel Additives with Biocidal Combustion Products", *Dana Knox Student Research Showcase*, Newark, NJ, April 2010

Zhang, S., Schoenitz, M., Dreizin, E.L., "Mechanically alloyed Al-I composite materials", *48th AIAA Aerospace Sciences Meeting*, Orlando, FL, January 2010

Zhang, S., Schoenitz, M., Dreizin, E.L., "Mechanically alloyed Al-I composite materials", *Defense Threat Reduction Agent (DTRA) Basic Research Technical Review*, Washington, DC, October 2009

To my beloved husband for his love and support

谨以此论文献给我最爱的爸爸，妈妈和弟弟

## ACKNOWLEDGMENT

It is with immense gratitude that I acknowledge my advisor, Dr. Edward Dreizin, whose intelligence, expertise, guidance and support made it possible for me to work on this project. As an advisor, he has not only guided me to achieve a lot of interesting discoveries, but also placed a great deal of trust and freedom in me to realize my interest and goals. As a teacher, he has not only instructed me knowledge, but also influenced me by his optimistic attitude to life. It has been a great pleasure to work with him, and I could not have come so far without the guidance from him.

I also would like to express my gratitude to my co-advisor, Dr. Mirko Schoenitz, for his genuine assistance, valuable advice, and providing me with an excellent atmosphere for doing research. I have learnt a great deal from him, and I feel blessed to have worked with him.

Dr. Suhithi Peiris deserves a special note of praise for her precious advice regarding to the topic of research, and her interest in this project. Without her my research would never have been possible. I would also like to thank other committee members, Dr. Ecevit Bilgili and Dr. Robert B. Barat, for their thoughtful criticism and the fact that they have watched over me as a graduate student.

The research staff and students in the laboratory of Dr. Dreizin are the most dedicated and generous people that I have ever met and I feel honored to have worked with them. Many thanks to Alexandre Ermoline, Vern Hoffmann, Yasmine Aly, Priya Santhanam, Shashank Vummidi, Hongqi Nie, Rayon Williams, Amy Corcoran, Ani Abraham, and my former colleagues Demitrios Stamatis, Carlo Badiola, Ervin Beloni,

Bob Gill, and Stefano Mercati, for helping me with experiment set-up and data collecting, as well as collaborating with me.

I am grateful to our collaborator, Dr. Sergey Grinshpun's group, for collaborating with me on the biocide project and the accomplishment we have achieved together.

I must thank the faculty and staff in the department of chemical engineering, as well as the staff in the office of graduate studies at NJIT for assisting me with the administrative tasks necessary for completing my doctoral program.

Most importantly, I would like to express my sincerest appreciation to my family. The love from them has been my driving force. My dear husband, Bo Shi has always been standing by me supporting me both practically and emotionally. His accompanying means so much to me that I could never be able to express. My parents, Yuxiang Zhang and Li Liu and brother, Yaoyang Zhang have always been believing in me and encouraging me with their best wishes.

I would like to thank my good friends, Bin Lin, Zhong He, Zheng Qian, Huiju Liu, Xiaowei Deng, Jun Zhang and Cheng Yun, who were always willing to help and give their best suggestions. I would feel lonely without them.

Finally, I would take this opportunity to express my acknowledgement to my sponsor, Defense Threat Reduction Agency (DTRA) grant HDTRA-1-08-1-0012, for the financial support.

## TABLE OF CONTENTS

**TABLE OF CONTENTS**
**(Continued)**

**TABLE OF CONTENTS**
**(Continued)**

**TABLE OF CONTENTS**
**(Continued)**

**Chapter** **Page**

## LIST OF TABLES

## LIST OF FIGURES

**LIST OF FIGURES**
**(Continued)**

**Figure** **Page**

## LIST OF FIGURES
## (Continued)

**LIST OF FIGURES**
**(Continued)**

## LIST OF FIGURES
## (Continued)

**Figure** **Page**

## LIST OF FIGURES
## (Continued)

**Figure** **Page**

## LIST OF FIGURES
## (Continued)

**Figure** **Page**

# CHAPTER 1

# INTRODUCTION

## 1.1 Background

Energetic materials (explosives, propellants and pyrotechnics) are used extensively for both civilian and military applications. The most commonly used energetic materials are organic compounds with nitro groups including TNT, RDX, and HMX [1-5]. Exothermic reactions producing $H_2O$ and $CO_2$ as reaction products are rate controlled by chemical kinetics [6, 7], which enables fast ignition and combustion rates for practical applications. However, the amount of energy that such materials can release is relatively low, and combustion temperatures are limited.

Metals, such as Al, Mg, B, Ti, etc. [3, 8, 9], are used as additives in energetic formulations to achieve significant increases in both combustion energy and energy density. Compared to mono-molecular organic compounds, their high gravimetric or volumetric combustion enthalpy enables one to achieve significantly high combustion temperature. However, their potential in many practical situations cannot be fully exploited due to long ignition delays [10] and relatively low burn rate, which is associated with the heterogeneous nature of many relevant reactions. In other words, combustion of metals is commonly accompanied by formation of condensed oxide phases

[11-13]. Therefore, the reaction rates become limited by the mass transport of reagents through such oxides, which is much slower than respective chemical kinetics.

Aluminum as a metal additive has been used and studied most widely because of its low cost, high abundance and high reaction enthalpy ($\Delta H_r$ = 31 kJ/g [14]). Recent work has been focused on modification of micron-sized aluminum powder that is commonly added in both solid propellants and explosives. Of particular interest are efforts aimed to achieve reduced ignition delays, greater reaction rates, and specific desired reaction products. Such efforts include reducing size of aluminum particles [15-18], achieving nanoscale mixing of aluminum and oxidizers [19-22], and producing composite particles with nanoscale structures [23-25].

Replacing mircron-sized aluminum particles with nano-sized [15-18] ones results in an accelerated reaction rate due to an increase in the specific surface of the powder. Additionally, the time required for the particle temperature to increase to a point for self-sustaining combustion is thus reduced. Although the application of nano-aluminum has gained substantial attention, there are some significant concerns associated with its application. Aluminum nanoparticles react with oxygen and moisture readily to produce a 2-6-nm-thick $Al_2O_3$ oxide layer [17, 26]. Due to the high surface to volume ratio of nano-particles, the amount of inactive oxide represents a significant fraction of the mass. Thus, energy density is dramatically reduced. In addition, such small particles become very cohesive and difficult to handle. In most recent work, it is also questioned whether

the benefit from morphology of nano-particles can be fully employed during combustion. It is reported that particles may experience a significant degree of sintering at elevated temperatures, and thus particles can no longer retain their nanometer size [27].

Another approach to improve reaction rate is to produce nano-thermites, which involves nanoscale mixing of aluminum and an oxidizer ($MoO_3$, CuO, and $Fe_2O_3$) [19-22]. Different types of reactive thermites have been reported. Metastable intermolecular composites (MICs) [15, 28, 29] were prepared by physically mixing nanoparticles of aluminum and oxidizer by ultra-sonic agitation. Fully dense nanocomposite materials were synthesized by arrested reactive milling (ARM) [30-32]. Such materials are micron-sized powders, each particle is fully dense and contains reactive components mixed on a scale of ~ 100 nm or less. It is anticipated that a small fraction of active metal is reacted during preparation involving high energy ball milling. For all nano-thermites, research has shown that the enhanced contact between fuel and oxidizer results in extremely fast ignition and combustion rate. However, such materials have intrinsically reduced energy density compared to metal fuel additives because they contain added oxidizer phases.

Ignition and combustion dynamics of aluminum can also be modified by mixing aluminum with other metals or metalloids. Such fine mixing with an aluminum matrix and inclusions of other metals was achieved using mechanical milling [33, 34]. The formation of intermetallic compounds was carefully avoided. Aluminum-based

mechanically alloyed compositions have reaction enthalpies similar to those of the pure aluminum, which is much higher compared to nanocomposite thermites prepared by ARM, having similar powder morphology. The oxidation kinetics leading up to ignition is controlled by kinetics of various phase transformations [35-37] occurring in metastable mechanically milled powders upon their heating. Examples of such transformations include formation of intermetallic phases between Al and such additives as Ti or Mg [23-25]. Alternatively, selective oxidation of such additive as Li [36] can also result in an enhanced ignition of the Al-based material. Combustion rate is also improved, which can be attributed to the addition of more reactive metals, such as Li, Zr, or Mg, and to increase in the surface area of reactive interfaces. In addition, the total energy release can be enhanced by adding boron [8, 38], which possesses greater combustion enthalpy compared to Al.

As a continuation of study on mechanically alloyed Al-metal composites, this work is focused on combining aluminum with non-metallic, volatile materials to produce multi-scale composite structures with customized properties desired for different applications. Mechanical milling, a "top-down" powder processing technique, is employed to produce such multi-scale composites.

In mechanical milling [33, 34], elemental powder mixtures used as starting materials are blended together and then ball-milled. The ball milling typically involves high-energy interactions between milling tools, in which the interaction energy is

dissipated in the powder being processed. Powder particles typically experience repeated processes of flattening, cold welding, fracturing and rewelding, which are caused by the impact force of physical collision between milling media. In the early stage of milling, the particles of the aluminum-based blends are ductile, and tend to weld together to form large flakes with new surface. With continued deformation, large flakes become fragile and fracture into smaller flaky fragments. After milling for a certain length of time, the small fragments tend to be welded into equiaxial agglomerates, while large particles tend to fracture. Consequently, the overall particle size distribution eventually stabilizes, while the structure of the particles is steadily refined. In other words, the inter-layer spacing of the produced composite structures decreases and the number of layers in a particle increases. The products are fully dense, reactive composites powders with a relatively broad particle size distribution, typically in the range of 10-100 μm [30]. Despite the small external surface, the internal mixing takes place at the nanoscale level producing highly developed reactive interfaces between different components. Desired powder size and degree of homogenization between components can be achieved by optimizing a number of variables including type of mill, milling speed, milling time, type and size of the grinding medium, ball-to-powder weight ratio, extent of filling the vial, milling atmosphere, process control agent and milling temperature [34].

This method of preparation of composite powders is readily scalable, and capable to process essentially any combination of reactive components. The prepared composites are generally less expensive than similar compositions produced using alternative, "bottom-up" approaches [39-41].

Typically, ball milling is performed at room temperature, although forced cooling of the milling vials by convection is common in different types of ball mills. It has been established that the milling vial temperature affects significantly the milling dynamics and properties of the products. In particular, lower temperatures result in reduced ductility of the aluminum-based powder blends; thus the flake formation occurs over a shorter period of time and the structures of the produced composites is altered. In order to exploit the effect of temperature, cryomilling or milling at the temperature of liquid nitrogen (77 K) has been investigated for preparation of multiple structural aluminum-based alloys [42-44]. The liquid nitrogen temperatures can be achieved either by adding liquid nitrogen into the milling vial directly or by using it as a cooling agent for the milling vial exterior. It was shown that cryomilling enables one to obtain a higher degree of refinement of both particle and grain sizes [42, 43].

In this effort, cryomilling is used to prepare nanocomposite powders with aluminum as a matrix and inclusions comprising materials which are unstable and volatile at room temperature. Additionally, materials that are mechanically soft and do not form composite structures with metals at room temperatures are explored as potential

inclusions into aluminum matrix. It is expected that their mechanical properties are sufficiently altered by cryogenic temperatures, so that effective formation of nanocomposite structures can be achieved.

## 1.2 Objectives

This work consists of two primary projects for different types of applications of reactive nanocomposite materials. The composite materials and their combustion performance are tailored based on specific requirements and conditions associated with these two applications.

The first part of this work is aimed to design an energetic material for applications in munitions designed to defeat stockpiles of chemical and biological weapons [45-49]. The main practical objective is to inactivate biological microorganisms that can be aerosolized by a blast and thus cause substantial contamination of the surrounding area. Developed reactive materials are expected to serve as potential drop-in replacements for the Al powder in aluminized explosives. When pure aluminum is replaced in reactive formulations, biocidal combustion products would form while the high temperatures and burn rates of aluminized explosive are maintained. Halogens are chosen as target additives to aluminum-based powders. Combustion products containing halogens are expected to be biocidal and effective in inactivation aerosolized viable biological microorganisms. However, halogens are unstable and difficult to handle. It is desired to

stabilize halogens and prepare powder-like reactive materials that could be handled and formulated into energetic compositions using currently accepted practices and protocols. Iodine is favored among all the halogens due to its relative stability. Low temperatures further promote stability of iodine. Thus, one of the objectives of the present study is to prepare a stable material combining aluminum with iodine using mechanical milling at cryogenic temperatures.

After materials synthesis, it is important to confirm that material indeed contains iodine and quantify the produced composition. The approach selected for the material characterization is based on thermal analysis. In particular, differential scanning calorimetry (DSC) or thermo-gravimetric analysis (TGA) will be used. It is also of interest to understand reaction kinetics of iodine release at different temperatures and the correlation between iodine release and oxidation behavior. Furthermore, various ignition and combustion experiments are designed to characterize ignition temperature, combustion rate, combustion temperature, and burn time. It is of utmost importance to optimize material to achieve the greatest possible halogen content while maintaining its stability and reactive characteristics. In addition, effectiveness of the prepared composite material in inactivating spores and bacteria is studied jointly with our collaborators at the University of Cincinnati.

Another objective of this work is to design reactive nanocomposite powders, which can serve as gas generators to improve mixing and combustion efficiency in

turbulent reactive flows. Hydrocarbons are considered as suitable candidate additives due to their volatility and combustibility. Thus, the objective is to prepare Al-hydrocarbon composite powders as potential replacements for aluminum powders. Such materials are expected to improve ignition and increase the energy release rate despite a small reduction in the theoretical combustion enthalpy compared to pure aluminum.

Cryomilling is also used to prepare desired aluminum-hydrocarbon composites in order to solidify the hydrocarbons and enable their embedding into the aluminum matrix. The feasibility of incorporation of hydrocarbon in the powder is investigated by DSC and TGA. In such composites, the aluminum oxide layer protecting the surface of regular aluminum powders is expected to be modified or completely replaced by a new, less protective layer. Therefore, the diffusion resistance to oxidation will be reduced, resulting in further accelerating heterogeneous oxidation and combustion. Combustion rate will be tested using constant volume explosion (CVE) experiments with aerosolized powders. Oxidation and ignition of the prepared materials will be evaluated using customized laboratory experiments. Combustion dynamics will be studied in different oxygenated environments.

# CHAPTER 2

# PREPARATION OF Al-$I_2$ COMPOSITES BY MECHANICAL MILLING

## 2.1 Introduction

In recent decades, mechanical alloying was used to prepare a wide variety of unique compounds for multiple applications [33, 34]. One type of potential application for mechanically alloyed materials includes the use as metallic fuel additives for propellants, explosives, and pyrotechnics [24, 35, 37, 50-52]. Such materials are being developed to tailor the rates of energy release from the burning metal and thus improve performance of various energetic formulations. In applications for explosives designed to defeat stockpiles of chemical and biological weapons, it is desirable that in addition to the generated temperature and pressure pulses, biocidal combustion products are released. It is further desired to combine the capability to produce biocidal compounds with an optimized combustion behavior. Halogens are well known to form a variety of biocidal species. However, from the point of view of energetic ingredients, halogens form either stable ionic compounds limiting the energy available for combustion, or compounds that are relatively unstable, hard to handle, and subject to rapid aging. Therefore, directly adding halogens to energetic formulations appears to be impractical. Instead, metal-based composites containing elemental (or loosely bound) halogens stabilized at room temperature are of interest. Such fuels are expected to increase the volumetric

reaction enthalpy of energetic formulations, as do conventional metal fuel additives; they also will help producing biocidal combustion products upon ignition. This project presents an effort to develop such a fuel additive based on aluminum, the most widely used metal additive to all types of energetic formulations. In this work, it is proposed that stabilized Al-halogen composites can be prepared by mechanical alloying, so that biocidal halogenated combustion products are released upon combustion. Iodine, which is solid at room temperature and is more readily available and simpler to handle than other halogens, was selected for this effort.

The objective of this work is to prepare powder-like Al-$I_2$ composites which can be easily handled at normal conditions. Such materials are expected to burn similar to unmodified aluminum and produce iodine-containing biocidal combustion products. The capability of such powders to capture and retain iodine until they are heated to high temperatures is of critical importance. In order to produce a material for which combustion and biocidal characteristics can be readily determined in laboratory experiments, it is desired to produce equiaxial particles in the size range of 10-100 μm. Particles that are much coarser, much finer, or flake-shaped could be of interest to practical applications, but are difficult to characterize using established laboratory ignition and combustion measurement techniques developed for micron-sized metal powders.

## 2.2 Experimental

### 2.2.1 Materials and Ball Milling Parameters

The Al-$I_2$ composites were prepared by ball-milling [36] elemental aluminum and iodine under various conditions. The initial mixture loaded into the ball mill was a blend of aluminum powder and iodine chips. Aluminum powder, -325 mesh size (< 45 μm), 99.5% pure was provided by Atlantic Equipment Engineers. Iodine chips, 99% pure, were provided by Sigma Aldrich. In one experiment, the starting mixture comprised aluminum powder mixed with a powder of aluminum iodide, $AlI_3$, 99.99+% (metals basis), obtained from Alfa Aesar.

Most of the samples were prepared using a model 01HD attritor mill by Union Process. The mill includes a stationary milling vial inside a cooling jacket. The steel milling vial is 750 mL in volume. The balls are agitated by a rotating impeller. Two types of milling vial lids provided by Union Process were used: one designed for experiments in controlled gas environments, and the other, designed for milling in liquid nitrogen. In all experiments, the impeller rotation rate was set to 400 rpm. The main process variables were the milling environment inside the milling vial and the cooling agent circulating through the cooling jacket surrounding the milling vial.

Powders were loaded at room temperature in air; milling balls were added after the starting materials. Nitrogen was flushed through the charge to prevent oxidation during the milling process.

Room temperature milling runs used running water in the cooling jacket and nitrogen gas fed through the milling vial at a flow rate of about 2 CFM (0.94 L/s). In initial experiments, the flow rate was not closely monitored, but it was noticed that a higher nitrogen flow rate results in a lower average amount of iodine retained in the mechanically alloyed powders.

Cryogenic milling runs used two configurations, in both cases the cooling jacket was filled with liquid nitrogen. In one setup, gaseous nitrogen was continuously fed through the milling vial, and in the other, the milling vial was also filled with liquid nitrogen.

Hardened steel balls were used as milling media. The total mass of milling balls was fixed at 1.8 kg. Different aluminum-to-iodine mass ratios were used to prepare materials with different compositions. Milling time, milling ball sizes and ball-to-powder mass ratios (BPR) were also varied.

The bulk of the material was recovered after completion of a milling run. In addition, small samples of materials were recovered from the vial at intermediate milling times to observe the particle evolution. No process control agent was added to the material being milled. In one experiment, the product powder obtained by ball-milling under specified conditions was used as a starting material for the second ball-milling run.

Table 2.1 shows a summary of the milling conditions representing samples prepared in the attritor mill.

A shaker mill (SPEX Certiprep, 8000 series) with two 50 mL flat-end steel vials was also used to prepare Al-$I_2$ composites. In addition to using elemental Al and I as starting materials, in one shaker mill experiment, elemental Al was mixed with $AlI_3$ to obtain an equivalent Al/I=90/10 composition. In the shaker mill the milling vial is cooled by a flow of room temperature air. Milling time for all shaker mill runs was set to 10 hours. Powders were loaded in argon gas. Material compositions, ball sizes, and ball-to-powder mass ratios were varied, as shown in Table 2.2.

**Table 2.1** Samples Prepared in Attritor Mill

| Sample ID | Ball Size, inch | Mass load ratio (Al/I) | BPR | Milling time, h | Cooling agent | Milling environment |
|---|---|---|---|---|---|---|
| 1-1 | 3/8 | 95/5 | 36 | 6 | Liquid $N_2$ | Gas $N_2$ |
| 1-2 | 3/8 | 90/10 | 36 | 6 | Liquid $N_2$ | Gas $N_2$ |
| 1-3 | 3/8 | 80/20 | 36 | 6 | Liquid $N_2$ | Gas $N_2$ |
| 1-4 | 3/8 | 90/10 | 36 | 10 | Liquid $N_2$ | Gas $N_2$ |
| 2-1 | 3/8 | 95/5 | 36 | 6 | Water | Gas $N_2$ |
| 2-2 | 3/8 | 90/10 | 36 | 6 | Water | Gas $N_2$ |
| 2-3 | 3/8 | 80/20 | 36 | 6 | Water | Gas $N_2$ |
| 2-4 | 3/8 | 90/10 | 36 | 24 | Water | Gas $N_2$ |
| 3-1 | 3/16 | 95/5 | 18 | 6 | Liquid $N_2$ | Gas $N_2$ |
| 3-2 | 3/16 | 90/10 | 36 | 6 | Water | Gas $N_2$ |
| 4-1 | 3/8 | 95/5 | 36 | 6 | Liquid $N_2$ | Liquid $N_2$ |
| 4-2 | 3/16 | 90/10 | 36 | 6 | Liquid $N_2$ | Liquid $N_2$ |
| 5-1* | 3/16 | 90/10 | 36 | 3.5 | Liquid $N_2$ | Liquid $N_2$ |
| 5-2* | 3/8 | 90/10 | 36 | 3.5 | Liquid $N_2$ | Liquid $N_2$ |

*Note: Sample 5-1 used sample 3-2 as a starting material; sample 5-2 used sample 1-2 as a starting material;

**Table 2.2** Samples Prepared in Shaker Mill

| Sample ID | Starting materials | Ball size, inch | Mass load ratio (Al/I) | BPR |
|---|---|---|---|---|
| s-1 | Al, $AlI_3$ | 3/8 | 90/10 | 10 |
| s-2 | Al, I | 3/8 | 90/10 | 10 |
| s-3 | Al, I | 3/8 | 95/5 | 10 |
| s-4 | Al, I | 3/16 | 95/5 | 5 |

### 2.2.2 Characterization of Al-$I_2$ Composites

The powders were characterized using scanning electron microscopy (SEM). For SEM analyses, a Phenom Tabletop Microscope by FEI Technologies Inc. was employed. Back-scattered electrons were used to obtain images showing the phase contrast between the materials.

Particle size distributions (PSD) for the prepared Al-$I_2$ powders were measured using a Beckman-Coulter LS230 Particle Counter. Ethylene glycol was used as suspension solvent for small quantities of powders.

X-ray diffraction (XRD) was used to determine phase composition for each sample. The XRD was performed on a Philips X'pert MRD powder diffractometer operated at 45 kV and 40 mA using unfiltered Cu K radiation (=1.5438 Å). Scan angle was in the range of 10-70 degrees. Two sample holders were used for XRD measurements. The standard sample holder has 20 mm length, 15 mm width and 2 mm depth. It was used for samples available in relatively large quantities. When only small amounts of powders were available, as was the case for samples recovered from

intermediate milling times, or for samples pre-heated to and cooled from a specific temperature, a smaller quartz sample holder was used with the diameter of the sample area of about 8 mm.

Selected XRD traces were processed for the purpose of quantitative phase analysis by whole-pattern refinement using the GSAS software package. The choice of sample holder influenced these results. The smaller quartz sample holder uses very small amounts of material, and therefore systematically underrepresents the diffracted intensities at lower diffraction angles. In most product samples $AlI_3$ was present, although only its main peaks at relatively low diffraction angles could be clearly distinguished. This caused the estimated concentration of $AlI_3$ to be systematically lower when the quartz sample holder was used compared to when the larger standard sample holder was used.

The amount of iodine captured in the materials and its release upon heating were more directly determined from thermogravimetric (TGA) traces in argon. A TA Instruments model Q5000IR thermogravimetric analyzer was used in this project. For initial characterization samples with weight varied from 5 to 35 mg were loaded into an alumina crucible, which was put in the platinum pan, according to the recommendations of TA Instruments. In further experiments, materials were placed in alumina pans enabling preparation of the samples with greater surface areas for more accurate TGA

measurements. The balance and the furnace were purged with argon at 10 and 25 ml/min, respectively. The maximum temperature was limited to 1273 K (1000 ºC).

Iodine release upon heating was determined in argon with varying heating rate from 5 to 200 K/min. As oxygen is hard to purge away, higher flow rate for argon was used in experiments aimed to quantify the kinetics of iodine release. Argon flow rates for balance and the furnace were set at 20 and 50 ml/min, respectively. The mass of material used for iodine release kinetics measurements varied in the range of 1-20 mg.

Oxidation kinetics of samples was studied in oxygen-argon mixtures and pure oxygen with varying heating rate from 5 to 200 K/min. The balance and the furnace were purged with oxygen-argon mixtures or pure oxygen at 10 and 25 ml/min, respectively. The mass of material used for oxidation kinetics measurements varied in the range of 0.4-5 mg.

## 2.3 Materials Preparation

### 2.3.1 Results

**2.3.1.1 Particle Shapes and Dimensions.** Characteristic SEM images of the materials prepared under different conditions are shown in Figure 2.1. For 6-hour long milling runs, flake-like particles were formed under all milling conditions, except for the case when liquid nitrogen was used both inside the milling vial and in the cooling jacket. In the latter case, the particles were roughly equiaxial. In addition, particles with

equiaxial shapes were obtained in run 2-4, when milling time was increased to 24 hours. As illustrated in Figure 2.1, cryomilling generally produced smaller particles than milling at room temperature. Images shown in Figure 2.1 used backscattered electrons, and iodine-rich areas appear brighter. In Figure 2.1A, at low magnification the scale of mixing between aluminum and iodine appears quite coarse. For samples appearing homogeneous, the scale of mixing is below the resolution of the images.

Particle sizes are observed to decrease with increasing iodine concentration. In general, particle sizes and shapes for powders prepared in the shaker mill were similar to those of powders prepared in the attritor mill at room temperature.

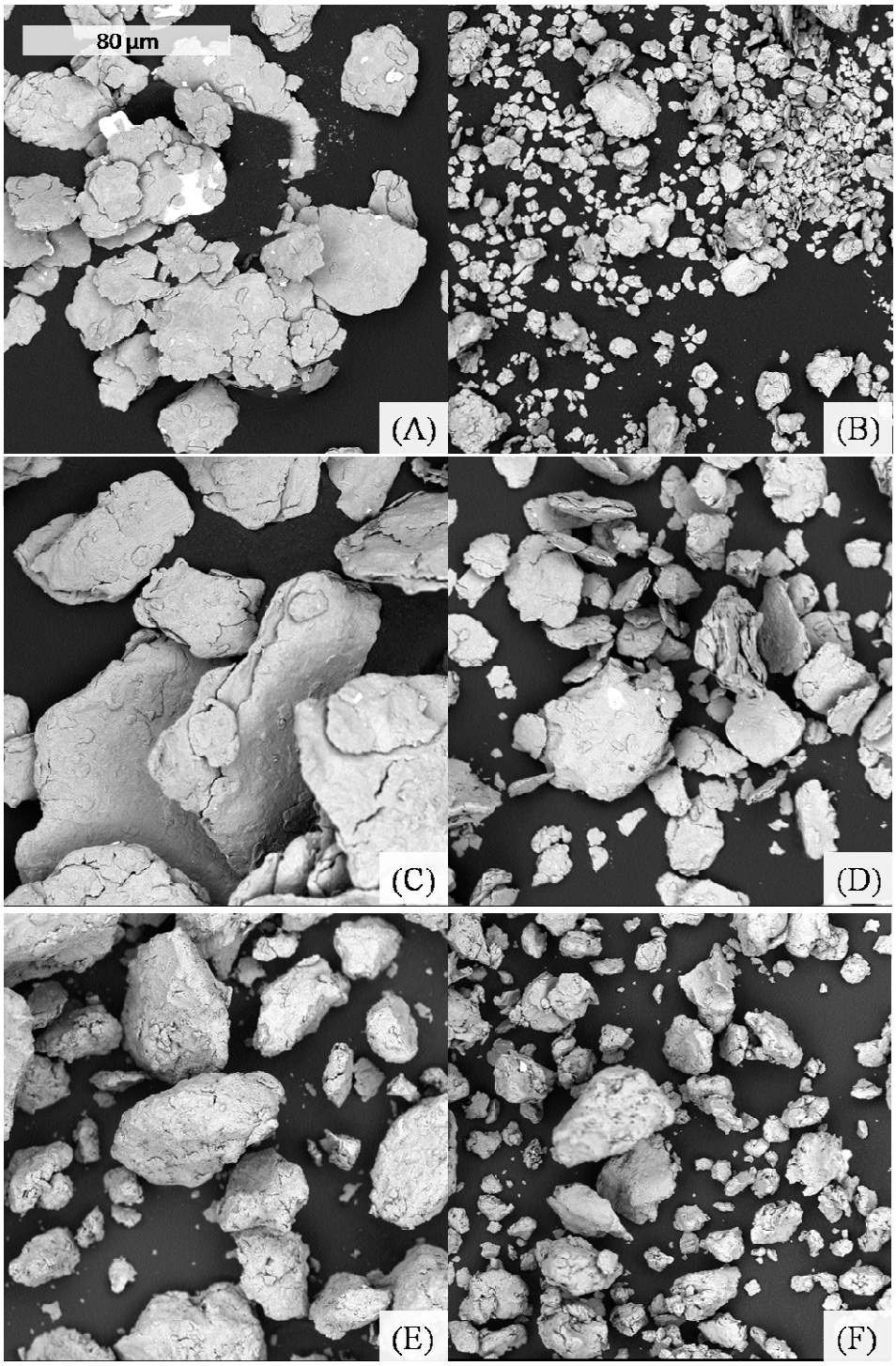


**Figure 2.1** SEM images of samples; magnification is the same for all images. Samples have nominal iodine concentrations of 5% on the left and 10 % on the right. Samples in the first row were cryomilled in $N_2$ gas, samples in the middle row were milled at room temperature in $N_2$ gas, and samples in the bottom row were cryomilled in liquid nitrogen. (A: 1-1, B: 1-2, C: 2-1, D: 2-2, E: 4-1, F: 4-2.)

**2.3.1.2 Iodine Content and its Release upon Heating.** For direct reference, mass reduction upon heating for both pure iodine and $AlI_3$ were characterized by TGA; the results are shown in Figure 2.2 where a TGA trace for one of the mechanically alloyed samples is also shown. The pure iodine sample evaporates completely before it reaches 473 K (200 °C). $AlI_3$ starts decomposing from room temperature, the decomposition rate increases at around 473 K (200 °C) when $AlI_3$ melts, and most of the decomposition ends before the sample reaches 673 K (400 °C). The TGA trace for the material mechanically alloyed in the shaker mill, sample s-3, shows a very small mass loss up until the temperature reaches about 733 K (440 °C). The mass loss occurring at higher temperatures accelerates near the aluminum melting point. As discussed below, this behavior was generally observed for all mechanically alloyed samples, except for those milled in liquid nitrogen.

Sets of TGA traces for the materials series 1 and 2 (see Table 2.1) are shown in Figure 2.3. As expected, the overall mass loss at 1273 K (1000 ºC) is greater for greater nominal iodine contents of the composite. This is true for both, samples milled at room temperature and at cryogenic temperature. Further, iodine release occurs in several steps, which are more or less clearly distinguished, depending on the sample.

For all samples the mass loss rate increases around 373 K (100 ºC), and decreases again by about 623 K (350 ºC). Figure 2.3 shows the mass loss for samples milled in $N_2$ gas. For samples milled in liquid $N_2$ the overall mass loss was substantially smaller.

At temperatures between 373 and 623 K, samples milled in liquid $N_2$ (samples 4-1 and 4-2 in Table 2.1) behaved similarly to the other materials. However, almost no mass loss was detected for those materials at higher temperatures. Therefore, the following discussion is focused on the materials milled in $N_2$ gas.

For both, cryomilled and room-temperature milled samples, for compositions with less than 10% of iodine, only minor mass loss is observed at temperatures between 373 and 623 K. It is noticeable, however, that for this temperature range samples milled at room temperature (series 2) lose more mass than respective samples with nominally identical compositions milled at cryogenic temperature (series 1). Starting at about 673 K (400 ºC), the second broad mass loss step continues up to the melting point of Al. A sharp mass loss step is associated with Al melting. It is followed by additional slight and gradual mass loss.

The pattern observed for the samples nominally containing 20 % iodine is qualitatively different and primarily consists of two mass loss steps spread over broad temperature ranges. The first step begins at about 373 K (100 ºC), as for all other samples, but is much stronger than for samples with lower nominal iodine content. It is followed by a second gradual mass loss step beginning at about 673 K (400 ºC). For the cryomilled sample, the first step ends at about 623 K (350 ºC), while for the sample milled at room temperature, the first step effectively overlaps with the second one. This second step continues until the sample reaches the aluminum melting point, and it is

apparent that nearly all iodine captured in the material is released by that time. Thus, only minor iodine release occurs upon Al melting, while a slow mass loss continues as the sample is heated to higher temperatures.

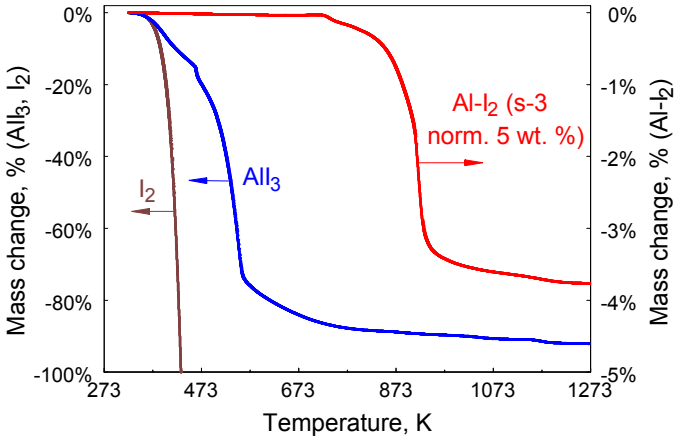


**Figure 2.2** TGA decomposition traces of pure $AlI_3$, $I_2$ and sample s-3.

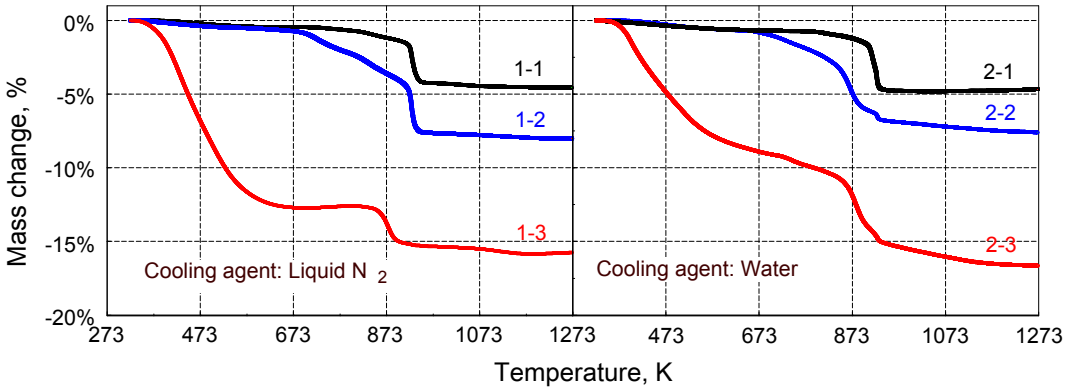


**Figure 2.3** TGA traces of samples 1-1, 1-2, 1-3 and 2-1, 2-2 and 2-3.

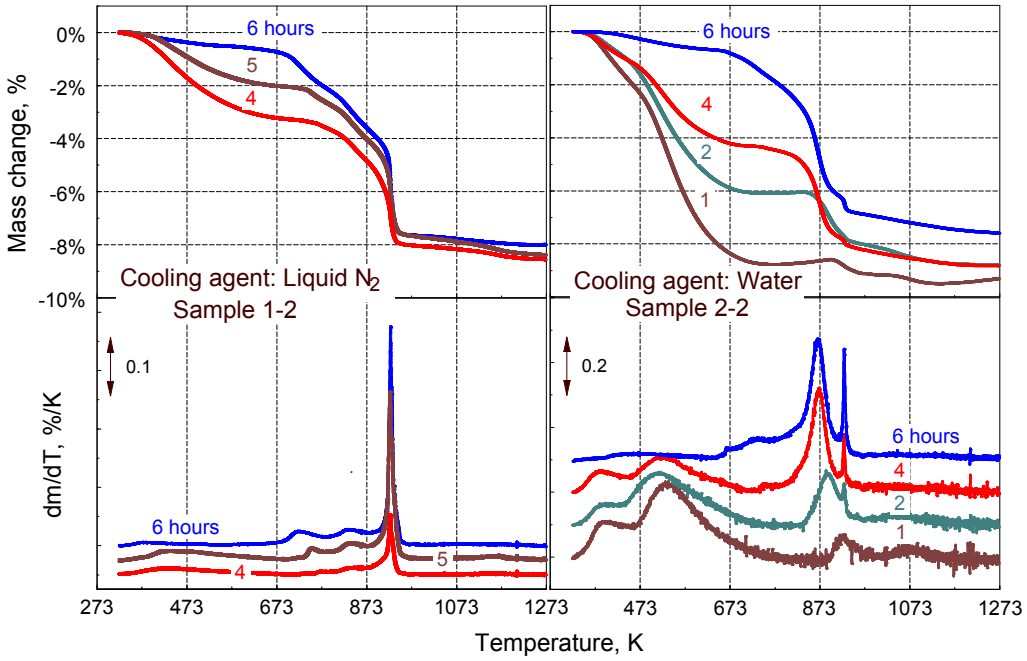


**Figure 2.4** TGA traces and mass loss rates for samples recovered at different milling times.

TGA traces for samples recovered at different milling times are shown in Figure 2.4. For both, cryomilled and materials milled at room temperature the amount of iodine released at high temperatures increases with longer milling times. It is also noted that the total amount of iodine released upon heating to 1273 K (1000 ºC) slowly decreases for longer milling times, indicating iodine loss during milling. This effect is stronger for material milled at room temperature.

Each of the two broad mass reduction steps between 373 and 623 K and between 673 K and the aluminum melting point consists of sub-steps, as is evident from the *dm/dT* signals. These sub-steps are better distinguished for the low-temperature (373-623 K) mass loss for samples milled at room temperature, for which the mass loss at lower

temperatures is greater. Conversely, for the cryomilled sample a more significant mass loss occurs between 673 K (400 ºC) and the aluminum melting point, and the respective mass loss sub-steps are distinguished better.

For all individual *dm/dT* peaks, except for the sharp peak associated with the aluminum melting, the peak positions shift to lower temperatures as the milling time increases. For the sample milled for 24 hours (not shown for brevity), the overall shape of the TGA curve does not differ substantially from that shown in Figure 2.4 for the sample milled for 6 hours. However, the strongest peak in the *dm/dT* trace shifts to higher temperatures, nearly coinciding with the sharp peak associated with aluminum melting.

TGA measurements were also performed for the samples prepared in the shaker mill. As illustrated in Figure 2.2 (see also Figure 2.5), these samples decomposed in a sequence of steps similar to that described above for the samples milled in the attritor mill with water used as a cooling agent.

The effect of the starting material is illustrated in Figure 2.5. The shapes of the TGA trace for material prepared from Al and $I_2$ is substantially the same as the trace for material prepared from Al and $AlI_3$ with the same nominal bulk composition. This suggests that regardless of the starting material, the distribution of the bulk of the iodine within the Al matrix is only affected by the milling process. The most noticeable difference is a small but relatively sharp mass loss step around 553 K (280 ºC) for the

sample prepared with $AlI_3$ as a starting material. This step-wise mass loss correlates well with the major mass loss step observed for pure $AlI_3$ as shown in Figure 2.2. This step was never observed for mechanically alloyed samples prepared using elemental iodine. The onset of the main mass loss sequence in samples prepared from elemental iodine occurs at slightly higher temperatures. This may indicate the possibility that some $AlI_3$ remains unaltered under the milling conditions used here if $AlI_3$ is used as starting material.

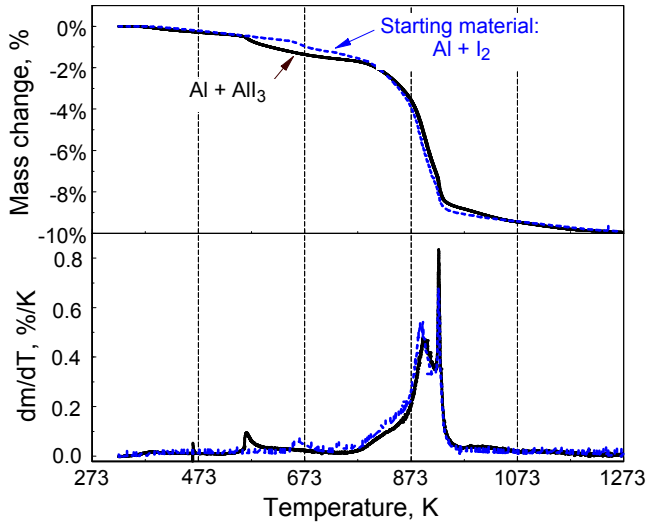


**Figure 2.5** TGA traces and respective derivatives for samples s-1 (solid line) and s-2 (dashed line).

**2.3.1.3 Material Structure and Composition.** Characteristic XRD patterns collected for different samples with varying milling conditions are shown in Figure 2.6. The peak pattern for Al and the strongest peak for $AlI_3$ (between 25 and 26º) were recognized for all samples. In some samples, additional $AlI_3$ peaks were identified. The

peaks of $AlI_3$ are broad for most samples indicating that $AlI_3$ is not well crystallized. The strongest presence of $AlI_3$ occurs in the cryomilled sample 1-2. The XRD traces of series 1 and 2 show that cryomilled samples have sharper $AlI_3$ peaks, and thus a more ordered structure than the room temperature milled powders with the same nominal composition.

Several peaks observed in the XRD patterns could not be identified. In particular, a peak around 27°, most clearly observed for the samples 1-2 and 2-3 in Figure 2.6, was found in every pattern. It may not be clearly seen in some of the traces presented in Figure 2.6; however, with whole pattern refinement (using GSAS) assuming the presence of Al and $AlI_3$, this peak was identified for all the patterns. Additional unrecognized peaks were observed in samples 1-2, 2-2 (at 11º) and 2-3 (at 23°).

Finally, XRD was used to examine samples heated to specific temperatures in the TGA furnace. The patterns from sample 1-2 heated to and cooled from 673, 783, and 873 K, are shown in Figure 2.7. The pattern for the as-prepared material, shown already in Figure 2.6, is repeated in Figure 2.7 for reference. The quartz sample holder was used to characterize the small batches of materials recovered after heating to intermediate temperatures. Upon heating, $AlI_3$ peaks become sharper but hardly decrease in intensity. The $AlI_3$ peaks remain clearly identifiable even for samples heated above the reported decomposition temperature of $AlI_3$ (~673 K).

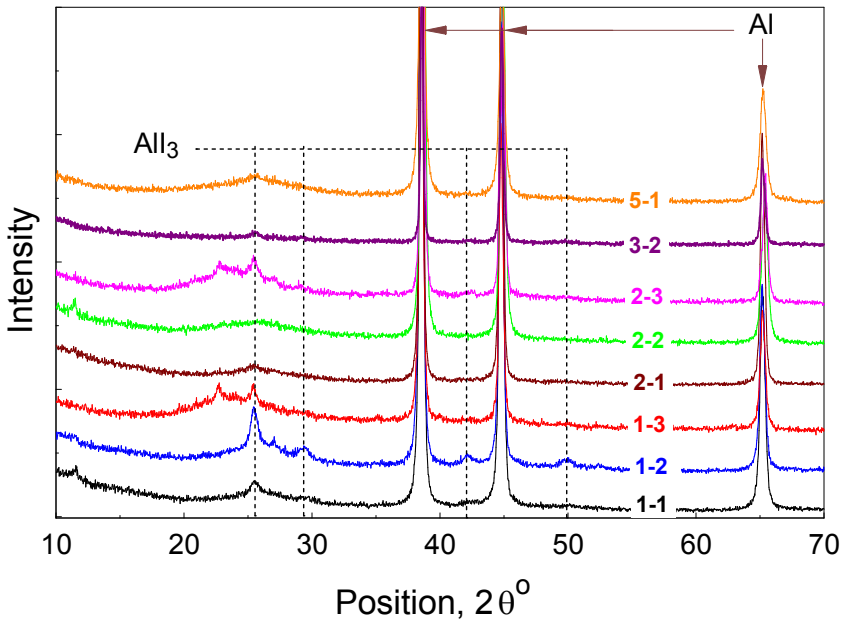


**Figure 2.6** XRD patterns for mechanically alloyed Al-$I_2$ materials. A smaller quartz sample holder was used to characterize sample 3-2; other samples were placed into the standard sample holder.

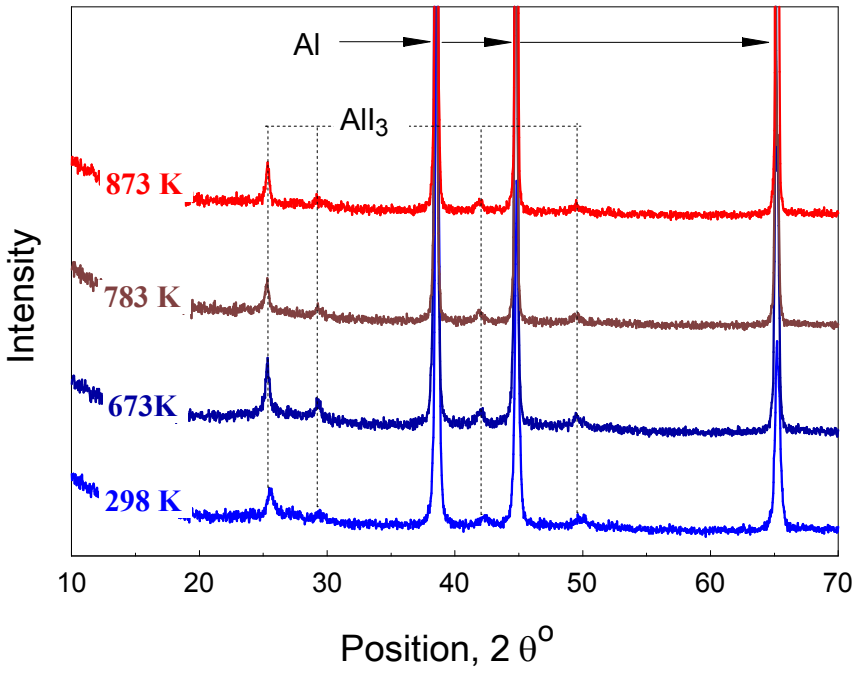


**Figure 2.7** XRD patterns of sample 1-2 heated to and cooled from different temperatures.

XRD results were analyzed by whole pattern refinement using the GSAS software package. The measured patterns were fitted with calculated patterns assuming the composition to include only two components, Al and $AlI_3$.

Table 2.3 shows that substantial part of iodine incorporated into the mechanically alloyed materials, more than half for most samples, is not contained in the $AlI_3$ detectable by XRD. The relative amount of iodine unaccounted for by $AlI_3$ is smallest for the samples loaded with 10% of iodine.

Quantitative X-ray analysis was also used to observe whether the iodine distribution within the sample changes upon heating. Respective results for sample 1-2 are shown in Table 2.4. For these measurements, the small sample holder was used consistently, and consequently the $AlI_3$ concentration shown for "as-prepared" material in Table 2.4 is lower than for the same material (1-2) shown in Table 2.3, for which the XRD data from the standard sample holder were used. Nevertheless, the results shown in Table 2.4 can be compared between themselves. The rate at which the overall weight loss is measured by TGA exceeds slightly the relative rate of reduction in the $AlI_3$ concentration; respectively, the percentage of iodine that remains unaccounted for decreases slightly as the temperature to which the sample is heated increases. This is a somewhat unexpected result, considering that $AlI_3$ is reported to boil off at 655 K (382 ºC) [53] and is observed to decompose nearly completely by 673 K (400 ºC) in the TGA measurements shown in Figure 2.2

**Table 2.3** Iodine Concentrations in the Prepared Materials Estimated from TGA ($I_{TG}$) and from Quantitative X-ray Analysis ($I_{AlI3}$).

| Sample ID | Wt. fraction of I loaded, $I_0$, % | Total TGA mass loss, $I_{TG}$, % | XRD whole pattern processing: wt. fraction of I in $AlI_3$, $I_{AlI3}$,% | Iodine balance (unaccounted for), $(I_{TG}-I_{AlI3},)/I_{TG}\cdot 100$ % |
|---|---|---|---|---|
| 1-1 | 5 | 4.56 | 1.59 | 65.1 |
| 1-2 | 10 | 8.01 | 4.02 | 49.8 |
| 1-3 | 20 | 15.53 | 3.18 | 79.5 |
| 2-1 | 5 | 4.62 | 1.60 | 65.4 |
| 2-2 | 10 | 7.53 | 3.24 | 57.0 |
| 2-3 | 20 | 16.49 | 4.52 | 72.6 |
| 5-1 | 10 | 8.37 | 3.75 | 55.2 |

**Table 2.4** Iodine Weight Fractions Estimated from TGA ($I_{TG}$) and from Quantitative X-ray Analysis ($I_{AlI3}$) for Sample 1-2 Quenched from Elevated Temperatures.

| Temperature sample heated to, K | $I_{TG}$, wt. % | $I_{AlI3}$, wt. % | $(I_{TG}-I_{AlI3},)/I_{TG}\cdot 100$ % |
|---|---|---|---|
| As prepared | 8.01 | 2.06 | 74.3 |
| 673 | 7.05 | 1.69 | 76.0 |
| 783 | 5.41 | 1.44 | 73.4 |
| 873 | 4.19 | 1.34 | 68.0 |

**2.3.1.4 Preparation of Equiaxial Powders with Substantial Iodine Content.**

Examination of the samples prepared at different conditions showed that the most efficient particle size reduction and production of equiaxial particles occurs when milling is performed with liquid nitrogen as a milling medium. However, based on the very low measured weight loss in the TGA experiments it was also observed that iodine is almost not retained in such powders. Therefore, additional experiments were performed in

which material was initially prepared by room temperature milling and only then size-reduced by milling in liquid nitrogen. Specifically, material 3-2 (see Table 2.1) was milled for 3.5 additional hours with liquid nitrogen in both the vial and cooling jacket (ID 5-1 in Table 2.1). Samples were recovered every 30 min from the mill, and substantial reduction of particle sizes and formation of equiaxial particles were observed after 3.5 hours, at which point the milling was stopped.

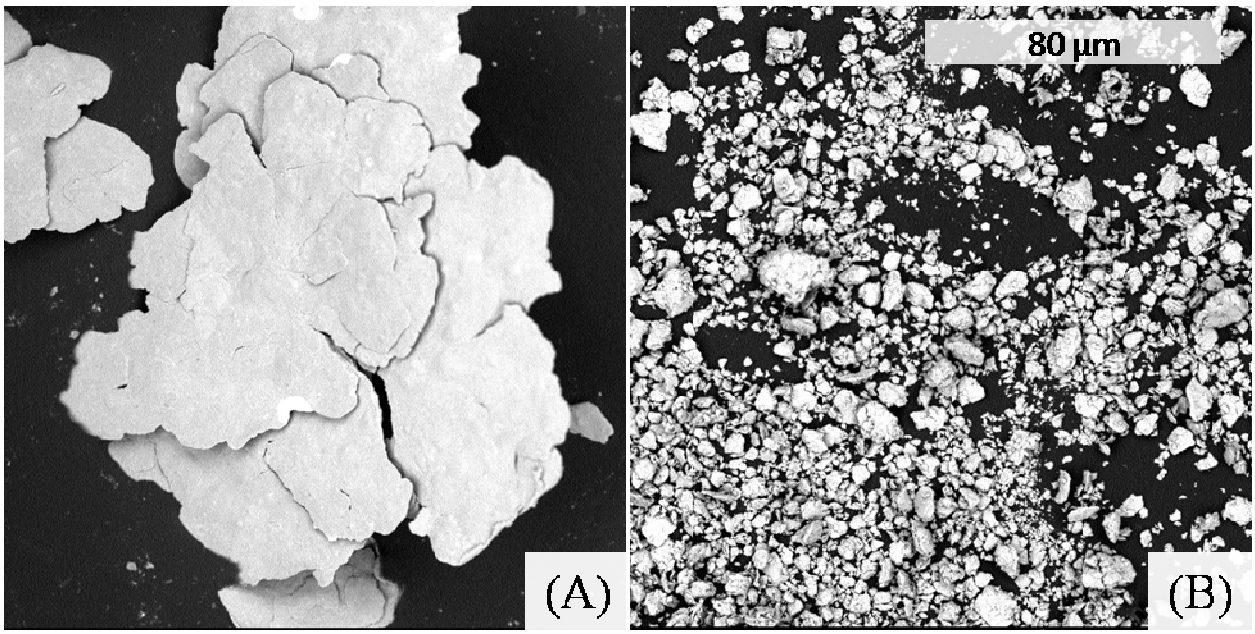


**Figure 2.8** SEM images comparison of sample 3-2 and sample 5-1; magnification is the same for both images. A: sample 3-2, B: sample 5-1.

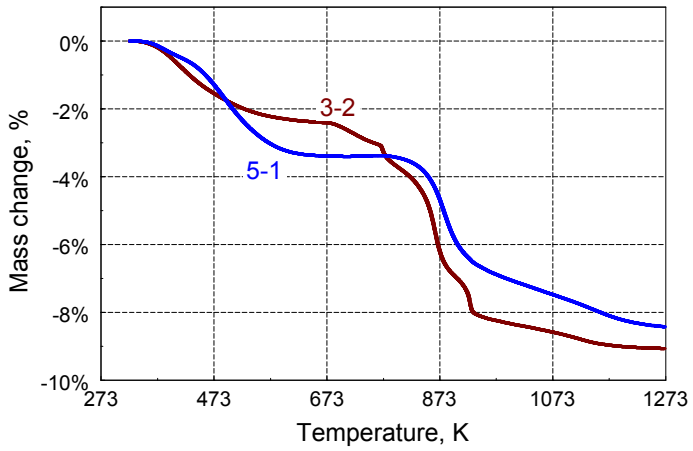


**Figure 2.9** TGA traces of samples 3-2 and 5-1.

The SEM images of samples 3-2 and 5-1 are shown in Figure 2.8. Both, marked reduction in particle dimensions and change in the particle shapes are clearly observed.

The TGA traces for the prepared uniaxial powder (sample 5-1) and its parent material (sample 3-2) are shown in Figure 2.9. The traces are qualitatively similar; however, the overall iodine concentration retained in the material after milling in liquid nitrogen is reduced compared to the parent material. It is also noted that compared to the parent material, iodine release occurs at somewhat lower temperatures for the material milled in liquid nitrogen.

### 2.3.2 Discussion

**2.3.2.1 Synthesis of Mechanically Alloyed Powders.** Both room temperature and cryogenic mechanical milling are suited to encapsulate iodine in aluminum. In both cases, iodine behaves as an effective milling process control agent resulting in flake-like

particle shapes preserved for a relatively long time. Also, similar to the effect of conventional milling process control agents, an increase in the load of iodine results in a decrease in the product particle dimensions. The product particle sizes are also reduced by milling at liquid nitrogen temperature, presumably due to reduction in the ductility of aluminum. Equiaxial particles are readily obtained by milling in liquid nitrogen as a milling medium; however, milling in liquid nitrogen results in a relatively rapid loss of iodine from the system. For milling in nitrogen gas, the loss of iodine is faster at higher nitrogen flow rate through the milling container. It is likely that the loss of iodine is directly correlated with the gas flow, which is substantially increased when the container is filled with boiling liquid nitrogen. When iodine loss is accelerated by a greater purging gas flow, its effect as a process control agent is also reduced, resulting in a more rapid formation of the mechanically alloyed composites between aluminum and the remaining iodine.

The difference in iodine release upon heating for the samples milled at different temperatures is relatively minor. At the same time, an improvement in stabilizing iodine in Al by cryogenic temperature milling compared to the room temperature milling is measurable. For both, room temperature and cryogenic milling, the amount of iodine released at higher temperatures increases with longer milling times. Comparison of samples milled for different times indicates that the 6-hr milling results in a stabilized material when the initial iodine concentration is 5 wt. %. The material is also nearing its

stabilized composition for the compositions with 10 wt. % of iodine. For the compositions deemed stabilized, only about 10 % of the iodine retained in the material is released upon heating to 673 K (400 ºC). Using longer milling times does not result in a substantial reduction of this relatively low-temperature iodine loss. Based on this assessment, the materials prepared at the liquid nitrogen temperature are closer to their stabilized state than similar materials prepared at room temperature. Further, materials with 20 wt. % of initial iodine are far from their stabilized condition. Comparing their respective TGA traces, it appears that a longer milling time would result in a further increase of iodine fraction retained in such materials; however, the very long milling times may be impractical especially considering the small but steady iodine loss due to the purging of the milling container. It is possible that the milling efficiency can be further improved by adjusting the ball sizes and speed of impeller (rpm), so that the times required to achieve a stabilized state are somewhat reduced. However, such optimization of the milling parameters was outside the scope of the present effort.

It is likely that the limit to the iodine concentration that can be retained in aluminum at elevated temperatures depends more on the specific milling conditions and less on the characteristics of aluminum and iodine themselves. More than 7 wt. % of iodine was observed to be released above 673 K (400 ºC) in this effort for a material prepared using elemental Al and I as starting materials in the attritor mill (cf. Figures 2.3, 2.4); however, this concentration is not the limit for the material system. For the

material prepared in the shaker mill, a greater overall percentage of iodine was captured in the material and more than 9 % of iodine was retained upon the material's heating to 673 K (400 ºC), as shown in Figure 2.5.

**2.3.2.2 Aluminum-Iodine Compounds.** Only a small portion of iodine contained in the mechanically alloyed material is similar to "free iodine" and thus released upon heating to 473 K (cf. Figure 2.2). Most of the retained iodine is either bonded to aluminum or at least effectively encapsulated, so that it remains in the material at elevated temperatures. It is also observed that $AlI_3$, the only reported stable aluminum iodide, may not be the only or even the primary compound formed. The formed $AlI_3$ is poorly crystalline and is likely embedded in an Al matrix. The latter assessments are based on both TGA and XRD results. Based on TGA measurements, pure $AlI_3$ decomposes nearly completely upon its heating to about 673 K (400 ºC); however, less than 10 % of the entire iodine retained in stabilized mechanically alloyed powders is released upon heating to this same temperature (compare Figure 2.2 vs. Figures 2.4, 2.5). XRD also show that $AlI_3$ remains detectable as a stabilized phase in the material upon its heating up to 873 K (600 ºC), as shown in Table 2.4, while substantial loss of iodine content is observed from the TGA measurements.

Release of iodine occurring in well-distinguishable steps preceding aluminum melting (see Figure 2.4) indicates formation of several Al-$I_2$ compounds. Identification of separate steps suggests that multiple distinct phases may be present in the material, or

that some phases undergo transformations as the material is being heated. Indeed, formation of AlI and, possibly, other intermediate compounds was inferred by early work studying solubility of Al in $AlI_3$[54]. Mechanical alloying is known to effectively generate metastable alloys, similar to rapidly quenched melts[34], so the formation of such compounds is not surprising. XRD was inefficient in resolving the structural differences between the formed compounds, indicating that they are either poorly crystalline or exist as very fine inclusions. However, the observation that decomposition steps shift to different temperatures (see Figure 2.4) for materials milled for different times is consistent with the concept of iodine redistribution among several phases induced by mechanical milling. In the future, high resolution transmission electron microscopy studies could be useful in resolving such inclusions and identifying their compositions and structures.

## 2.4 Conclusions

Mechanical alloying is effective in preparation of Al-$I_2$ compounds in which iodine is bonded to aluminum and is not released until the material is brought to high temperatures. Mechanical alloying at liquid nitrogen temperature is more effective in preparing stabilized Al-$I_2$ compounds than milling at room temperature. An increase in the flow rate through the milling vial results in a higher rate of iodine loss during milling. Milling directly in liquid nitrogen does not allow preparation of the stabilized Al-$I_2$

compounds; however, it results in the formation of relatively equiaxial particles as opposed to flake-like products obtained under other milling conditions. Therefore, milling directly in liquid nitrogen can be used as an additional milling step following the preparation of the stabilized material, when equiaxial and/or smaller particle sizes are desired.

Materials containing as much as 17 wt. % of iodine were prepared. However, for such high iodine concentrations, a substantial fraction of the retained iodine was released when the material was heated to less than 673 K (400 ºC). In fully stabilized mechanically alloyed samples, containing more than 8 wt. % of iodine, about 90 % of the entire iodine content was released after the material was heated above 673 K. In addition to poorly crystalline $AlI_3$, other iodine compounds were contained in the mechanically alloyed powders. In such compounds, iodine was bonded to aluminum stronger than in $AlI_3$, so that their thermal decomposition and respective iodine release occur at higher temperatures compared to decomposition and boiling of $AlI_3$.

# CHAPTER 3

# REACTION KINETICS OF Al-$I_2$ COMPOSITES

## 3.1 Introduction

Research is currently active on the development of multifunctional reactive materials. In particular, there has been interest in developing reactive compositions with biocidal combustion products[45, 47] . Such materials are needed for munitions aimed to defeat stockpiles of biological weapons. The potentially harmful spores and bacteria should be inactivated before they are released to the environment, and various methods of increasing the rate of such inactivation are being explored. Halogenated compounds are known to be effective biocides [48]; however, most such materials are unstable and difficult to handle. Therefore, it is of interest to generate such compounds in situ when biological agents are expected to be released. Aluminum powder is a common component of energetic formulations[3] and it is added to conventional explosives to achieve greater reaction temperatures and to maximize the energy density of the payload [24, 35-37, 50-52]. It was shown in Chapter 2 that mechanical milling can be used to prepare relatively stable aluminum-iodine (Al-$I_2$) composites. These materials have a high combustion enthalpy, comparable to that of pure Al, and they also release iodine upon heating. Initial experiments from Chapter 2 showed that Al-$I_2$ composites prepared by mechanical milling are more stable than conventional Al-$I_2$ compounds, i.e.,

$AlI_3$. It was also shown that the properties of the prepared composites are not affected strongly by selection of the starting materials (e.g., elemental I or $AlI_3$ mixed with Al) used for mechanical alloying. This Chapter is aimed to further explore the Al-$I_2$ composites prepared by mechanical milling; in particular, it is of interest to consider the kinetics of reactions leading to iodine release at different temperatures. Furthermore, ignition and oxidation behaviors of the prepared materials will be investigated and correlations between different reactions will be considered.

## 3.2 Materials

Two batches of materials with equiaxial shaped particles (sample 1-4 and 5-2, shown in Table 2.1) were used in these experiments. Sample 1-4 was size classified using a No. 170 mesh (88 μm opening size) sieve and powder passed through sieve was used. Sample A was continuously milled for 10 hours. The product powder was passed through a 170 mesh (88 μm opening size) sieve. Sample B was milled in two steps. The first step included milling for 6 hours as outlined above. The second step included 3.5 hour milling with liquid nitrogen fed into both cooling jacket and inside the milling vial. Using liquid nitrogen inside the milling vial helps to reduce the particle sizes of the prepared powders, but it also results in a less stable material for which greater iodine release occurs at low temperatures.

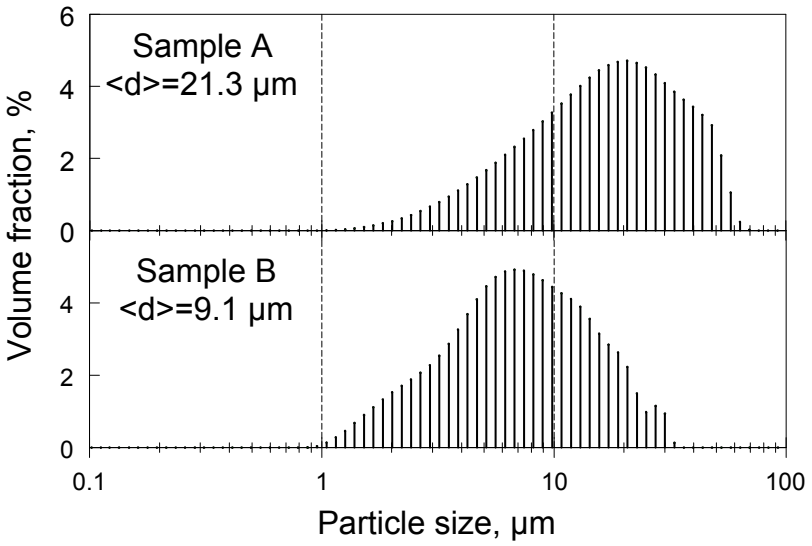


**Figure 3.1** Particle size distributions for samples A and B. Volume mean particle sizes are shown for each material.

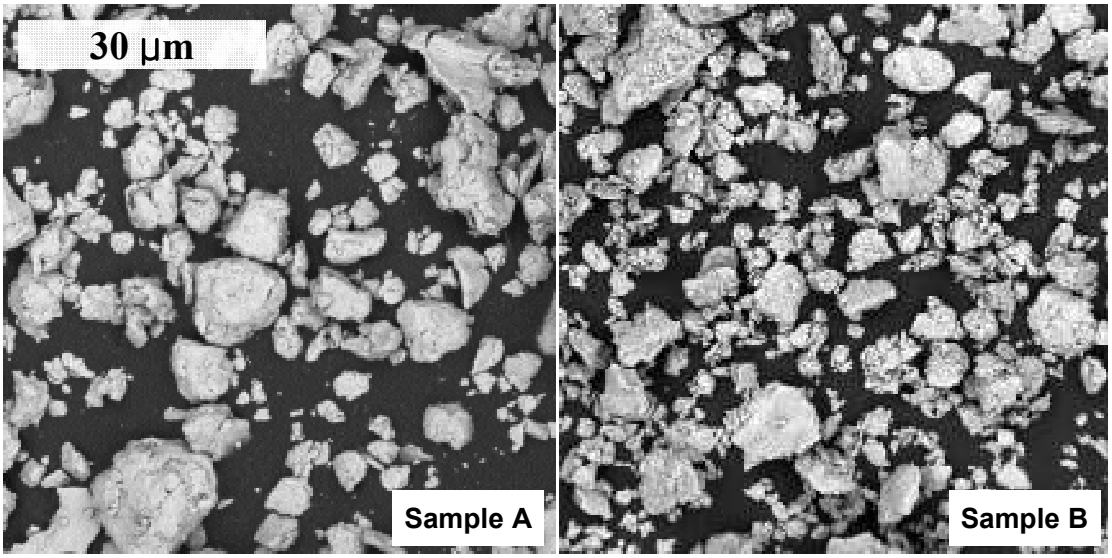


**Figure 3.2** SEM images of samples A and B; magnification is the same for both images.

In addition to the Al-$I_2$ composites, pure Al powder with nominal particle sizes in the range of 1 – 5 μm by Atlantic Equipment Engineers was used for selected oxidation experiments as a reference.

Figure 3.1 shows the particle size distribution (PSD) and respective volume mean particle sizes of samples A and B. The abrupt drop of the volume fraction of particles coarser than about 60 μm for sample A is due to sieving prior to use in this project. Both samples consist of micron-sized particles. The morphology of particles is illustrated in SEM images shown in Figure 3.2. Generally, both samples contain particles with equiaxial shapes, and particles of sample A are coarser and more rounded compared to sample B. As described above, using liquid nitrogen inside the milling vial helps to reduce the particle sizes of the prepared powders, but it also results in a less stable material for which greater iodine release occurs at low temperatures.

## 3.3 Experimental

A TA Instruments model Q5000IR thermogravimetric analyzer (TGA) was used for both iodine release and oxidation measurements. Materials were placed in alumina pans. For iodine release measurements, the balance and the furnace were purged with argon at 20 and 50 ml/min, respectively. These relatively high flow rates were selected to protect the balance from corrosive iodine, and to minimize the contamination of the furnace environment with traces of oxygen. The maximum temperature was limited to 1273 K (1000 ºC). The heating rates varied from 5 to 200 K/min. The mass of material used for iodine release kinetics measurements varied in the range of 1 – 20 mg.

Oxidation of Al-$I_2$ composites was studied in oxygen-argon mixtures and in pure oxygen. The balance and the furnace of Q5000IR were purged with argon at 10 ml/min and oxygen (purity 99.8 %) at 25 ml/min, respectively. Experiments were performed at heating rates varied from 5 to 200 K/min. The mass of material used in oxidation experiments varied in the range of 0.4 – 5 mg.

A heated filament ignition test was used to characterize ignition of the prepared materials at heating rates not achievable by the thermo-analytical measurements. Figure 3.3 shows a simplified diagram of the filament ignition apparatus. Details of this experimental technique are available elsewhere [31, 51, 55]. A 0.5 mm diameter 4.5 cm long Nickel-Chromium alloy wire was used as the electrically heated filament. The filament served as a load in a circuit including a set of DC batteries and an adjustable resistor connected in series. Thus, the heating rate of the filament was adjusted by changing the applied DC voltage and resistance. A small amount of powder was mixed with a surfactant and hexane, and this slurry was coated onto the filament to form a thin layer with a coated portion of about 1 cm in length. The coating dried prior to experiments. Ignition was observed using a silicon photodiode (DET110 by Thorlabs, Inc.) equipped with an iris aimed at the powder coating from a distance of 4 – 5 cm. A high speed camera (MotionPro 500 by Redlake) was also used to observe the ignition in some experiments. The temperature history of the heated filament was measured using a high-speed infrared pyrometer (DP1581 by Omega Engineering, Inc.), which was

focused on the uncoated surface of the filament adjacent to the powder coatings. The experiments were performed in air with varied filament heating rates. From this experiment, the ignition temperature was determined as a function of the heating rate.

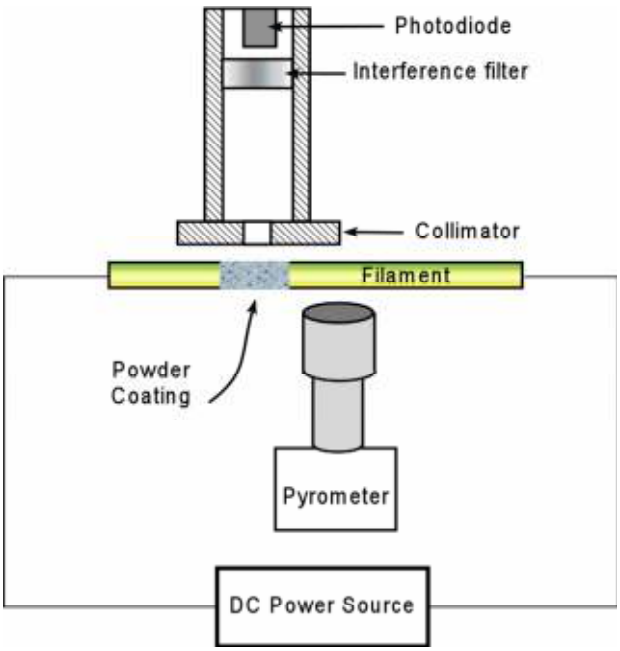


**Figure 3.3** Heated filament setup used for powder ignition experiments.

## 3.4 Results

### 3.4.1 Iodine Release

Mass reduction traces for samples A and B heated in argon at different heating rates are shown in Figure 3.4. Consistent with the second section, there are several main mass reduction stages. Initial iodine release occurs well before Al melting, starting at a temperature as low as about 373 K (100 ºC) and continuing to up to about 673 K (400

ºC). This iodine release stage is much stronger for sample B than for sample A. The second subsolidus iodine release stage begins in the vicinity of 873 K (600 ºC). It overlaps with aluminum melting. The second iodine release stage is substantially stronger for sample A, for which the amount of iodine released in the initial stage is very small. Iodine release continues after melting; however, the measurements at elevated temperatures are increasingly affected by oxidation with residual oxygen and thus do not provide a reliable measure of the iodine release rate. The iodine release from molten aluminum observed in these TGA experiments is also of little significance in terms of its effect on or interference with the material ignition (as shown below) and so it will not be analyzed.

To evaluate the kinetics of iodine release, consider Figure 3.5 showing temperature derivatives of the TGA traces presented in Figure 3.4. There are two clearly distinguished minima in the temperature range of 373 and 673 K, when the first broad iodine release stage occurs. This iodine release stage is weak for sample A; nevertheless the two minima in the *dm/dT* trace are clearly distinguished in the inset, showing fractions of the *dm/dT* traces at a magnified scale. Therefore, the first iodine release stage is further broken down into two steps. The temperatures at which the first and second steps occur correlate with the respective temperatures at which pure iodine and $AlI_3$ were observed to evaporate upon heating. The second iodine release stage is represented by a single minimum in the *dm/dT* trace. For sample B, this minimum and

the respective iodine release stage are nearly completed before the Al melting point. For sample A, the rate of iodine release appears to increase noticeably at the onset of aluminum melting, so that the shifts to higher temperatures at increased heating rates are smaller for the trailing edges of the respective minima of the *dm/dT* traces compared to those for the leading edges of the same minima.

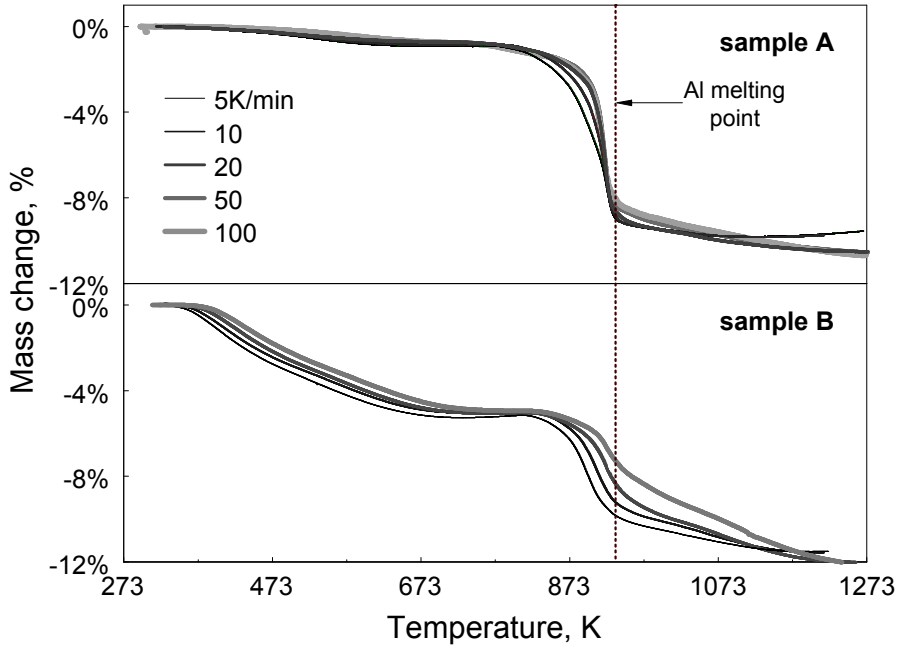


**Figure 3.4** Iodine release trace for sample A and B in TGA at different heating rates.

The TGA measurements were processed to calculate the iodine release activation energy as a function of the reaction progress, assumed to change between 0 and 1 for the as-prepared sample and the sample heated to 1273 K (1000 ºC), respectively. The data processing used a model-free integral isoconversion method proposed by S. Vyazovkin [56] accounting for the variation in the activation energy with the extent of conversion.

Results of the activation energy as a function of reaction progress are shown in Figure 3.6. For the first iodine release stage, the activation energy is generally low for both samples A and B. While less clearly distinguished, it appears that the first step has a somewhat lower activation energy (~ 50 kJ/mol) than the second one (~ 70 kJ/mol) for both samples. Specific values of the activation energies corresponding to the low temperature decomposition steps for samples A and B are very close to each other. The same activation energy values are also obtained using Kissinger analysis[57], following the minimum positions at various heating rates (not shown, for brevity).

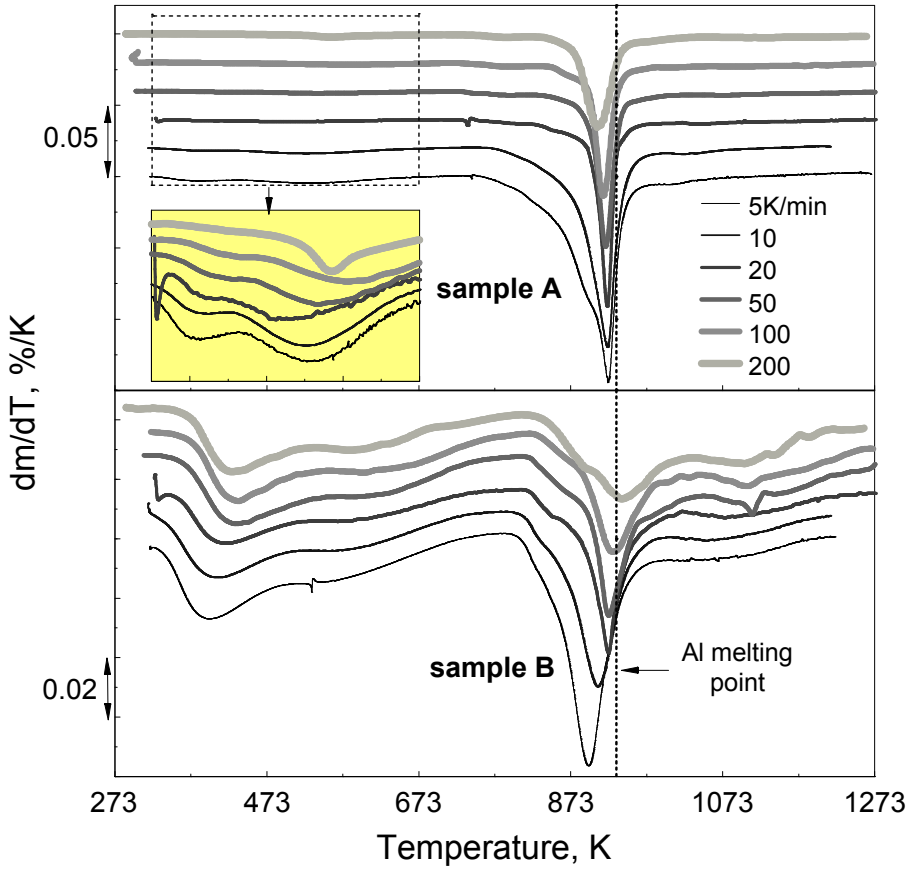


**Figure 3.5** Mass derivatives of iodine release for sample A and B in TGA at low temperature range for different heating rates.

For the second iodine release stage, (occurring at different reaction progress values for samples A and B), the activation energy increases for both materials. Note that the sharp spike in the activation energy immediately before it settles near 300 kJ/mol is an artifact due to residual oxidation occurring in the TGA experiments despite continuous flushing the furnace with pure argon. This oxidation is detected by slight increase in the sample weight after the completion of the first iodine release stage. Note also that the interference of melting with the second iodine release stage for sample A results in a rapid increase of the apparent activation energy, as shown in Figure 3.6. The melting point does not depend on the heating rate so that, once again, very high apparent oxidation energies observed for sample A at high reaction progress values are not physical.

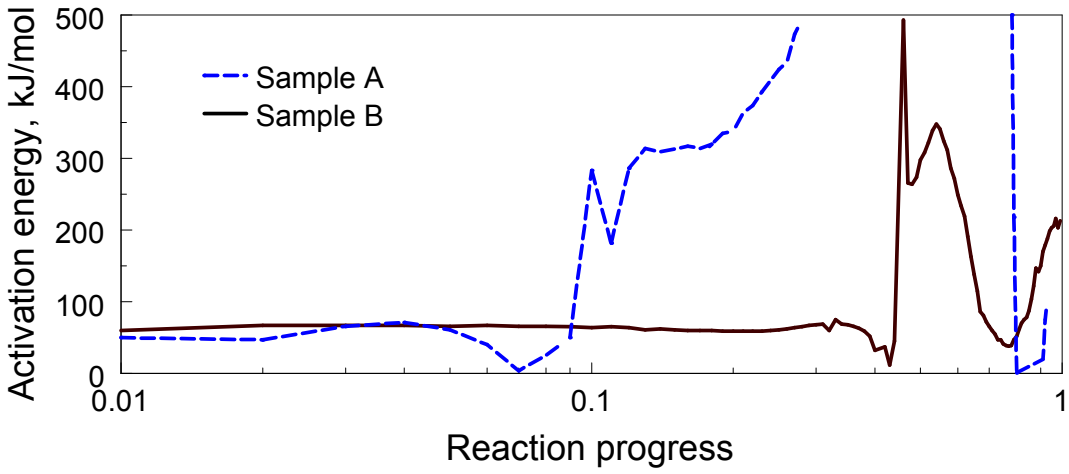


**Figure 3.6** Activation energy in function of reaction progress for samples A and B calculated using Vyazovkin method [56, 58]. Note the logarithmic horizontal scale.

### 3.4.2 Oxidation

Oxidation of samples A and B was characterized by TGA at different heating rates in both an argon-oxygen mixture and pure oxygen; the results are shown in Figure 3.7. The mass changes result from the combined effects of iodine release (mass loss) and oxidation (mass gain). For all samples the mass keeps decreasing upon heating to 673 K (400 ºC). In general there are four oxidation steps for both samples spread over broad temperature ranges from 673 to 1373 K, which are better observed in the derivatives of mass change during oxidation (Figure 3.8). The first step starts around 673 K (400 ºC) with a slight weight gain. For sample B, the first step is not clearly seen from Figure 3.7 and Figure 3.8 because the mass loss due to iodine release offsets the mass gain due to oxidation. The second step starts around 873 K (600 ºC) where the sample mass sharply increases. The third step seems to be related to aluminum melting and does not shift with heating rates, unlike thermally activated reaction steps. As the heating rate increases, the second step shifts to higher temperatures and merges with the third step associated with Al melting. In the fourth step, oxidation occurs over a broad temperature range starting from 1073 K (800 ºC). For sample B the fourth step ends around 1373 K (1100 ºC); for sample A the end point is beyond the measured temperature range. Note that the weight increase is measured only when the weight gain from oxidation exceeds the weight loss from iodine release. Thus, the oxidation may be faster than what is directly implied by the measured weight gain.

The positions of the *dm/dT* peaks shifting to higher temperatures at greater heating rates were processed using the Kissinger method [57-59] to evaluate activation energies for different oxidation steps. Different oxidation steps were resolved better for different samples, respectively, so this processing was somewhat incomplete. The activation energies identified by this processing are shown in Table 3.1.

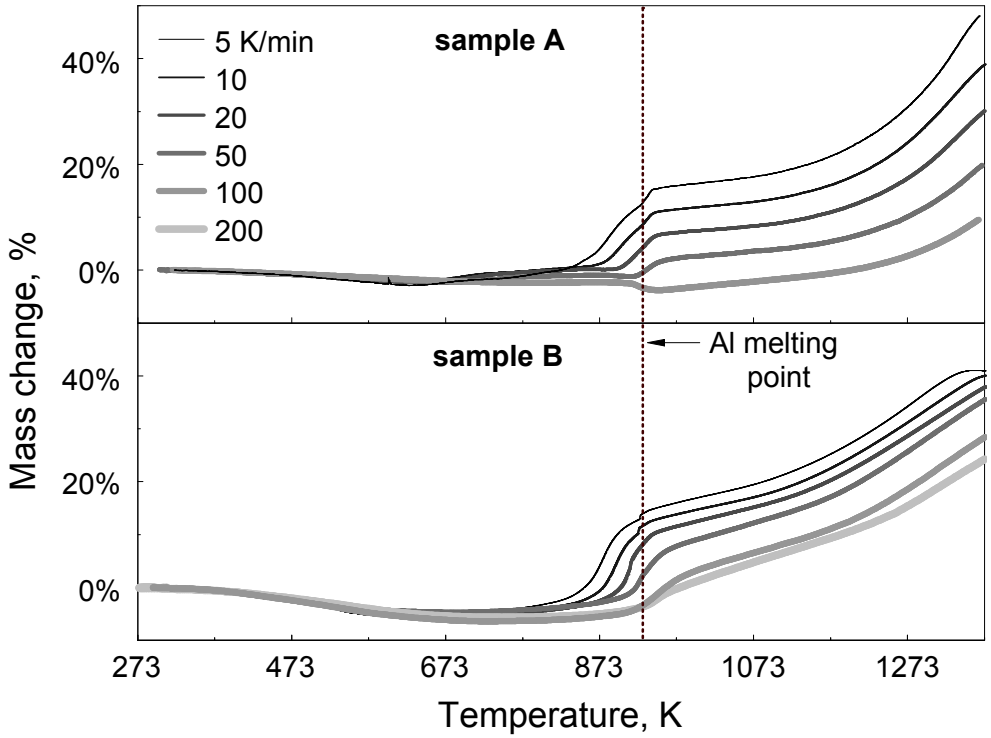


**Figure 3.7** Oxidation trace for sample A and B in TGA at different heating rates. The oxidation of sample A was measured in pure oxygen; the oxidation of sample B was measured in argon and oxygen mixture.

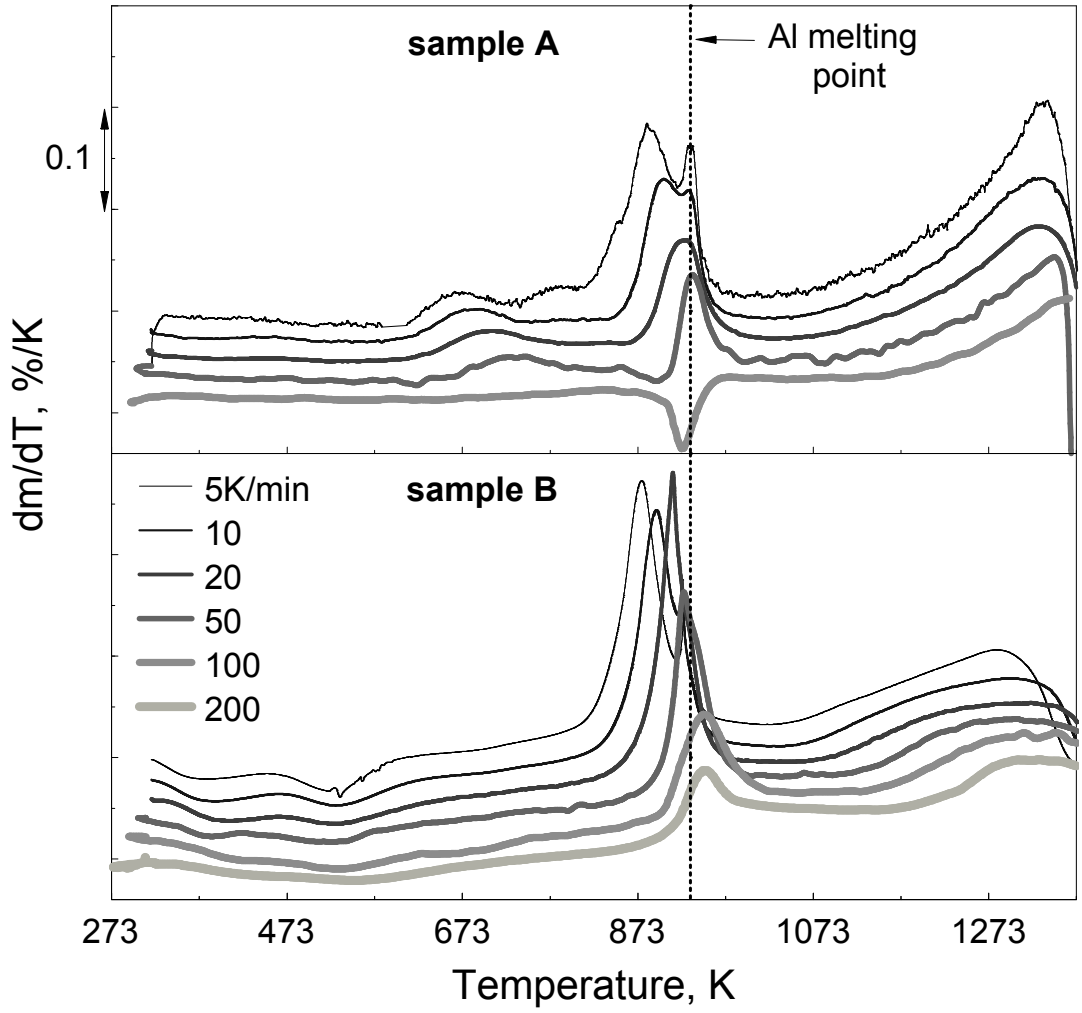


**Figure 3.8** Derivative of mass change for oxidation of sample A and B at different heating rates.

**Table 3.1** Activation Energies, kJ/mol, Determined by Kissinger Processing for Different Oxidation Steps for Al-$I_2$ Composites.

| Sample ID | A | B |
|---|---|---|
| Oxidation step | | |
| 1 | 144 | - |
| 2 | 289 | 287 |
| 4 | - | 506 |

To understand processes occurring during oxidation, XRD patterns were collected from powders by quenching sample B heated to 298, 803, 913, 953 and 1473 K. A low-background quartz sample holder was used to characterize small batches of material recovered after heating to intermediate temperatures. Figure 3.9 shows the respective XRD patterns and the pattern of as-milled sample as reference. For this sample, peaks of iodine or iodine-containing phase cannot be clearly seen, and no iodine-containing phase was detected unambiguously as oxidation went on. Only aluminum reacting to form γ-alumina and α-alumina was observed from the XRD patterns.

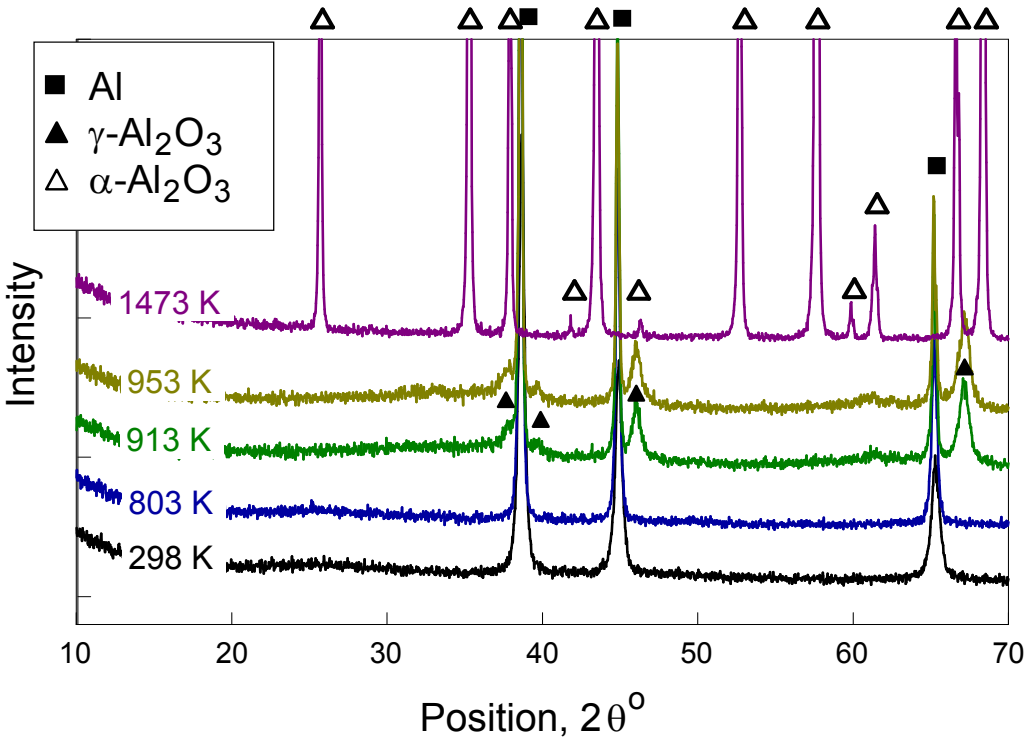


**Figure 3.9** XRD patterns of the powders produced by heating sample B in argon and oxygen mixture to and quenching at different temperatures.

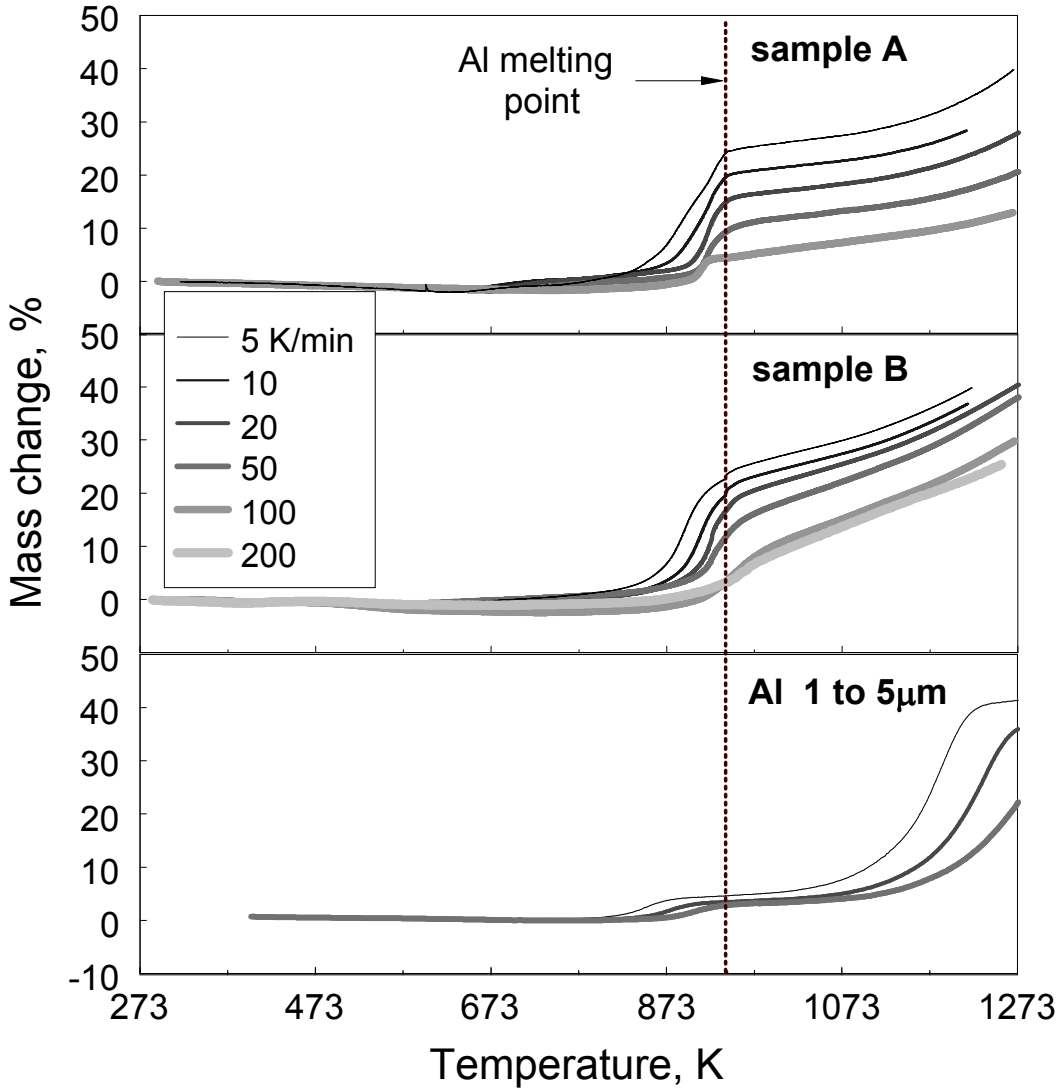


**Figure 3.10** The TGA oxidation traces of Al-$I_2$ composites from which a TGA signal measured during heating the same samples in argon are subtracted (top) and TGA traces for the pure Al oxidation (bottom).

To directly compare oxidation of Al-$I_2$ composites with that of aluminum, the oxidation TGA traces shown in Figure 3.7 were processed by subtracting the iodine release TGA traces recorded for the same material at the same heating rate in argon, as shown in Figure 3.4. The final processed oxidation traces for samples A and B are

shown in Figure 3.10. In addition, several oxidation traces directly measured for a pure Al powder are shown for comparison. A slow decrease in the processed TGA signal during the temperature ramp up to about 623 K (350 ºC) means that the iodine release at these low temperatures was slightly accelerated in the oxygen environment.

Although weight loss (dominated by the iodine release) was observed around the Al melting point for 100 K/min in the original oxidation trace (Figure 3.7), the weight gain due to oxidation becomes noticeable after subtraction of the TGA curve measured in argon. Compared to the pure aluminum oxidation, oxidation for the composite materials starts at a lower temperature (673 K) and a distinct oxidation event occurs around the aluminum melting point. It is apparent that oxidation for Al-$I_2$ composites is generally accelerated compared to pure aluminum.

### 3.4.3 Ignition

Figure 3.11 illustrates the ignition temperature measurements and shows a temperature trace corresponding to a specific setting of the electric circuit and a photodiode signature for Al-$I_2$ sample undergoing ignition. A photodiode signal for the blank filament without powder is also shown by Figure 3.11 as a reference. The calibrated temperature range for the pyrometer is 273 – 1200 K. For Al-$I_2$ powder, the ignition results in a sharp spike in the photodiode signal, which is observed at about 0.329 s in Figure 3.11. At this time, the pyrometer output is within the calibrated range, and the ignition

temperature is measured directly. For some runs ignition moment is beyond the calibrated pyrometer range; in such cases an extrapolation of the filament temperature based on the temperature ramp measured in the calibrated range is used. A linear extrapolation of the temperature ramp for the range of temperatures of interest in these experiments was supported by a detailed analysis of the heat transfer for the electrically heated filament placed in a convective environment[55].

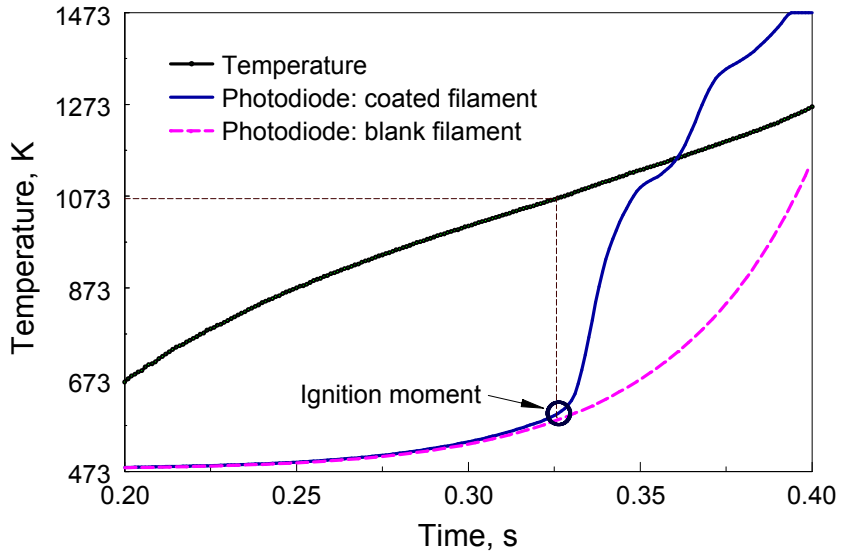


**Figure 3.11** Photodiode and temperature traces recorded during heated filament ignition experiment of Al-$I_2$ composites. A blank filament without any powder coating was heated and the photodiode signal was recorded as a reference.

The filament ignition experiments were performed in air at different heating rates varying in the range of 1,000 to 220,000 K/s. Sample B exhibited clear ignition signatures and the time of ignition was readily detected by the photodiode. For sample A, clear ignition signatures were observed at heating rates from 5,000 to 8,000 K/s. For

lower heating rates, (around 2,500 K/s) or higher heating rate (around 12,000 K/s), ignition of sample A could not be easily detected by the photodiode. A high speed video camera was used to aid in identifying the ignition moment. Figure 3.12 shows image sequences for the ignition or sample A at low and high heating rates, respectively. As the filament is heating up, the coating surface looks darker than the uncoated filament, which may be attributed to the temperature gradient (the coated portion of the wire has a greater heat capacity, and so it is heated to a lower temperatures compared to the blank wire.) In addition, the emissivity of the coating may be different from that of the clean wire surface. Note that the coated portion of the filament appears darker than the clean surface at the high heating rate (right in Figure 3.12) compared to the low heating rate (left in Figure 3.12), consistently with an expected stronger temperature gradient at the increased heating rates.

For the heating rate of 2,500 K/s, ignition is identified when a first bright spot is detected on the filament (cf. left in Figure 3.12). As time goes on, multiple bright spots appear and ignition propagates over the coating. When the coated filament is heated at a heating rate of 12,000 K/s (right in Figure 3.12), the time of ignition is identified when multiple bright particles appear to be lifted off the filament. This event always begins at the edges of the coated section of the wire, where the temperature is expected to be higher and closer to that measured by the pyrometer. It is interesting that a visible smoke cloud is observed to be produced just before the ignition, as seen in the image

shown on the right in Figure 3.12. Similar smoke clouds are observed in the video-images for the wire ignition experiments performed at heating rates of 8,000 – 12,000 K/s. This observation is hypothesized to be associated with iodine release and mass-spectrometric identification of the emitted species could be of interest in the future.

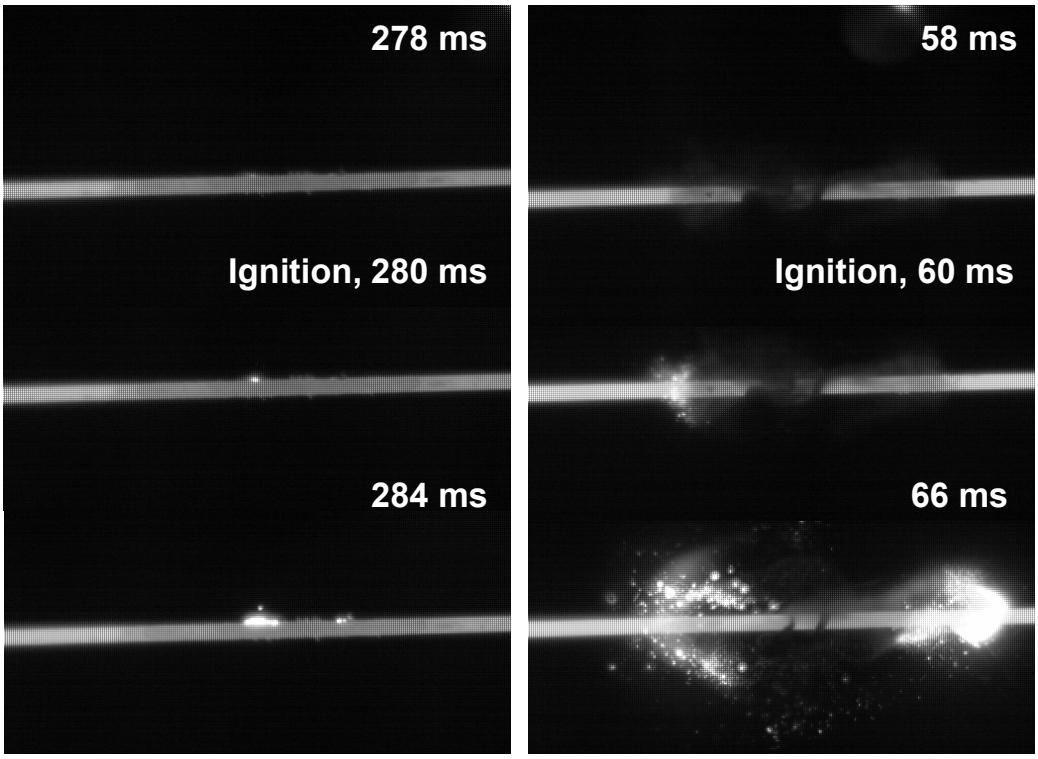


**Figure 3.12** Images recorded by the high speed camera for sample A undergoing ignition at 2,500 K/s (left), and at 12,000 K/s (right). The filament diameter is 0.5mm. The time delay for each frame is noted in the image.

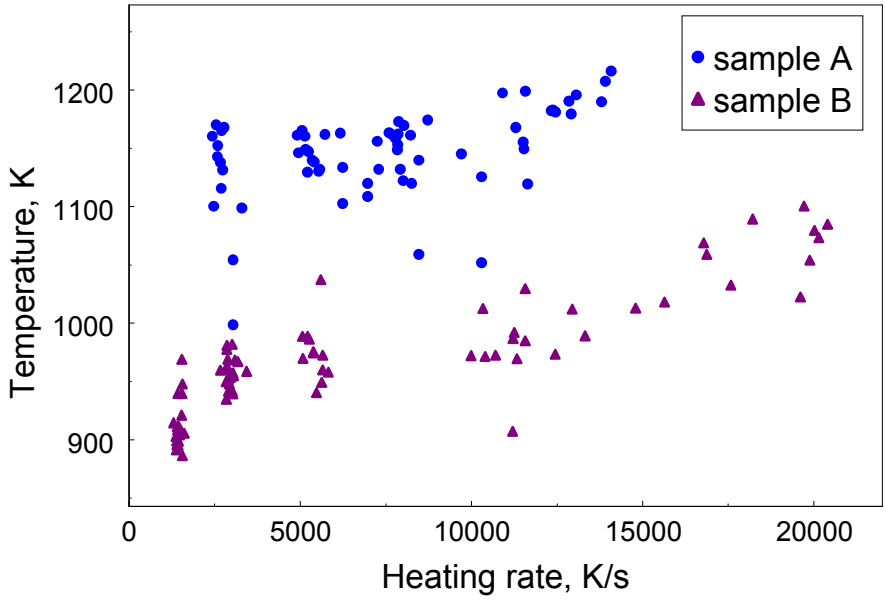


**Figure 3.13** Ignition temperatures measured for samples A and B at different heating rates.

Figure 3.13 shows the ignition temperatures of Al-$I_2$ composites as a function of heating rate. In general it is observed that the ignition temperatures of the Al-$I_2$ composites increase with increasing heating rates as is expected for a thermally activated ignition mechanism. The scatter of data might be due to the inconsistency of experimental conditions including powder coating, filament diameter and heating program. Ignition temperatures measured for sample B are somewhat lower, and ignition can be observed in a wider range of heating rates compared to sample A. The difference in the ignition temperatures measured for samples A and B is relatively small and can be caused by a difference in the particle size distributions for the two materials (cf. Figure 3.2). The difference between the particle temperature and the filament

temperature may be smaller for finer particles (sample B), explaining a small decrease in the measured ignition temperature compared to sample A.

### 3.5 Discussion

The results suggest that iodine is retained in the mechanically milled Al-$I_2$ composites in at least three different forms. The correlation of temperatures for two initial iodine release steps (the first stage) with the volatilization temperatures of pure iodine and $AlI_3$ [53, 60] suggest that fractions of the iodine retained in Al can be described as representing elemental iodine and $AlI_3$, respectively. These compounds are only weakly bound to aluminum and, similarly to the respective separate phases of I and $AlI_3$, are volatilized upon moderate heating. It is expected that these compounds would result in relatively rapid aging and partial deterioration of the prepared composites upon storage and handling. Thus, sample A, releasing less iodine at low temperatures is considered to be more suitable for practical formulations. Iodine retained in the prepared materials at elevated temperatures and released just before, during, and after Al melting is strongly bound to Al and is expected to survive storage and handling of these materials. The state of this iodine is unknown. It is possible that iodine is dissolved in the Al crystal lattice or present as surface-stabilized nano-inclusions of pure iodine or $AlI_3$ embedded into aluminum matrix.

The differences in relative fractions of the iodine contained as weakly and strongly bound forms between samples A and B represent the major difference between these two materials. Indeed, quantitative differences in the iodine release and oxidation behaviors between these two samples can be readily traced to the difference in the weakly and strongly bound iodine forms. At the same time, qualitatively, the samples behave similar to each other, including consistency in the apparent activation energies assigned to different reactions.

Increasing the concentration of iodine strongly bound to Al while reducing the concentrations of the weakly bound forms behaving as pure iodine and $AlI_3$ are identified as objectives of further synthesis efforts aimed at development of practically useful Al-$I_2$ composites.

It is interesting to consider whether the detected stages and steps of iodine release are correlating with the oxidation steps for the prepared materials. It is apparent that the first iodine release stage occurring at low temperatures does not directly correlate with the observed oxidation steps. Similarly, the initial oxidation step with the onset close to 673 K (400 ºC) is not associated with any specific iodine release step. It is worth emphasizing that this initial oxidation step occurs earlier than for pure Al (cf. Figure 3.9) and so the low-temperature oxidation rate for aluminum is clearly affected by the presence of iodine. Because no crystalline alumina phases are detected for the partially

oxidized materials (Figure 3.9), amorphous alumina is the likely product of oxidation at these temperatures, as is the case for pure Al [61].

The second stage of iodine release does appear to correlate with the second oxidation step for Al-$I_2$ composites. In both cases, the reactions start at about 773 – 873 K and in both cases, the activation energies are found to be close to 300 kJ/mol. Aluminum melting also apparently interferes with both iodine release and the oxidation processes. Oxidation at these temperatures produces well-detectable quantities of $\gamma$-$Al_2O_3$. This product is also consistent with that observed for oxidation of pure Al at the same temperatures [62]. Further oxidation results in formation of $\alpha$-$Al_2O_3$, again, consistently with the oxidation of pure Al. Note that pure Al in $O_2$ does not oxidize appreciably immediately following its melting, while the oxidation rate increases rapidly at elevated temperatures. Conversely, Al-$I_2$ composite materials oxidize relatively fast at the Al melting point. The oxidation rate increases only slightly (slower than for the pure molten Al) as the temperatures increase. The acceleration in the pure aluminum oxidation upon melting has been previously observed in the presence of $H_2O$ as an oxidizer [63]. It was hypothesized that presence of hydrogen alters properties of the protective alumina film resulting in disruption of its continuity when molten Al forms. It is possible that the presence of iodine has a similar effect on properties of alumina. It is also possible that iodine bound to crystalline Al is rapidly released upon Al melting;

the release of gaseous iodine results in disrupting the alumina shell, which in turn leads to an enhanced transport of oxygen to the fresh aluminum surface.

Finally, it is interesting to consider possible correlations between the ignition kinetics and those of the various observed iodine release and oxidation events. Figure 3.14 shows ignition temperatures measured at different heating rates presented in the same Kissinger plot as the *dm/dT* minimum and maximum temperatures corresponding to individual iodine release and oxidation events, respectively. The kinetic trends following from TGA measurements are extrapolated as straight lines into the range of heating rates corresponding to the ignition experiments. It is apparent that the second iodine release step (corresponding to the release of the $AlI_3$-like form of iodine) correlates with the ignition data better than any other reactions observed in the TGA experiments. This observation is consistent with the observed "smoke" produced by the sample coated onto the heated filament just prior to its ignition (Figure 3.12); the smoke may be formed by air moisture reacting with the generated iodine cloud. The second stage of iodine release, not shown in Figure 3.14, but effectively coinciding with step II of oxidation is projected to higher temperatures than the experimental ignition temperatures determined here.

Thus, it is suggested that the second iodine release step may accelerate the oxidation process and lead to ignition of the materials. Thus, reducing the weakly

bound iodine forms in more stable materials can also alter their ignition behavior, which should be addressed in the future efforts.

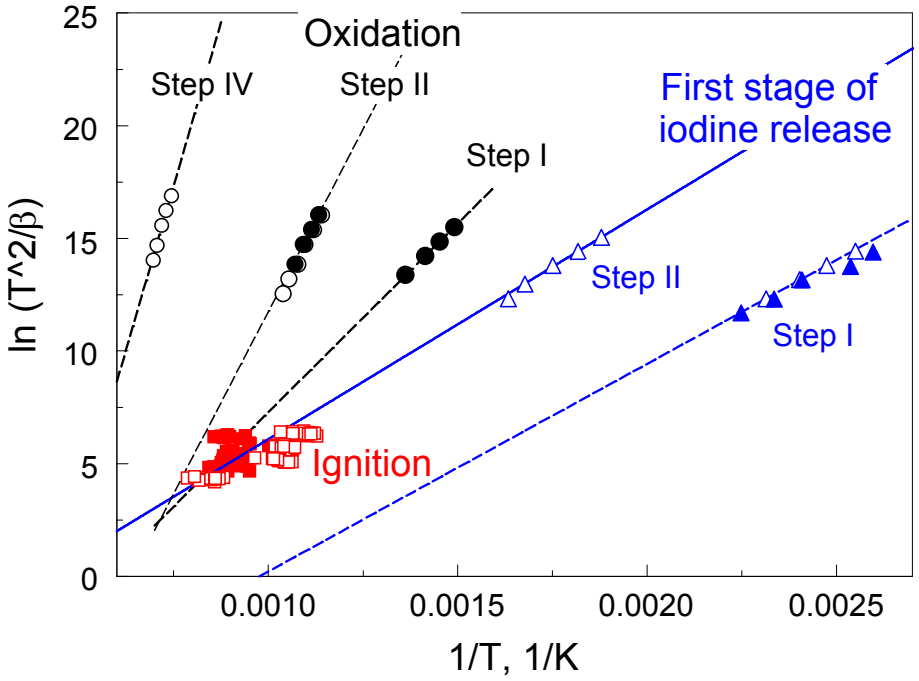


**Figure 3.14** Comparison of ignition temperatures measured at different heating rates with iodine release and oxidation steps observed in the TGA traces. Filled symbols represent sample A; open symbols represent sample B. Circles represent oxidation steps, triangles represent iodine release steps, and squares show ignition temperatures.

## 3.6 Conclusions

Mechanical milling at cryogenic temperatures is successfully applied to prepare Al-$I_2$ composite powders with iodine concentrations exceeding 10 wt. %. Detailed TGA measurements suggest that iodine is present in the prepared composites in at least three different forms. Two weakly bound forms volatilize similarly to elemental iodine and

$AlI_3$. A strongly bound form is retained in aluminum until the material is heated up to nearly the Al melting point. Two different samples prepared in this effort contained different fractions of weakly and strongly bound iodine forms; however, the iodine release and oxidation behaviors were qualitatively similar for both samples. Oxidation of the prepared materials in $O_2$ occurs in several steps clearly distinguished by TGA. The low-temperature oxidation begins sooner than for pure aluminum. The second oxidation step is correlating with the release of strongly-bound form of iodine. Unlike for pure aluminum oxidizing in $O_2$, the second oxidation step is accelerated by Al melting. Ignition of the prepared materials occurs at substantially lower temperatures than for pure Al. It is observed that for the materials prepared in this study, the ignition kinetics likely correlates with that of the low-temperature release of iodine.

# CHAPTER 4

# OXIDATION, IGNITION AND COMBUSTION OF Al-$I_2$ COMPOSITE POWDERS

## 4.1 Introduction

Recent interest in energetic materials generating biocidal combustion products capable of inactivating aerosolized microorganisms prompted research on novel fuels and oxidizers containing halogens [47, 64, 65]. It is desired to release maximized quantities of halogen-containing combustion products while minimizing any possible negative impact of modification of the energetic formulation on its combustion performance. It is also important that the modified ingredients and formulations are convenient to store and handle. In this chapter, continuing Chapter 2 and 3 the focus is on development and characterization of Al-$I_2$ composite materials. Such materials are expected to combine attractive combustion characteristics of aluminum powders with a capability to release iodine or iodine-containing reaction products. The Chapters 2 and 3 showed feasibility of preparing Al-$I_2$ composite materials by cryomilling [60, 66]. Reactions occurring in such materials upon their heating in inert and oxidizing environments were investigated in Chapter 2 and 3, where work was restricted to materials containing 10 wt. % of iodine. In this chapter, materials with an expanded range of iodine concentrations are prepared and characterized. In addition to thermo-analytical and ignition measurements, experiments directly investigating combustion of the prepared materials as aerosolized clouds and as

individual particles are reported. The goals of this chapter are to better characterize ignition kinetics and combustion dynamics of the Al-$I_2$ composite materials prepared by cryomilling, and identify materials combining stability, maximized iodine concentration, and attractive combustion performance.

## 4.2 Materials

Al-$I_2$ composite powders with different iodine concentrations were prepared by cryomilling elemental aluminum and iodine using a model 01HD attritor mill by Union Process. Starting materials were aluminum powder, -325 mesh (< 45 μm), 99.5% pure, by Atlantic Equipment Engineers and iodine chips, 99% pure, by Sigma Aldrich. The mean size of aluminum powder is 25 μm. 1.8 kg of 10 mm diameter hardened steel balls served as milling media. A 750-ml steel milling vial was continuously flushed with gaseous nitrogen. Liquid nitrogen was flushed through the cooling jacket of the milling vial. In all experiments, ball-to-powder mass ratio was 36 and the impeller rotation rate was set to 400 rpm. Further details describing material preparation are given in Chapter 2 and 3.

Five different samples were studied in this chapter. Samples A and B (cf. Chapter 3) had the nominal iodine concentration of 10 wt. %. Sample A was continuously milled for 10 hours. Sample B was prepared by two-step milling, which included milling for 6 hours with conditions described above, followed by an additional 3.5-hour long milling

step with liquid nitrogen fed into the milling vial. Samples C, D and E were milled continuously for 25 hours and contained, respectively, 15, 20 and 30 wt. % of iodine.

**Table 4.1** Prepared Al-$I_2$ Composite Powders

| Sample ID | Mass ratio (Al/I) | Milling time, h | Milling protocol |
|---|---|---|---|
| A | 90/10 | 10 | Liquid $N_2$ in cooling jacket |
| B | 90/10 | 9.5 | 2-step cryomilling (see text) |
| C | 85/15 | 25 | Liquid $N_2$ in cooling jacket |
| D | 80/20 | 25 | Liquid $N_2$ in cooling jacket |
| E | 70/30 | 25 | Liquid $N_2$ in cooling jacket |

Size distributions of the prepared powders were measured using a Beckman-Coulter LS230 Particle Counter. Figure 4.1 shows the particle size distribution (PSD) and respective volume mean particle sizes of all the samples. Note that sample A appeared coarse as prepared and therefore it was sieved prior to all experiments, which explains an abrupt drop in the volume fraction for particles coarser than about 60 μm for that sample. Sample E included many fine particles and tended to agglomerate, causing the bimodal size distribution observed for that sample. The second peak produced by the agglomerated particles was discounted in order to estimate the volume mean particle size shown in Figure 4.1.

All samples consist of generally equiaxial, micron-sized particles. The morphologies of samples C, D and E are illustrated in back-scattered SEM images shown in Figure 4.2. SEM images of samples A and B were presented elsewhere. Particle

shapes are similar for different powders. With an increase in the iodine concentration, the number of fine particles increases.

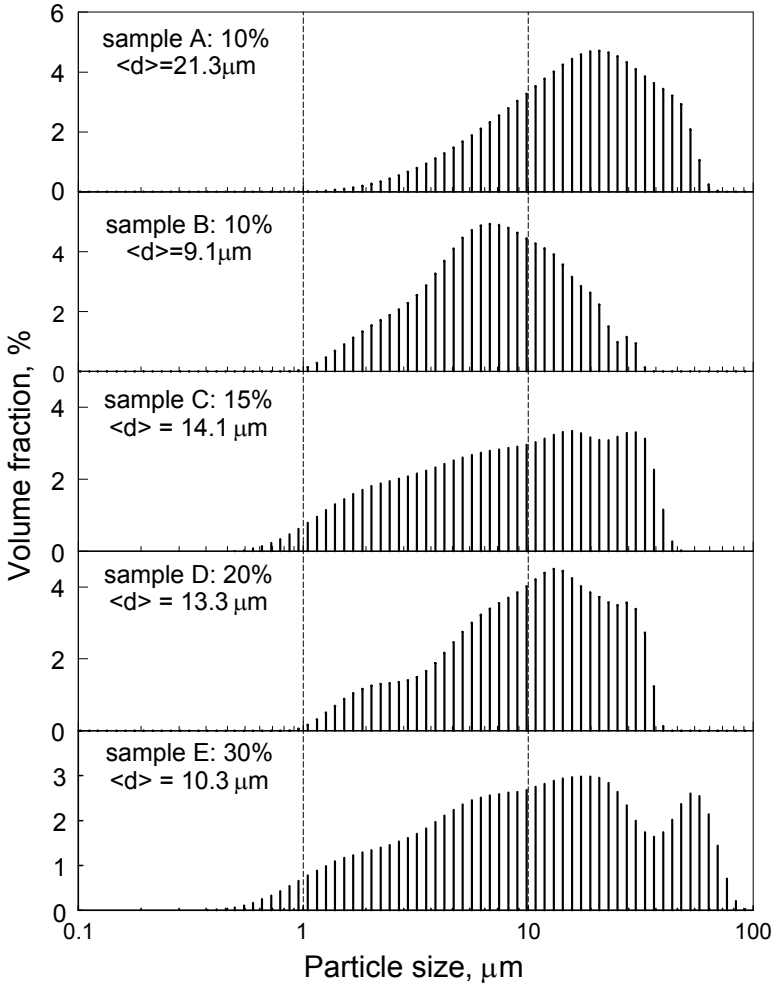


**Figure 4.1** Particle size distributions for the prepared composite powders. Volume mean particle sizes are shown for each material.

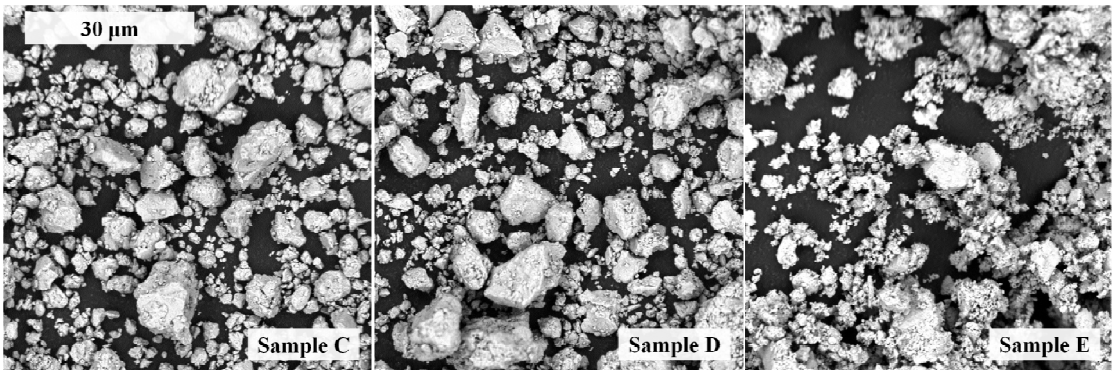


**Figure 4.2** SEM images of powders in samples C, D and E. The scale bar is the same for all the pictures.

## 4.3 Experimental

Iodine release and oxidation were measured by a TA Instruments model Q5000IR thermogravimetric analyzer (TGA). The amount of iodine embedded in composites is clearly shown by the total weight loss from TGA results. Alumina pans were used to hold samples for the measurements. The maximum temperature was limited to 1273 K. Experiments were performed at heating rates varied from 5 to 100 K/min. For iodine release and oxidation measurements, the experiment conditions are the same as shown in Chapter 3.

Ignition of the prepared materials was studied in air at heating rates ranging from 1000 K/s to 22000 K/s using an electrically heated filament [32, 67]. Ignition instant was identified from videos recorded at 500 fps using a high speed camera (MotionPro 500 by Redlake). The temperature at the ignition instant was determined as a function of the heating rate.

Combustion of the Al-$I_2$ composite powders in air was studied using a constant volume explosion (CVE) experiment [68]. A simplified diagram of the experiment setup is shown by Figure 4.3. A nearly spherical, 9.2-liter explosion vessel was initially evacuated. Composites were aerosolized and introduced into the vessel with an air blast delivered from a high-pressure reservoir. After a short delay, aerosolized powder was ignited by an electrically heated tungsten wire placed in the center of the vessel. The pressure trace was recorded by a pressure transducer. The ratio of the maximum pressure over the initial pressure and the maximum rate of pressure rise were used to gauge the energy released in each experiment and the rate of combustion, respectively. Samples B, C, D and E having comparable particle sizes were tested by this technique with a constant powder load (4.65 g), corresponding to fuel-rich conditions for all samples. This mass was selected to be the same as in multiple reference experiments with pure Al powders of different particle sizes [68]. Experiments with each material were repeated at least three times. CVE results for similarly sized pure aluminum powders were used for reference.

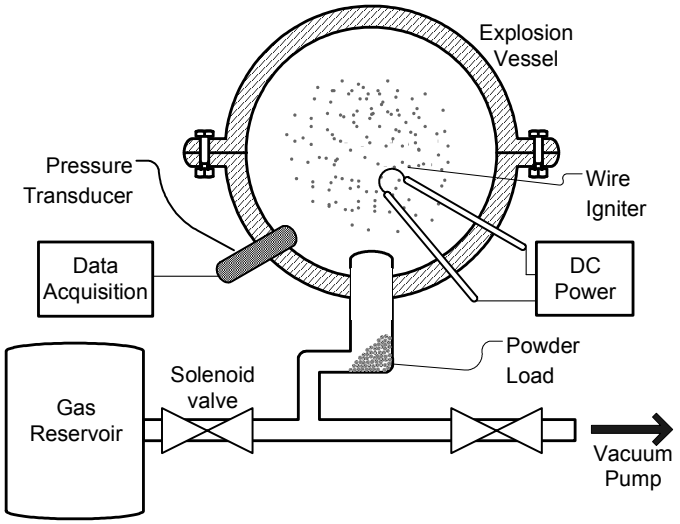


**Figure 4.3** Schematic diagram of the constant volume explosion apparatus.

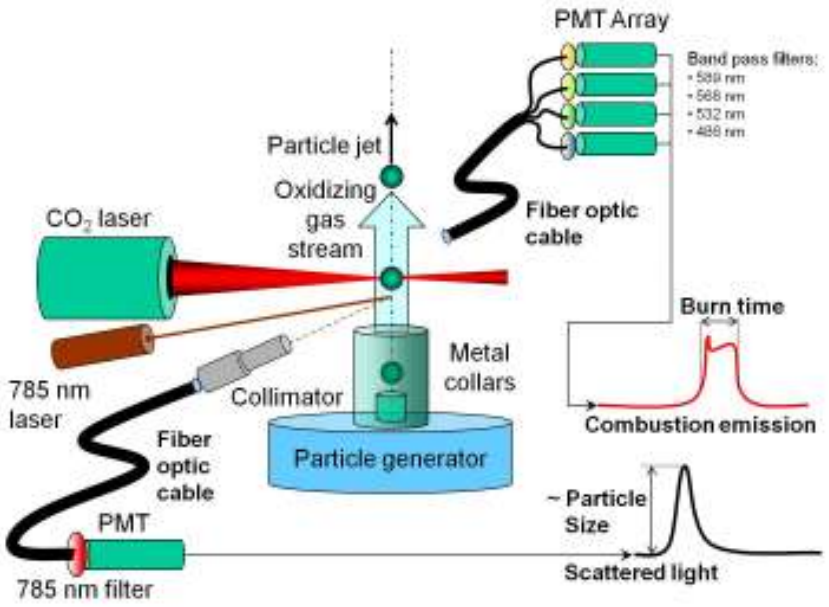


**Figure 4.4** Experimental apparatus and diagnostics for single particle combustion with in situ size measurement.

Burning characteristics of individual composite particles were investigated using a laser ignition apparatus illustrated in Figure 4.4 [69-72]. Individual particles were fed by an air flow into a $CO_2$ laser beam, where they were ignited. Flow settings were

selected so that for all materials the measured average particle velocities were close to 0.7 m/s. Before ignition, particles crossed a beam of a 785 nm, 30 mW laser and the scattered light pulses were used to measure particle sizes in-situ. Luminous streaks produced by ignited particles were photographed. Four photomultiplier tubes (PMT, Hamamatsu H3164-10) were used to record the light emission from particle burning. The photomultiplier tubes were equipped with interference filters (486, 532, 568, and 589 nm). Separate measurements using an EPP2000 High Resolution Spectrometer by StellarNet Inc were performed to verify that the particle emission did not include a parasitic sodium line at 589 nm. 532 and 589 nm filters were used for combustion temperature measurement. Considering that one of the strongest molecular bands of AlO emission is at 486 nm, while no substantial AlO emission occurs at 568 nm, the strength of the observed AlO emission was evaluated using the following ratio:

$$R_{AlO} = \frac{\left(I_{486} / I_{568}\right)_{\exp}}{\left(I_{486} / I_{568}\right)_{bb}} \tag{4.1}$$

Where $I_{486}$ and $I_{568}$ are the emission intensities measured with 486 and 568 nm filters, respectively; $(I_{486}/I_{568})_{\exp}$ is the intensity ratio calculated from experiment; and $(I_{486}/I_{568})_{bb}$ is the ratio calculated for a black body when the black body temperature was equal to the measured particle temperature. The experiments for the $Al{\cdot}I_2$ composite samples A, B, C and D were performed. Because of agglomeration observed for sample E, it was not suitable for the present single particle laser ignition experiments.

The overall data processing included the following steps. Individual particle pulses were identified from the raw data of the scattered signals and the strongest emission signals (568 nm). The amplitudes of peaks of scattered light pulses were converted to particle diameter by matching peak height distribution and particle size distribution obtained from Beckman-Coulter LS230. The time shift between two lasers was identified based on the shift between the onset of emission peak and the maximum of scatter pulse. Finally, burn times from emission pulses were correlated to their corresponding sizes. Only the longest emission times measured for each range of particle sizes are considered for samples in this chapter. Shorter emission pulses are produced when particles are partially consumed in the laser beam so that these pulses are not considered to be representative of burn times of interest [69, 70].

## 4.4 Results

### 4.4.1 Iodine Release

Figure 4.5 shows the reduction of mass, $m$, and derivative of mass over temperature, $dm/dT$, for Al-$I_2$ samples heated in argon. The study in Chapter 3, which focused on materials with 10 wt. % of iodine (samples A and B) showed two main iodine release stages. The first one occurred in the temperature range of 373 – 673 K; the second one began in the vicinity of 873 K, close to the aluminum melting point. These iodine release stages were also detected for all samples prepared in this project. Iodine in

sample A is well stabilized, and it is mostly released in the second, high temperature stage. Conversely, iodine is not well stabilized in sample B, resulting in a strong initial iodine release stage. For the sample E (30 wt. % of $I_2$) the low-temperature iodine release is very strong, relatively comparable to that for sample B. This may indicate an upper limit for the encapsulation of iodine in an aluminum matrix. Alternatively, longer milling times might be necessary to reduce the low-temperature iodine release at higher iodine concentrations. However, longer milling times were considered impractical and were not attempted. At high temperatures (~ 1173K), a slight mass increase for sample E was observed that was likely caused by oxidation with residual oxygen.

For the samples C and D, (with 15 and 20 wt. % of $I_2$, respectively) an additional iodine release stage was observed between the two stages mentioned above. It began at 683 K for sample C, and at 653 K for sample D.

For all samples, except for sample E, the final weight measured after the end of heating was close to that expected based on the nominal material composition reduced by the entire iodine content for each sample. The discrepancy in the final weight of sample E and that expected based on its nominal starting composition may be associated with an incomplete incorporation of iodine into the aluminum matrix. Longer milling times possibly could have increased the efficiency of iodine incorporation into aluminum. In addition, reaction with residual oxygen (an undesired experimental effect) and causing

the observed weight increase at high temperatures could have further contributed to the discrepancy between the observed and expected final weights for sample E.

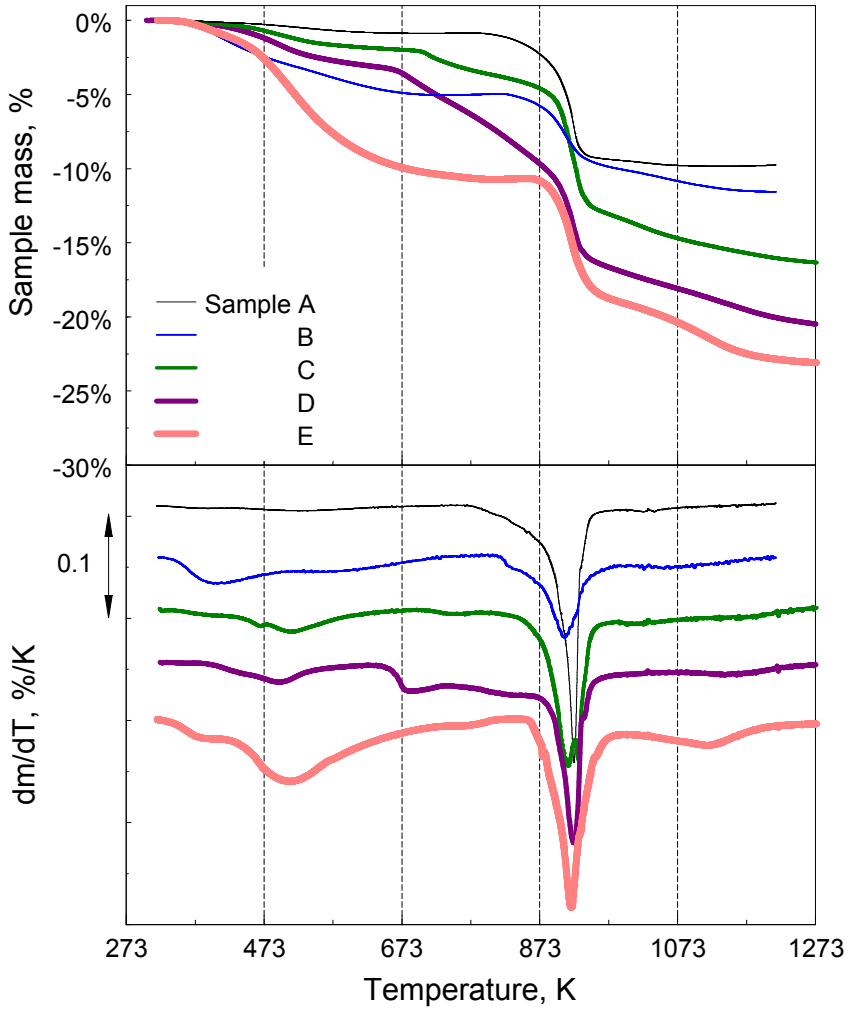


**Figure 4.5** Mass change and derivative traces (shifted along the vertical axis for clarity) for iodine release of Al-$I_2$ samples in argon. All the samples were heated at 10 K/min.

**Table 4.2** Measure of Stability Defined by Equation (4.2) for Different Samples

| Sample ID | A | B | C | D | E |
|---|---|---|---|---|---|
| *S*, % | 91.2 | 57.9 | 87.9 | 83.0 | 57.2 |

Minima in the *dm/dT* traces shown in Figure 4.5 illustrate further the observed iodine release stages. The intermediate iodine release stage well visible in the TGA traces for samples C and D, is represented by a minimum shifting to higher temperatures for lower iodine concentrations: it is observed at about 678 K for sample D and at about 743 K for sample C. It is possible that this stage merges with the following stage for sample B, resulting in the observed feature in its *dm/dT* trace in the vicinity of 823 K. The *dm/dT* trace of sample C shows that the initial iodine release stage can be split into two steps as two minima in the temperature range of 373 – 673 K are visible. However, the first step occurs at a very low temperature and the steps are hard to distinguish for most samples, so these features were not analyzed further.

For all samples, the high temperature iodine release stage overlaps with Al melting. Melting accelerates iodine release for all samples, resulting in a clearly distinguished feature in all the *dm/dT* traces.

A relative measure of the material stability, *S*, is introduced comparing the total mass of iodine contained in the sample (equal to the total weight loss measured in the TGA, $W_{total}$) with the weight loss at the temperatures exceeding 673 K, $W_{T>673K}$, i.e., after the first major low-temperature iodine release stage:

$$S = \frac{W_{T>673K}}{W_{total}} \cdot 100\% \tag{4.2}$$

The values of *S* for all samples are shown in Table 4.2.

Kinetics of the iodine release stages were studied by tracking the main minima positions while heating samples C and D (for which all three stages were observed) at different rates from 5 to 100 K/min. These results are discussed below, in the Reaction kinetics section. Note that kinetics of iodine release for the samples with 10% $I_2$ was studied in Chapter 3.

### 4.4.2 Oxidation

TGA traces and their derivatives for oxidation of Al-$I_2$ samples are shown in Figure 4.6. The mass changes result from the combined effects of iodine release (mass loss) and oxidation (mass gain). All materials are losing weight upon initial heating, and a four-step oxidation including a sharp oxidation step coinciding with the Al melting is observed at higher temperatures for all materials except for sample E, for which the oxidation behavior is masked by strong iodine release. Consistently with the iodine release measurements (Figure 4.5), the initial weight loss is much stronger for sample E compared to other materials. The oxidation results in only one clearly distinguished peak in the *dm/dT* trace for that sample.

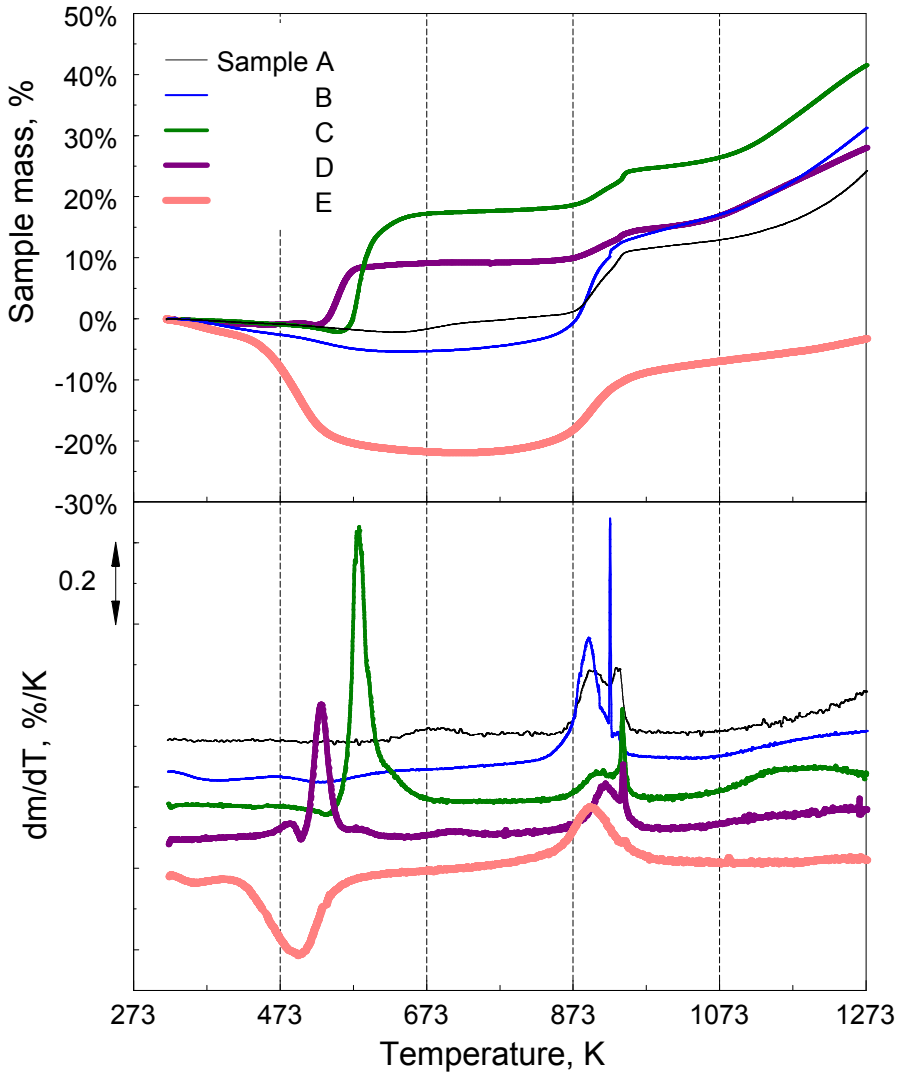


**Figure 4.6** Mass change and derivative traces for oxidation of Al-$I_2$ samples in pure oxygen at heating rate of 10 K/min.

Comparing the *dm/dT* traces for samples A, C, and D, for which the first oxidation peak is well distinguished, one observes how that peak shifts to lower temperatures for higher iodine concentrations. It is interesting that the weight gains for the first oxidation stage for samples C and D (with 15 and 20 wt. % of $I_2$, respectively) are more significant than those for samples A and B, both containing 10 wt. % of $I_2$.

For sample D, oxidation appears to begin prior to the first iodine release stage, so that the minimum in the *dm/dT* trace is overlapped with the onset of the first oxidation peak, resulting in a superficial additional maximum just above 473 K. For sample C, the first oxidation peak shifts to higher temperatures and the additional maximum is no longer observed. There is no obvious effect of iodine concentration on the positions of other oxidation steps.

### 4.4.3 Ignition

Figure 4.7 shows the ignition temperatures of Al-$I_2$ composites as a function of heating rate. Each point represents an individual filament ignition experiment. Ignition instant is identified using recorded videos when a first bright spot is detected on the powder coating. Despite significant scatter of the data points, a general trend is noticed showing that the ignition temperatures of the Al-$I_2$ composites increase slightly with increasing heating rates as is expected for a thermally activated ignition mechanism. The lowest ignition temperatures are observed for sample D, (20 wt. % of iodine). It is also noted that the scatter in the measured data is decreasing from sample C to E.

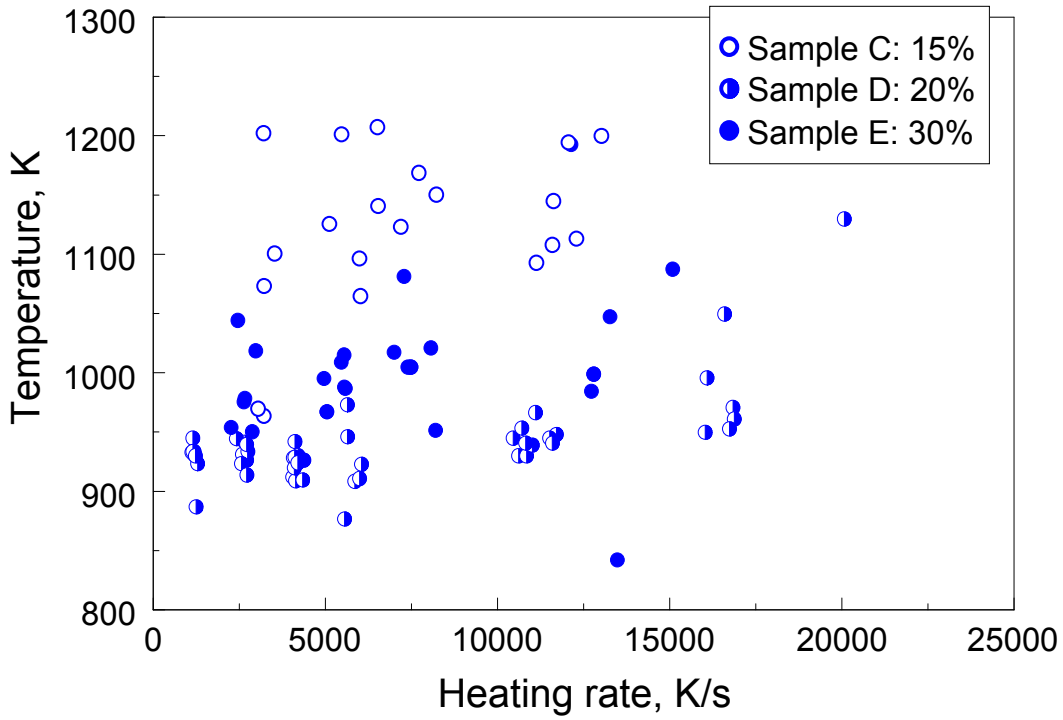


**Figure 4.7** Ignition temperatures for samples C, D, and E measured at different heating rates

### 4.4.4 Reaction Kinetics

TGA results as well as ignition results were processed using the Kissinger method [57]. Figures 4.8 and 4.9 show plots of $\ln(\beta/T^2)$, where $\beta$ is the heating rate, versus the reciprocal temperature for both, ignition temperatures and TGA *dm/dT* peak temperatures for iodine release and oxidation. Plots for samples C and D are shown separately. Similar Kissinger plots for samples A and B were presented in Chapter 2. Sample E was excluded from these comparisons because most of iodine was lost from that sample at low temperatures.

The first two iodine release stages are clearly separated and do not appear to correlate with the initial oxidation stage for both samples C and D. Conversely, the high-temperature stage of oxidation coincides with the high-temperature stage of iodine release, also for both samples C and D.

Kinetic trends implied by TGA measurements can be extrapolated as straight lines into the range of heating rates corresponding to the ignition experiments. For samples A and B, such extrapolation described in Chapter 2 suggested possible correlations between ignition and either first stage of iodine release or initial oxidation stage. Figure 4.9 suggests a correlation between ignition and the first oxidation step observed in TGA for sample D. It is also apparent that in some experiments, ignition occurred at the Al melting point, at which time both iodine release and oxidation were noticeably accelerated as well. Figure 4.8 indicates possible correlations between either of the two observed oxidation steps and ignition for sample C. It is interesting that for both samples C and D, ignition does not appear to correlate with either of the first two iodine release stages.

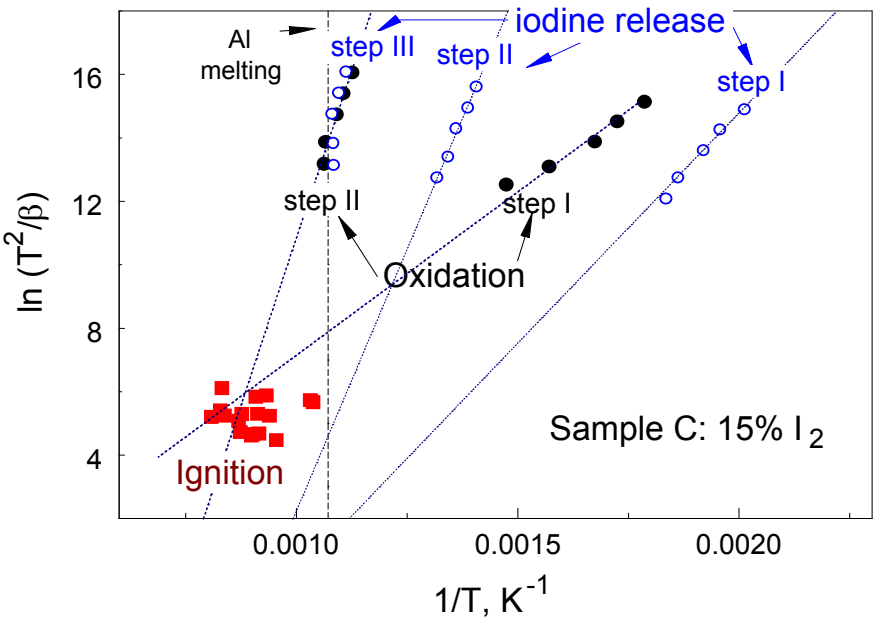


**Figure 4.8** Kissinger plot showing ignition temperatures measured at different heating rates (squares) together with peak positions for iodine release (open circles) and oxidation steps (filled circles) observed in the TGA traces for sample C.

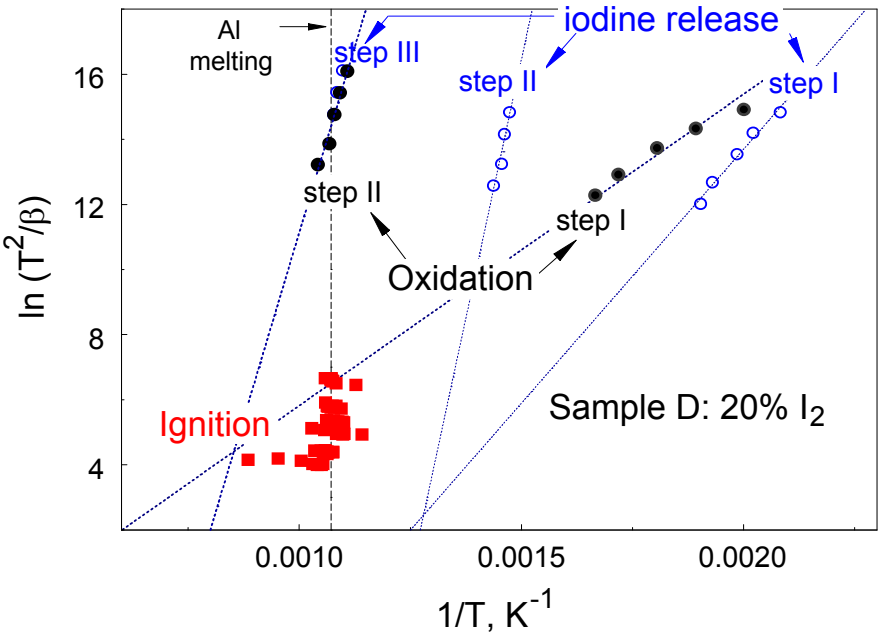


**Figure 4.9** Kissinger plot showing ignition temperatures measured at different heating rates (squares) together with peak positions for iodine release (open circles) and oxidation steps (filled circles) observed in the TGA traces for sample D.

### 4.4.5 Aerosol Combustion

Four Al-$I_2$ materials (samples B, C, D, and E) and three reference aluminum powders with comparable particle sizes were tested in CVE experiment. Sample A was excluded because of its substantially coarser particle sizes compared to other materials. Aluminum powders used had nominal sizes of 1-5 μm, 6.5 μm, and 10-14 μm. All tested samples ignited readily. Results from CVE experiments for Al-$I_2$ composites and aluminum powders are summarized in Figure 4.10. Results are presented in terms of the ratios of maximum explosion pressure, $P_{max}$, over the initial pressure in the vessel, $P_{ini}$, i.e., pressure ratios, and the maximum rates of pressure rise, $(dP/dt)_{max}$. Following earlier work, e.g., [31, 68], $P_{max}/P_{ini}$ and $(dP/dt)_{max}$ are assumed to be proportional to flame temperature and combustion rate, respectively. In order to account for the effect of particle sizes for other powders, the values of $P_{max}/P_{ini}$ and $(dP/dt)_{max}$ are plotted as a function of the volumetric mean particle size for each tested sample. The error bars indicate standard deviations from the mean values obtained from the repeated CVE experiments. For pure aluminum powder, both $P_{max}/P_{ini}$ and $(dP/dt)_{max}$ increase as particle sizes decrease. Sample B showed lower values of $P_{max}/P_{ini}$ and $(dP/dt)_{max}$ compared to pure Al with the same mean particle size. Conversely, samples C and D produced higher $P_{max}/P_{ini}$ and $(dP/dt)_{max}$, indicating a higher flame temperature and combustion rate compared to the similarly sized pure aluminum powders. Sample E

showed lower $P_{max}/P_{ini}$ and higher $(dP/dt)_{max}$ and a greater standard deviation compared to the pure Al.

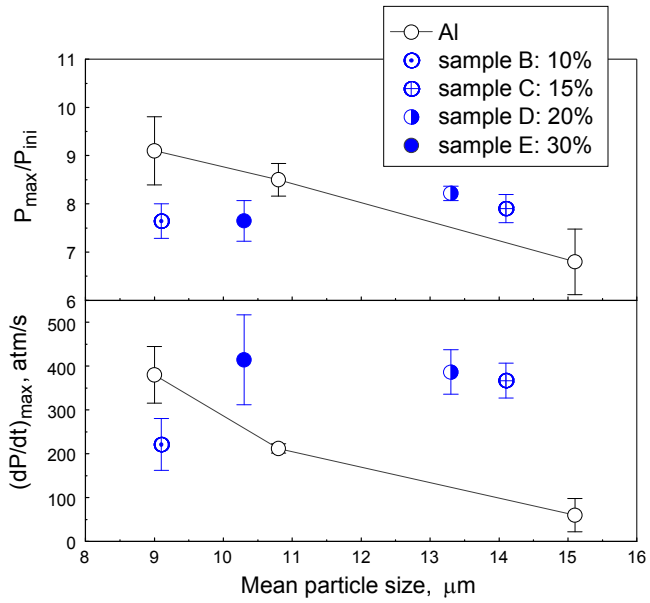


**Figure 4.10** Maximum pressures and rates of pressure rise measured in constant volume explosion tests with different materials. Results are shown as a function of the volumetric mean particle size for each powder.

### 4.4.6 Laser Ignited Particle Combustion

A photograph of laser-ignited and burning particles is shown by Figure 4.11; each streak represents a particle passed through the laser beam. The camera shutter was open for 250 ms to capture emission from a sequence of passing particles. For all particles, pronounced oscillation patterns were observed. Most particles are observed to experience fragmentation by the end of combustion. The overall emission intensity appears to increase while the particles are burning and peak just before particles fragment. For most particles, sharp turns in their trajectories are observed.

Figure 4.12 shows characteristic traces for emission, temperature, and $R_{AlO}$ for samples B, C, and D. All traces in Figure 4.12 represent particles with measured diameters close to 5 μm. The overall burn time for sample B is very close to that reported for pure Al particles [69, 70]. The burn times for other samples are somewhat longer. The emission intensity traces are shown in the logarithmic scale to better resolve changes accompanying ignition and extinction of the burning particles. The oscillatory patterns in the emission signals are stronger, more regular, and occur over longer periods of time compared to similar signals for pure, micron-sized Al particles [69, 70]. For all traces, prior to quenching the emission intensity decreases and then exhibits a short plateau, probably associated with burning particle fragments. Combustion temperatures are fairly low for sample B and do not exceed 2000 K. For samples C and D, the combustion temperatures are higher and approach 2800 – 3000 K.

Values of $R_{AlO}$ are the highest for sample B, which burns at the lowest temperature. $R_{AlO}$, defined by Equation (4.1) is normalized to the intensity ratio expected for a black body emitter at the particle temperature and thus accounts for the effect of temperature on the black body spectrum shift. Therefore the high values of $R_{AlO}$ for sample B indicate substantial vapor phase reactions of the Al-$I_2$ composites even at such low temperatures. Indeed, the values of $R_{AlO}$ are substantially greater than 1 for all samples, indicating significant vapor phase reactions.

Following the data processing methodology of ref. [70], an average temperature was calculated for each trace for the period of time when the emission signal varied within 50 and 100 % of its peak value. These average temperatures and their respective standard deviations are shown in Figure 4.13 for different Al-$I_2$ samples. Interestingly, for the range of particle sizes studied, no effect of particle size on the average combustion temperature was observed.

Laser ignition experiments were also performed for sample A; however, because that sample consisted of mostly coarse particles, the results cannot be directly compared to the data presented in Figures 4.12 and 4.13. The minimum particle size, for which combustion traces were recorded for sample A was close to 10 μm. The oscillatory emission patterns for that material were weaker than for other samples. The combustion temperatures measured for sample A were quite high, in excess of 3500 K.

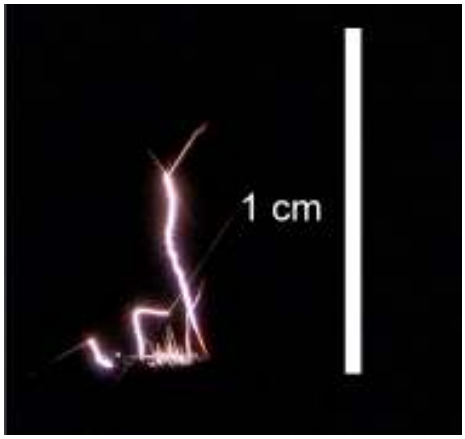


**Figure 4.11** Photograph of streaks of Al-$I_2$ particles (sample C) ignited while crossing the $CO_2$ laser beam.

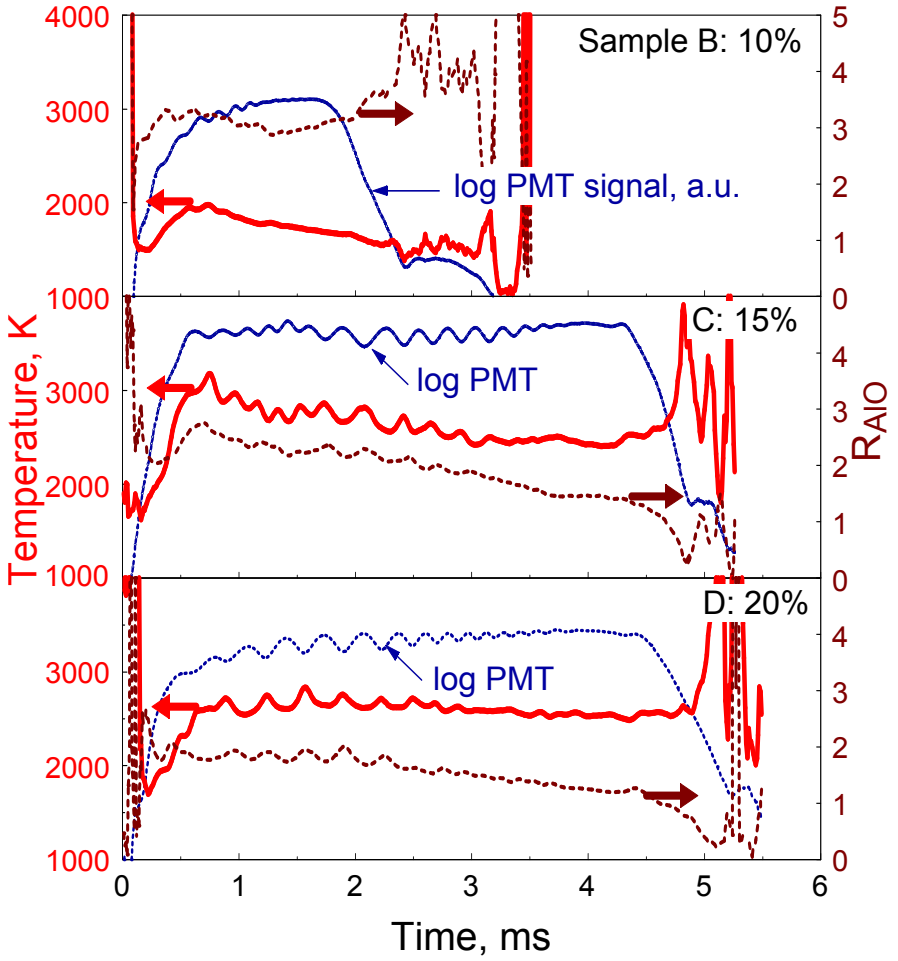


**Figure 4.12** Characteristic traces of emission intensity (logarithmic scale), temperature, and $R_{AlO}$ for ~5 μm particles of samples B, C and D burning in air.

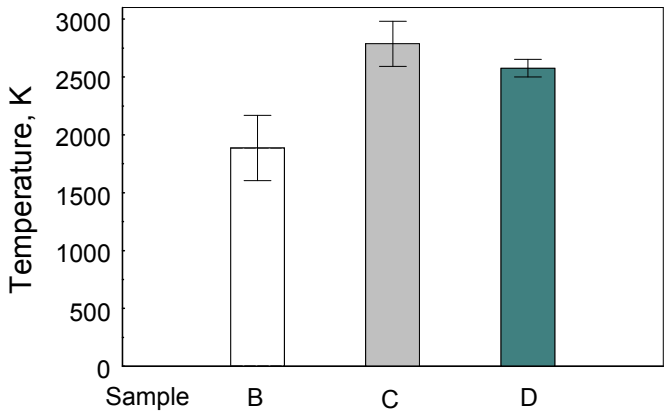


**Figure 4.13** Average burning temperatures and their standard deviations for Al-$I_2$ composites.

## 4.5 Discussion

### 4.5.1 Ignition

Previous analyses of the Al-$I_2$ composite powders with 10 wt. % of iodine prepared by cryomilling showed that iodine is retained in the Al matrix in at least three different forms, corresponding to three stages of iodine release upon heating. The first, low temperature iodine release stage included two steps, roughly correlating with characteristic temperatures of evaporation of $I_2$ and dissociation of $AlI_3$. For samples considered to be stable (high values of *S*, see Table 4.2), the iodine release during this first stage was minimized. At higher temperatures, release of iodine "weakly bound" and "strongly bound" to aluminum (see Chapter 3) occurred. Oxidation of the Al-$I_2$ composite powders was observed to be markedly different from that of the pure Al. The first oxidation step in TGA experiments was observed to occur at a much lower temperature compared to the pure Al. This oxidation step occurred after the initial iodine release. Comparisons of ignition temperature measurements with TGA results for samples A and B described in Chapter 3 indicated that ignition could be best correlated with the release of iodine present in a $AlI_3$-like form in the prepared composite materials, while correlation between ignition and the first oxidation step could not be ruled out. In the present experiments, considering Al-$I_2$ composite powders with a wider range of iodine concentrations, it is observed that the first oxidation step occurs at lower temperatures for materials with greater iodine concentrations. For samples C and

D, this first oxidation step is also much stronger than for samples with lower iodine concentration (cf. Figure 4.6) and, based on Figures 4.8 and 4.9, it is well correlated with ignition events occurring at higher heating rates. It generally appears that the ignition of Al-$I_2$ composite powders depends on both overall iodine concentration and its stability within Al. Less stable samples (see Table 4.2), e.g., samples B (10% $I_2$) and E (30% $I_2$), for which the low-temperature iodine release processes are more significant, ignite at lower temperatures compared to the more stable samples, A(10% $I_2$) and C(15% $I_2$). Sample D(20% $I_2$), which is more stable than sample E(30% $I_2$) and less stable than sample C(15% $I_2$), ignites at the lowest temperature.

Figures 4.8 and 4.9 indicate that the first oxidation step for samples C and D has a noticeably lower activation energy compared to the iodine release steps (lower slopes of the experimental trends in the Kissinger plots shown). Extrapolation of the observed trends to higher heating rates indicates that the first oxidation step may occur at a lower temperature than the second iodine release step, changing the order of events observed in the TGA experiments. Thus, while the present results support previous hypothesis of the importance of early iodine release steps as triggering ignition, they also suggest a more complex relationship between early iodine release and oxidation steps as affecting ignition of the rapidly heated Al-$I_2$ composites.

### 4.5.2 Combustion

Presence of oscillatory emission patterns suggests heterogeneity of the burning particle surface. More specifically, it is suggested that oxide caps are formed early on at the surfaces of the Al-$I_2$ composite particles generating asymmetric flames and associated oscillatory emission patterns. Formation of condensed $Al_2O_3$ inclusions is favored because of somewhat reduced combustion temperatures compared to pure Al. On the other hand, strong periodic oscillations as well as relatively high values of $R_{AlO}$ indicate a substantial vapor phase reaction.

It is interesting that the combustion temperatures correlate with the relative stability of the prepared composite powders, as gauged by parameter *S* shown in Table 4.2. The most stable sample A, for which early release of $I_2$-like and $AlI_3$-like iodine is the smallest, burns at the highest temperature. The next most stable sample C, exhibits the next highest flame temperature, as seen in Figures 4.12 and 4.13. On the other hand, unstable sample B with low iodine concentration burns at a very low temperature.

The above-mentioned, extended duration oscillatory burn patterns and correlation between iodine stability and combustion temperature are somewhat surprising considering that the iodine release might be expected to occur before or at the Al melting point, i.e., at the temperatures much lower than the observed combustion temperatures. If that were the case, combustion of iodine-free particles would proceed in a very similar fashion to that of pure Al. However, differences in the combustion temperatures,

emission traces, and AlO emission observed for the Al-$I_2$ composite particles and pure Al indicate that iodine remains present in the burning particles and affects their combustion. This could be explained by finite kinetics of iodine release and by effects of rapid aluminum oxidation impeding its release.

### 4.5.3 Selection of Useful Al-$I_2$ Compositions

Al-$I_2$ composite materials are being developed as a potential replacement for the Al powder in energetic formulations, which would enable release of biocidal iodine-containing products while maintaining high temperatures and burn rates of aluminized energetic materials. Thus, a practically useful material would burn as well as or better than aluminum and would release the maximum possible amount of iodine-containing products. Constant volume explosion experiments appear to be the most representative of practical combustion conditions and enable the most straightforward selection of an attractive practical composition. Based on the results shown in Figure 4.10, the composition D with 20% $I_2$ appears to be the most attractive. It exhibits an improvement over comparable size pure Al powder in both rate of pressure rise and the total pressure produced in the experiment. Composition D is also attractive based on the ignition experiments presented in Figure 4.7. Furthermore, particles prepared from composition D burn at relatively high combustion temperatures, as shown in Figure 4.13. Finally, this material is relatively stable, as follows from data shown in

Figures 4.5 and 4.6 and Table 4.2, and thus can be readily handled and mixed with other ingredients of the energetic materials.

## 4.6 Conclusions

Increased iodine concentrations in the Al-$I_2$ composite powders prepared by cryomilling shift their first oxidation step to lower temperatures. These materials ignite at much lower temperatures than the pure Al. Both overall iodine concentration and its stability in the Al matrix are observed to affect ignition and combustion characteristics of the Al-$I_2$ composite powders. Qualitatively, lower iodine stability results in a lower ignition temperatures and lower combustion temperatures. Greater iodine concentrations also lower ignition temperatures but do not affect the combustion temperatures substantially. Burn times of individual Al-$I_2$ composite particles are slightly longer and their combustion temperatures are somewhat lower compared to the pure Al. However, improvements in both rate of pressure rise and maximum pressure were observed in constant volume explosion tests with powders containing 15 and 20 wt. % of $I_2$. Preparation of materials with greater iodine concentrations may be feasible but is impractical using the currently available milling equipment.

# CHAPTER 5
# AL-SOLID HYDROCARBON COMPOSITES

## 5.1 Introduction

Aluminum powder is the most commonly used metal fuel additive for propellants, explosives, and pyrotechnics [9]. Its main advantages are a high combustion enthalpy, high flame temperature, and a relatively low cost. However, in many aluminized energetic formulations performance is not optimized because of relatively long ignition delays and difficulties in controlling the rate of combustion. Recent advances in materials manufacturing enable one to design Al-based reactive materials with customized combustion characteristics. Of specific interest are reduced ignition delays and ability to adjust the burn rate, e.g., by producing gaseous reaction products enhancing mixing and combustion efficiency in complex reactive flows. Materials with different burn rates are of interest for different applications; e.g., higher burn rates are desired for pressure generation and impulse, and reduced burn rates (while still complete reaction) are desired for enhanced heat distribution necessary for effective inactivation of aerosolized spores and bacteria. Finally, adjusted flame temperature and emission are often desired for pyrotechnic formulations.

This study is aimed to prepare and characterize novel Al-based alloys and composite materials using mechanical milling: a versatile technique enabling one to

combine aluminum with many different components and achieve unprecedented control over the particle structure and morphology. Often materials that can be made by mechanical milling cannot be prepared otherwise. This project builds on our previous work dealing with Al-based alloys, nanocomposite thermite materials, and Al-$I_2$ composites [3, 60, 73]. In this effort, aluminum is being combined with volatile hydrocarbons producing metastable composite powders. Specifically, paraffin wax and polyethylene are used to create unique composite structures with an aluminum metal matrix. It was initially anticipated that the volatile gaseous fuel may cause fragmentation of the prepared particles during combustion, leading to generation of very finely divided Al, which may enhance combustion dynamics. Such materials were also expected to have reduced ignition temperatures compared to pure Al. It is of interest whether the materials "remember" their metastable nature and structure after their ignition and after melting of their metal matrix. The paper describes preparation and characterization of these materials.

## 5.2 Materials

Reactive composite powders were prepared by ball-milling aluminum and a hydrocarbon additive using a model 01HD attritor mill by Union Process. Aluminum powder, -325 mesh (< 45 μm), 99.5%, was provided by Atlantic Equipment Engineers. The additives were paraffin wax, mp: 70-80 °C, provided by Sigma Aldrich, and polyethylene powder,

low density, 500 μm, provided by Alfa Aesar. 1.8 kg of 10-mm diameter hardened steel balls served as milling media. Liquid nitrogen was flushed through the cooling jacket of the mill and gaseous nitrogen was fed into a 750-ml steel milling vial. In all experiments, the ball-to-powder mass ratio was 36 and the impeller rotation rate was set to 400 rpm. Al-wax and Al-polyethylene (Al-PE) sample were milled for 19 hours each with a nominal hydrocarbon load of 10 wt. %. Milling at room temperature was found to result in strong caking, which prevented further refinement of the material.

The powders were characterized by X-ray diffraction using a Philips X'pert MRD powder diffractometer and scanning electron microscopy (SEM) using a Phenom tabletop microscope by FEI Technologies Inc. The morphologies of Al-wax and Al-PE samples are illustrated in back-scattered SEM images shown in Figure 5.1. Both samples consist of micron-sized, mostly equiaxial particles. Al-wax composite powders are somewhat finer than Al-PE. A close examination of the Al-hydrocarbon particles shows that they are comprised of compacted aluminum flakes; individual flakes or flake-like agglomerates are also observed, the latter are especially abundant in the Al-PE composites. The smallest flake dimension appears to be on the scale of 10-100 nm. It is expected that such flakes adhere to one another with wax or PE coated interfaces; however the aluminum surfaces in such interfaces are formed by shear and deformation of the starting Al particles and are not expected to be coated by protective alumina.

Size distributions of the prepared powders were measured using a Beckman-Coulter LS230 Particle Size Analyzer. Figure 5.2 shows the particle size distribution and respective volume mean particle sizes of both samples. The shape of the size distribution is complex for Al-PE including more flake-like particles, causing possible errors in this light-scattering based measurement designed for spherical powders.

X-ray diffraction patterns showed only peaks of Al and the respective hydrocarbons. Paraffin wax showed peaks at 21-22° and 23.5-24.5° 2Θ, consistent with JCPDS 3-0259. Amorphous or poorly crystalline polyethylene caused a raised background in the range of 18-22° 2Θ, where the strongest peaks for crystalline polyethylene are expected.

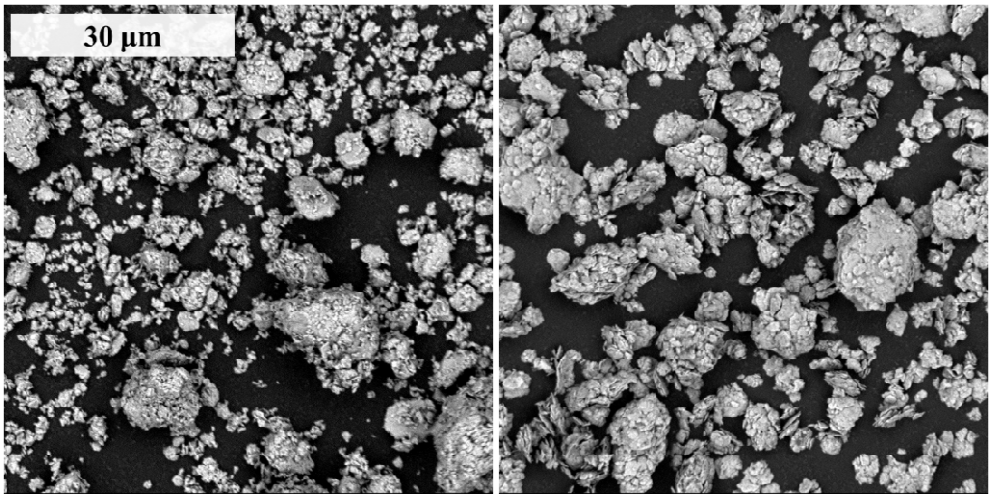


**Figure 5.1** SEM images of Al-wax and Al-PE composites. The scale bar is the same for both pictures.

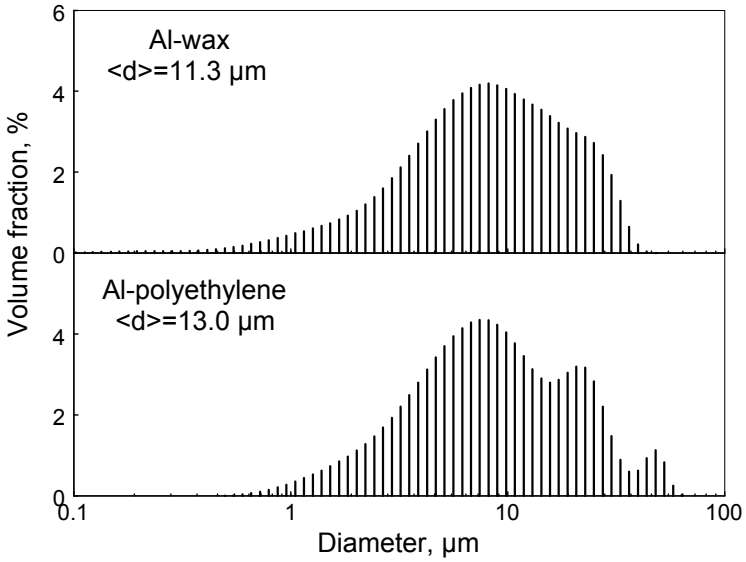


**Figure 5.2** Particle size distributions for Al-wax and Al-PE composites. Volume mean particle sizes are shown for both samples.

## 5.3 Experimental

Release of volatile species upon heating and oxidation of the prepared materials were measured by a TA Instruments model Q5000IR thermogravimetric analyzer (TGA). Alumina pans were used to hold samples for the measurements. The maximum temperature was limited to 1273 K. Experiments addressing release of volatile species in inert environment were performed at the heating rate of 10 K/min in argon. The balance and the furnace were purged with argon at 20 and 50 ml/min, respectively. For oxidation measurements, experiments were performed at heating rates varied from 5 to 100 K/min to investigate the reaction kinetics. The balance and the furnace of Q5000IR were purged with argon at 10 ml/min and oxygen (purity 99.8 %) at 25 ml/min, respectively. The TGA traces were baseline-corrected.

Ignition of the prepared materials was studied at the heating rates ranging from 2000 to 23000 K/s in air using an electrically heated filament [55]. Ignition was observed using both a high-speed video camera. The ignition temperatures were recovered from a high-speed infrared pyrometer for various heating rates.

Burning characteristics of individual composite particles in air were investigated using a laser ignition apparatus, described in detail by [69-71]. In this experiment, some of the particles crossing the $CO_2$ laser beam may not have ignited; some others could have ignited and partially burned while still in the laser beam. In both cases, emission signatures should be discarded from the data analysis, focusing instead on particles ignited in the laser beam and burning after exiting from it. In this chapter, a different data processing step was employed for Al-hydrocarbon samples. Selection of the emission pulses of interest, produced by particles that were ignited, but not partially consumed in the $CO_2$ beam was done considering the amplitude of the emission pulse at the instant the particles left the $CO_2$ beam. When this amplitude was comparable to the maximum emission signal, the particles were discarded. Conversely, emission pulses were analyzed when the signal increased substantially after the particle left the $CO_2$ beam. Specifically, particles were analyzed when the emission signal at the instant the particles left the $CO_2$ beam reached 10 % (Al-wax) or 5 % (Al-PE) of the maximum emission level for the same particle.

Combustion of the prepared composite materials was studied using a constant volume explosion (CVE) experiment. Detailed description of this experiment is available in Chapter 4. Samples were tested in air with a constant powder load of 4.65 g. This mass was selected to be the same as in multiple reference experiments with pure Al powders of different particle [68, 74]. For pure Al and Al-hydrocarbon in air, this mass corresponds to the equivalence ratio of 1.6 and 2.1, respectively, and was observed to be readily and reproducibly ignited in the present CVE apparatus.

The combustion products were embedded in epoxy and cross-sectioned for SEM examination. A LEO 1530 Field Emission Scanning Electron Microscope operated at 10 kV and equipped with energy-dispersive x-ray spectrum (EDX) detector was employed to analyze combustion products.

## 5.4 Results

### 5.4.1 Release of Volatile Species in Inert Environment

The TGA traces for Al-wax and Al-PE composites heated at 10 K/min in Ar are shown in Figures 5.3 and 5.4, respectively. The mass loss traces for the starting hydrocarbons (wax and PE, respectively) are shown for reference. The gasification of pure paraffin wax starts at 430 K, and ends before the temperature reaches 740 K. The decomposition of pure PE starts at a somewhat higher temperature, ca. 580 K and ends by about 750 K. For both composite materials, the mass loss begins at lower temperatures compared to the

starting hydrocarbons. This may be due to distribution of the hydrocarbons in very thin layers with developed surface areas in the composite materials, or to partial breakdown of the hydrocarbons into lighter compounds during the milling process. For wax, the decomposition of the composite and the mass loss of the starting material are rather similar to each other. For PE, the low-temperature mass loss is significantly stronger for the composite material. Furthermore, the second, stronger decomposition step occurs for the composite material noticeably earlier than for pure PE. The differences in decomposition of the initial PE vs. PE contained in the composite material can be due to a modification of PE by milling.

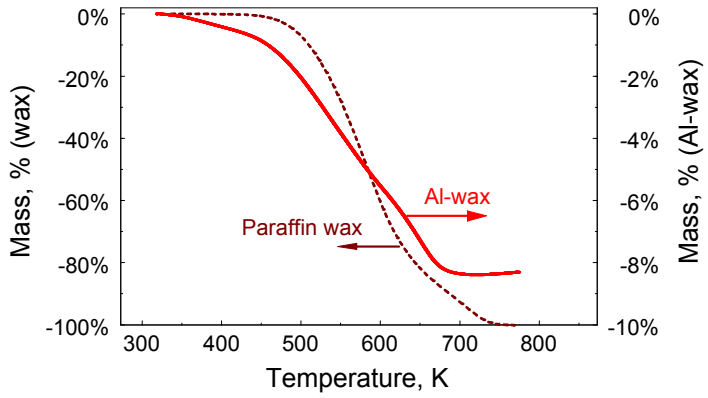


**Figure 5.3** TGA traces of pure paraffin wax and Al-wax composite heated at 10 K/min in argon.

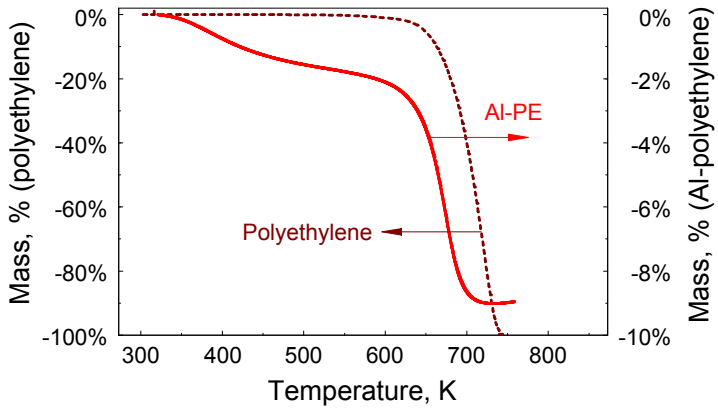


**Figure 5.4** TGA traces of pure PE and Al-PE composite heated at 10 K/min in argon.

### 5.4.2 Oxidation

TGA traces for oxidation of Al-wax and Al-PE composites at a heating rate of 5 K/min are shown in Figure 5.5; the trace for the pure spherical aluminum with volumetric mean particle size of 9.4 μm is shown for reference. The mass changes result from the combined effects of release of volatile additives (mass loss) and oxidation (mass gain). There are two oxidation stages for pure Al in the temperature range from 273 K to 1273 K, which are associated with a phase transformation of amorphous alumina to crystalline $\gamma$-$Al_2O_3$ and with ensuing thermally activated growth of $\gamma$-$Al_2O_3$ [61, 62].

For both, Al-wax and Al-PE composites, the oxidation traces are very similar to each other. A strong weight loss begins at about 450 K, at nearly the same temperature for both materials. The same onset of weight loss observed for both materials in an oxidizing environment is a bit surprising considering that in inert environment, rapid gasification of Al-PE composite occurs at a somewhat higher temperature than that for

Al-wax (cf. Figures 5.3 and 5.4). The weight loss trend reverses at about 560 K, and a strong oxidation stage occurs in the range of temperatures from 750 to 850 K. This oxidation stage is substantially stronger than the first oxidation stage for Al, it also occurs at a lower temperature than for Al. The oxidation rate decreases significantly before Al melts. Well after aluminum melting, at about 1070 K, another oxidation stage occurs, correlating well with the second oxidation stage observed at this same temperature range for pure Al. However, for the composite materials this second oxidation stage is much weaker than it is for the pure Al.

Kinetics of oxidation is studied by tracking the main maxima positions of *dm/dT* while heating Al-wax and Al-PE at different rates from 5 to 100 K/min. The data for two strong oxidation steps occurring at around 823 K and 1070K are further processed and discussed below, in the reaction kinetics section.

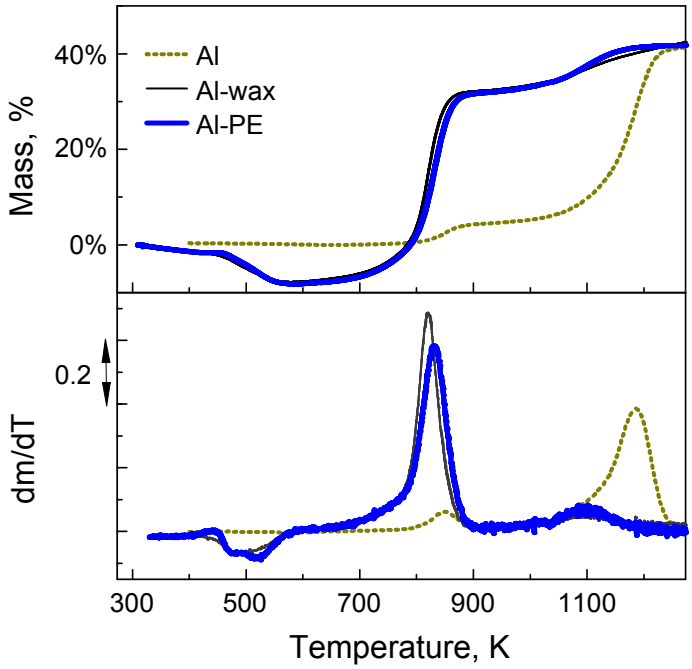


**Figure 5.5** TGA oxidation traces and *dm/dT* derivatives of Al-wax, Al-PE and reference Al (9.6 μm volumetric mean particle diameter) heated at 5 K/min in argon/oxygen flow.

### 5.4.3 Ignition

Figure 5.6 shows ignition temperatures of Al-wax, Al-PE composites and reference Al as a function of the heating rate. Each point represents an individual filament ignition experiment. Ignition instant is identified using recorded videos when the surface (or part of it) of the powder coating becomes brighter than the filament surface. Al-hydrocarbon composites can be easily ignited, and ignition is observed at relatively low heating rates, at which pure aluminum cannot be ignited. Ignition temperatures of Al-hydrocarbon composites fall in the range of 900 – 1200 K, which are much lower than that for pure aluminum. Generally, ignition temperatures increase slightly with

increasing heating rates as is expected for a thermally activated ignition mechanism, although the observed effect is relatively weak.

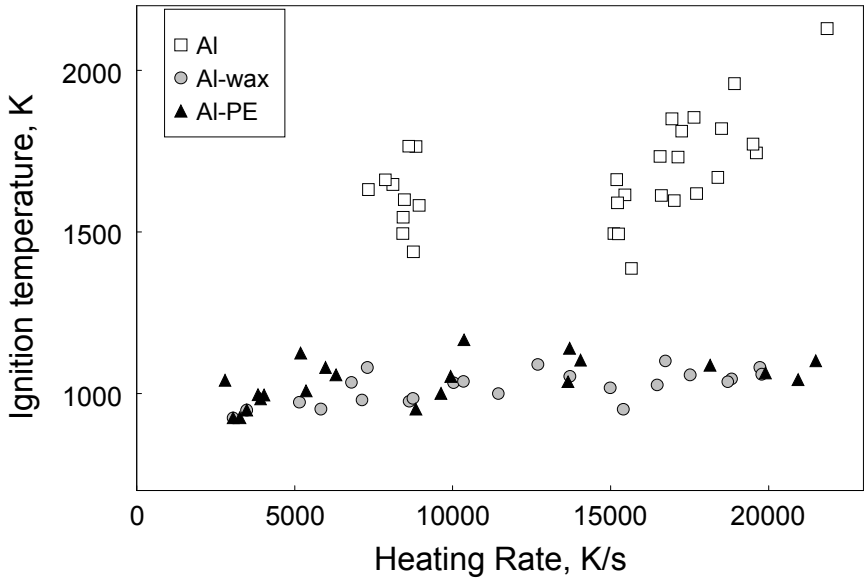


**Figure 5.6** Ignition temperatures for Al-wax, Al-PE and reference Al (9.6 μm volumetric mean particle diameter) measured using an electrically heated filament at different heating rates in air.

### 5.4.4 Reaction Kinetics

TGA results as well as ignition results were processed using the Kissinger method, e.g. [57, 58] , as shown in Figures 5.7 and 5.8. For processing, $\ln(T^2/\beta)$, where $\beta$ is the heating rate, is plotted versus the reciprocal temperature for the following characteristic points identified from the TGA traces: onset of the weight loss upon heating in oxidizing environment and two maxima in the rate of oxidation, determined respectively as the first minimum and two maximum points in the *dm/dT* traces for oxidation experiments (cf.

Figure 5.5). Experimental ignition data from Figure 5.6 are directly transferred into Kissinger coordinates in Figures 5.7 and 5.8, showing the results for Al-wax and Al-PE, respectively. Kinetic trends implied by the oxidation experiments (TGA) can be extrapolated as straight lines (shown as dashed lines) into the range of higher heating rates corresponding to the ignition experiments. It appears that ignition of both composites occurs at somewhat lower temperature compared to that predicted by the extrapolation of the two oxidation stages observed in TGA measurements. The extrapolation of the weight loss step points to temperatures slightly lower than the ignition temperatures. Considering that the direct extrapolation of kinetic trends observed in TGA traces into ignition experiments is only suitable for qualitative assessment of the reaction mechanisms, it is reasonable to suggest that both weight loss and oxidation contribute to processes leading to ignition of the prepared materials. Specifically, it is likely that the weight loss destroys a protective layer formed during milling and including hydrocarbon species. Removal of this protective layer accelerates oxidation and leads to powder ignition.

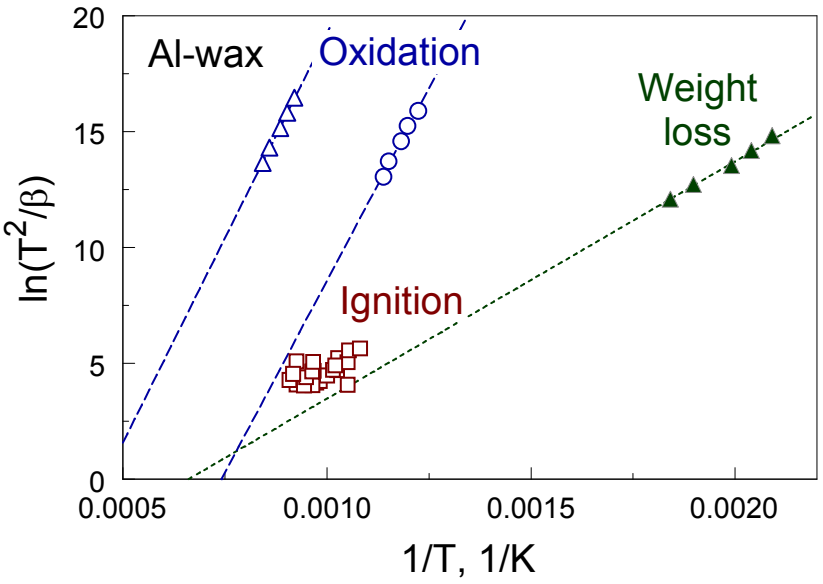


**Figure 5.7** Kissinger plot showing ignition temperatures measured at different heating rates (open squares) together with peak positions for oxidation stages (open triangles and circles) and the onset of weight loss (filled triangles) observed in the TGA traces for Al-wax.

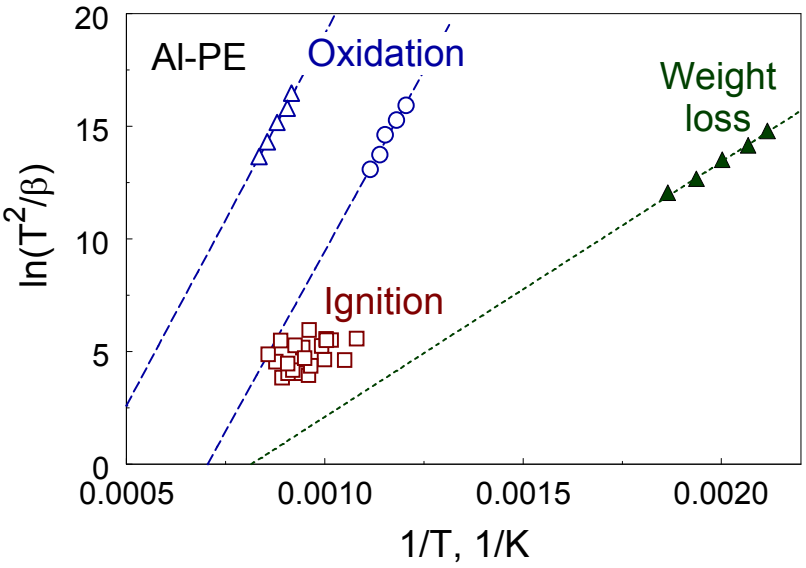


**Figure 5.8** Kissinger plot showing ignition temperatures measured at different heating rates (open squares) together with peak positions for oxidation stages (open triangles and circles) and the onset of weight loss (filled triangles) observed in the TGA traces for Al-PE.

### 5.4.5 Single Particle Combustion

Photographs of laser-ignited and burning particles of Al-wax and Al-PE composites are shown in Figure 5.9; each streak represents a particle after passing through the laser beam. The camera shutter was open for 250 ms so that more than one streak could be captured in each image. In general, streaks of Al-wax and Al-PE are similar to each other. In both pictures, the streaks widen and become brighter soon after particles exit the $CO_2$ laser beam. The broad streaks with blurry boundaries are likely indicators of intensive vapor-phase reactions. The high overall emission intensities last relatively long, and the particles extinguish quickly after the peak emission intensity is achieved. It is also noted that Al-wax produces higher emission intensity than Al-PE.

Figure 5.10 shows characteristic traces for emission, temperature, and $R_{AlO}$ (cf. Equation (4.1)) for both Al-wax and Al-PE. The two composites exhibit similar combustion characteristics. The overall burn time is somewhat longer than that reported for pure Al particles. The oscillatory patterns in the emission signals for both samples are much stronger, and occur over longer periods of time compared to similar signals for pure Al particles. The temperature traces are well correlated with the intensities of AlO emission, which is different from the dynamics observed for pure Al and Al-$I_2$, for which the temperature continued to increase after the peak in the AlO emission in Chapter 4. The combustion temperature and $R_{AlO}$ peak after the initial increase, followed by a gradual decay throughout the rest of combustion. The combustion temperatures remain

stable at around 2400 – 2800 K after pre-heating despite the strong emission oscillations. The values of $R_{AlO}$ are substantially greater than 1 throughout combustion, indicative of substantial vapor-phase reactions.

Figure 5.11 shows the measured emission (burn) time as a function of the particle diameter for Al-wax, Al-PE and pure Al as a reference, taken from [71]. A strong scatter in the data for Al-hydrocarbons is due to errors in measuring particle sizes and the irregularity of the particles. The volumetric average sizes of Al used for this experiment was 15.1 μm. Particle size distributions for composite materials include more fines compared to Al; respectively, more small particles for Al-wax and Al-PE are detected in combustion experiments compared to Al. In general, despite the scatter, Al-based composites appear to burn appreciably longer than similarly sized pure Al particles.

All emission traces were processed to determine the average flame temperature and average $R_{AlO}$ corresponding to the relatively strong emission signal (exceeding 50% of its peak value). Average flame temperature and $R_{AlO}$ for Al-wax, Al-PE and reference Al are shown in Figure 5.12 and Figure 5.13, respectively. The flame temperatures for small-sized particles for Al-wax and Al-PE fall into the similar temperature range as for Al. The trend for larger-sized particles is difficult to see because of a small number of data points available. Larger scatter and lower value of $R_{AlO}$ is observed for both composites compared to Al particles.

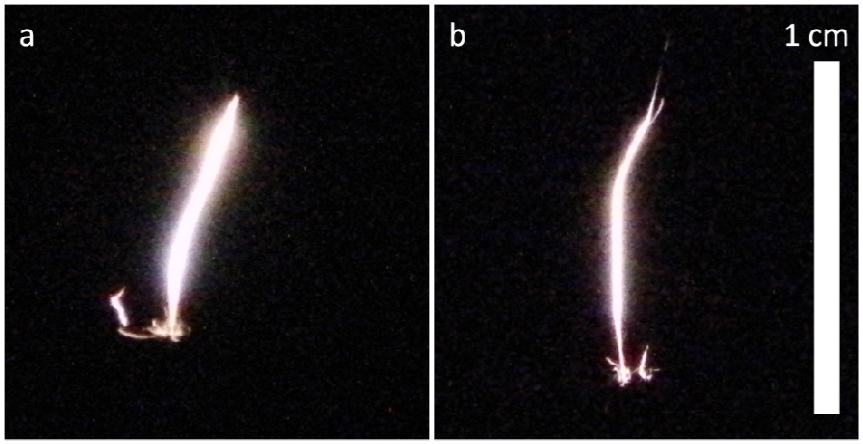


**Figure 5.9** Photographs of burning particle streaks for Al-wax (a) and Al-PE (b). The scale bar is the same for both pictures.

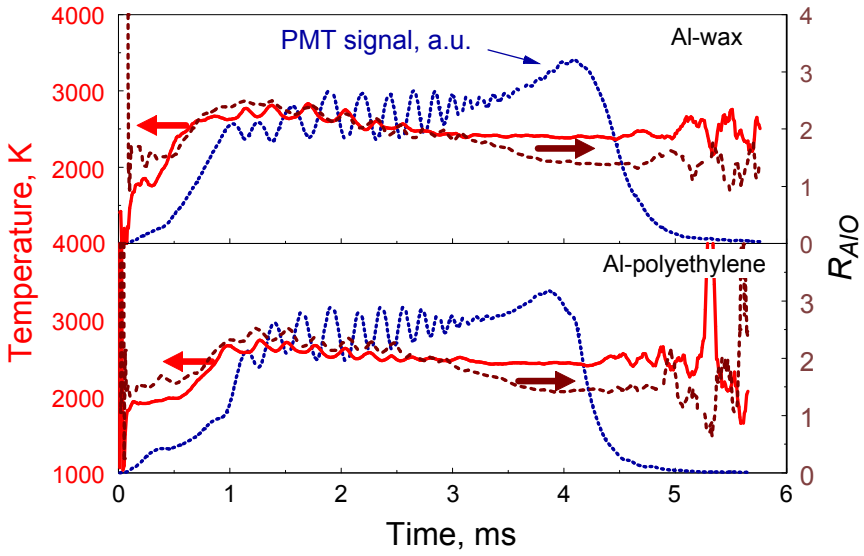


**Figure 5.10** Characteristic traces of emission intensity, temperature, and $R_{AlO}$ for Al-wax and Al-PE in air. The axes for PMT signals plotted in a.u. are not shown.

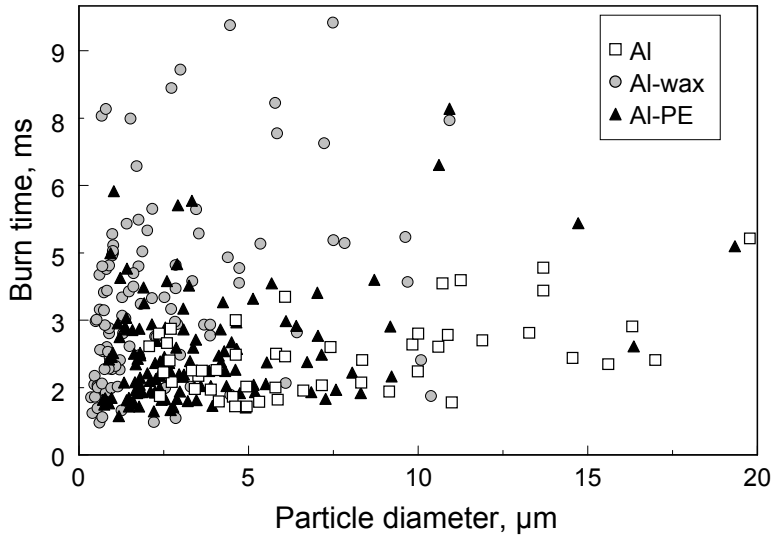


**Figure 5.11** Burn time for Al-wax, Al-PE, and reference Al burning in air.

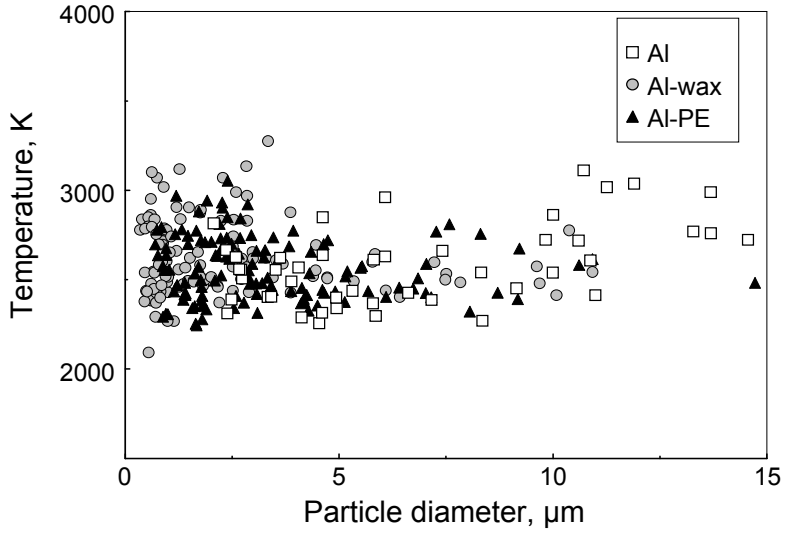


**Figure 5.12** Mean combustion temperatures for Al-wax, Al-PE, and reference Al burning in air.

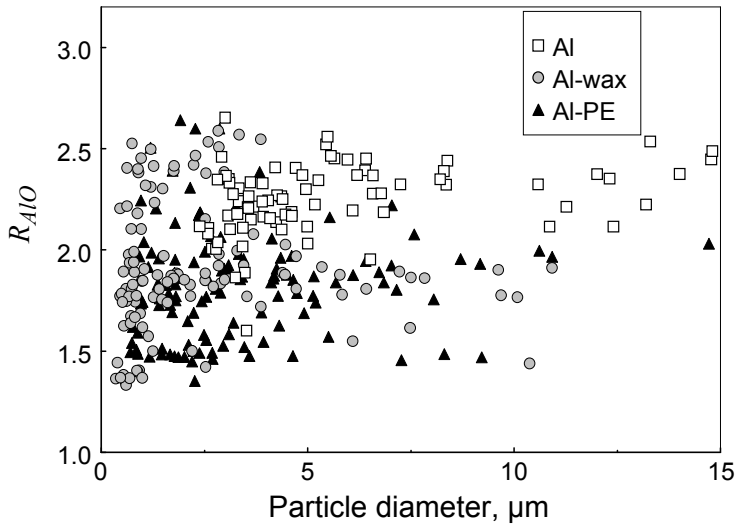


**Figure 5.13** AlO ratios for Al-wax, Al-PE, and reference Al burning in air.

### 5.4.6 Aerosol Combustion

Figure 5.14 shows the pressure traces from CVE experiments for Al-wax, Al-PE composites and reference aluminum. The values of the maximum pressure and the rate of pressure rise from CVE tests are indicative of the flame temperature and combustion rate, respectively. The pressure traces for Al-wax and Al-PE are observed to fit between those shown for Al powders with average sizes 10.9 and 15.1 μm, as is expected considering their average particle sizes. Results for the measured values of maximum pressure and rate of pressure rise, respectively, $P_{max}$ and $dP/dt_{max}$, are summarized in Figure 5.15. The error bars for Al data indicate standard deviations from the mean values obtained from the repeated CVE experiments. Because of relatively low pressures observed, experiments for Al-wax and Al-PE composites were not repeated. For pure aluminum powder, both the maximum pressure and the rate of pressure rise

increase as particle sizes decrease. Al-wax and Al-PE composites produce similar values of $P_{max}$ and $dP/dt_{max}$, indicating comparable combustion temperatures and combustion rates compared to pure Al powder.

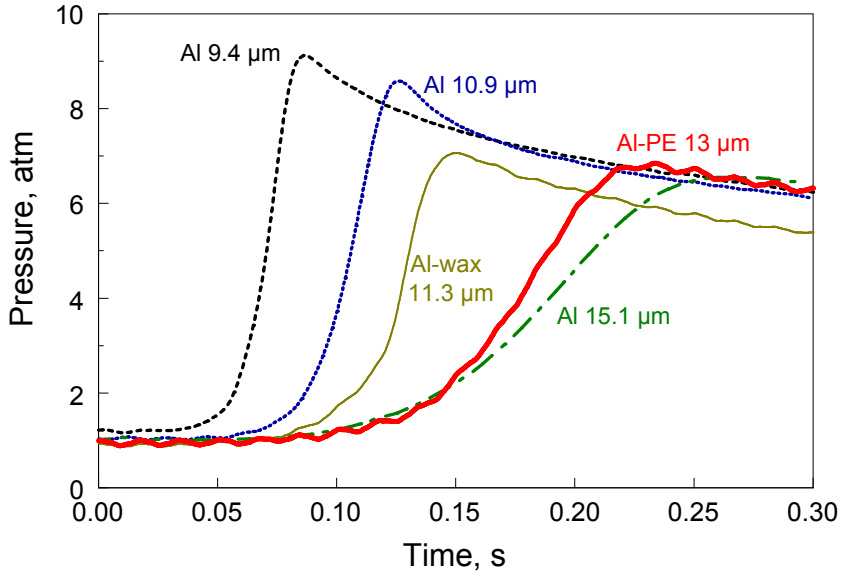


**Figure 5.14** Pressure traces from aerosol combustion experiments for Al-wax, Al-PE and reference Al. Dashed/dotted lines are for Al, solid lines are for composite materials. Labels show volumetric mean particle sizes for spherical Al powders.

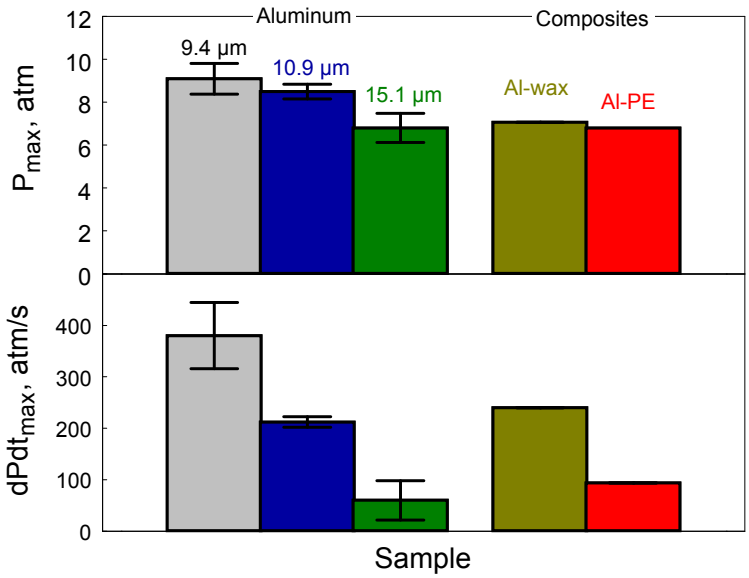


**Figure 5.15** Maximum pressure and maximum rate of pressure rise for Al-wax, Al-PE and reference Al measured in CVE experiments.

### 5.4.7 Combustion Products

Cross-sections of combustion products from CVE experiments were examined by SEM. It is found that combustion products of Al consist of oxide particles, unreacted aluminum with oxide inclusions, and hollow structures, possibly caused by the release of gasified suboxides or boiling of Al. Strong agglomeration is observed in the products of both Al-wax and Al-PE composites, which appeared generally similar to each other. Many of the burned and partially burned particles are much coarser than the starting particles of these Al-hydrocarbon composites. Figure 5.16 shows back-scattered SEM images of combustion products of Al-wax composites. For brevity, additional images including those of combustion products of Al-PE composites were omitted. The image on the left of Figure 5.16 shows an example of a large particle formed as a result of agglomeration.

The particle consists of two main parts: the lighter phase (top, right) is less oxidized than the darker phase (bottom left). The image on the right zooms in the more oxidized portion of this particle. It shows a distinct compositional contrast produced by two phases that were likely separated during solidification. EDX spectra of the light and bright phases marked in the right image in Figure 5.16 are shown in Figure 5.17. Figure 5.17 shows the presence of Al, O, and C, with the C and O balance substantially different in the light and dark phases. The darker phase (right image in Figure 5.16) contains less oxygen and more carbon compared to the lighter phase. The quantitative analysis of the phase composition of the combustion products was difficult because of substantial heterogeneity of the sample, effect of carbon coating applied to prevent charging during SEM analyses, and lack of the appropriate calibration of EDX spectra. However, EDX results for different particles and different materials could be qualitatively compared to one another. Carbon was consistently detected in the products of both Al-wax and Al-PE composites. The carbon concentration varied among different particles. Typically, more carbon was detected in the less oxidized portions of the reacted particles.

Combustion products of Al-wax and Al-PE were also characterized by X-ray diffraction analysis. X-ray diffraction shows only aluminum and alumina phases in the combustion products.

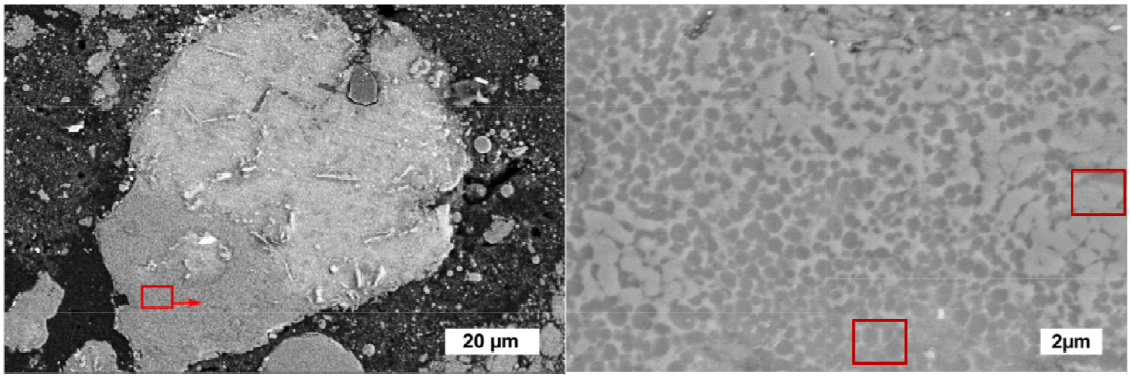


**Figure 5.16** SEM images of cross-sectioned combustion products of Al-wax composites. The image on the right is a magnified view of the rectangular area selected in the left image.

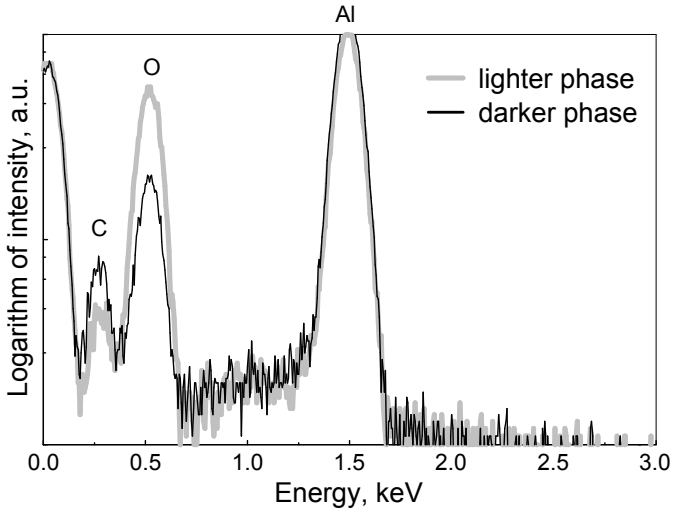


**Figure 5.17** EDX spectra for lighter and darker phases detected in the combustion products of Al-wax composites. The areas for which the EDX spectra were taken are marked in the right image in Figure 5.16.

## 5.5 Discussion

Cryomilling offers a unique approach enabling one to combine aluminum with an unstable or difficult to process additive. Chapters 2-4 showed that iodine is chemically bound and stabilized in the Al-$I_2$ composites prepared by cryomilling. Conversely, no

such stabilization is observed for either wax or polyethylene. Indeed, comparing the weight loss observed upon heating with the initial amount of hydrocarbon added to the powder (cf. Figures 5.3, 5.4), it is concluded that only 10-20 wt. % of the hydrocarbon might be retained in the powder after the hydrocarbon volatilization temperatures are exceeded. This retention can be explained by formation of carbides; however, the bulk of the hydrocarbon additive is readily volatilized. Therefore, for both wax and polyethylene addressed in this work, cryomilling mostly enables their very homogeneous mixing with Al so that very fine Al flakes are covered by thin hydrocarbon layers; such covered flakes are packed to produce micron-sized particles. It appears that hydrocarbons (wax or polyethylene) behave as milling process control agents (lubricants), which do not react with Al, unlike iodine. Thus, the lubricant remains active during the entire milling time resulting in production of finer final particles compared to Al-$I_2$ composites, in which iodine is typically absorbed before the end of the milling run.

The unusual particle morphology for the Al-hydrocarbon composites, in which agglomerated primary particles are flake-like with the smallest dimension on the nanoscale, and for which aluminum surface is coated with hydrocarbon while there is no underlying oxide layer, is likely responsible for their unusual oxidation behavior. Indeed, a strong oxidation step following weight loss caused by volatilization of the hydrocarbon occurs at a significantly lower temperature compared to both pure Al and

Al-$I_2$ composites made by cryomilling [60, 66, 73], both of which are coated by a naturally grown amorphous alumina. The oxidation step is likely occurring at the relatively large exposed metal surface, produced when the hydrocarbon surface coating is volatilized from agglomerated flakes.

Ignition temperatures for all composite materials are substantially lower than for the pure Al. Kissinger processing of ignition and oxidation data suggests that the earliest oxidation processes are likely responsible for ignition of the prepared composite materials. It is also speculated that volatilization and ignition of the hydrocarbon additives may aid ignition of aluminum.

In the single particle combustion experiments, substantial differences were detected in the measured emission intensity, temperature, and AlO emission traces for the prepared composite particles as compared to pure aluminum [71]. These differences are surprising. Indeed, for all materials combustion occurs at very high temperatures compared to the temperatures at which the volatile additives are expected to evaporate and aluminum is expected to melt. Thus, one might have expected that combustion would occur in a similar fashion for the pure Al and materials that are expected to consist of pure Al following the loss of readily volatile components. However, recorded optical signatures of the burning particles suggest that the additives remain in the burning material affecting aluminum combustion well after the particle ignites and melts, similar to what is observed for Al-$I_2$. This conclusion is further supported by SEM/EDX

analyses of the combustion products, in which carbon is found in the partially oxidized particles. It is suggested that the product analysis is directly relevant to the above observations even though the products were collected from CVE rather than single particle combustion experiments. It is proposed that the evaporating hydrocarbon species change the environment around burning particles. In particular, volatile hydrocarbons may be consuming oxygen leaving the particle surface to react with products of their combustion.

Presence of oscillatory emission patterns for single particles of composite materials suggests heterogeneity of the burning particle surface. More specifically, it is suggested that oxide caps are formed early on at the surfaces of the composite particles generating asymmetric flames and associated oscillatory emission patterns. Strong periodic oscillations as well as bright trajectory, high combustion temperature and relatively high values of $R_{AlO}$ indicate non-negligible vapor phase reactions. As stated above, is very likely that for Al-hydrocarbon composites burning in air, evaporated aluminum reacts in an atmosphere with carbon oxides and water, which are not present in similar experiments with pure Al particles. It is suggested that the presence of carbon and hydrogen reaction products in the gas composition in the immediate particle vicinity results in wider and brighter streaks, longer burn time and lower value of $R_{AlO}$. Because combustion temperatures for the composite materials and for pure Al are close to each

other, longer combustion time observed for the composite powders may suggest that such powder particles release more heat and thus burn more completely than pure Al particles.

CVE experiments suggest a similar combustion behavior for Al-hydrocarbon composites as for Al, which is consistent with the combustion temperature measurement from single particle measurements. The reason for the unattractive performance in CVE tests comes from analysis of the collected combustion products for Al-hydrocarbon composites. Specifically, formation of large numbers of very coarse agglomerates in the fuel-rich aerosols may give rise to premature quenching and low reaction completeness, causing relatively low and slowly rising pressures. It is unclear what promotes agglomeration in the aerosolized Al-hydrocarbon combustion products, but it is clear that preventing such agglomeration could substantially improve their combustion performance.

## 5.6 Conclusions

New aluminum-based materials are prepared by cryomilling comprised of an aluminum matrix and hydrocarbon inclusions. Hydrocarbons are not altered chemically; Al-hydrocarbon composites consist of fine Al flakes coated with thin hydrocarbon layers (without intermediate alumina layers), and packed together into micron-sized particles. For both Al-wax and Al-PE prepared materials, their ignition temperatures are reduced substantially compared to pure aluminum. Al-hydrocarbon materials oxidize at

substantially lower temperatures and noticeably faster compared to pure Al powders. Individual particle burn times are longer, the combustion temperatures are similar and values of AlO emission are lower for Al-hydrocarbon particles compared to Al. It is observed that in combustion experiments, hydrocarbon additives do not completely escape before or soon after particle ignition; instead their traces remain in the burning particles changing significantly the resulting burn rate and combustion temperature. For aerosolized powder clouds, burn rates for the Al-wax or Al-PE composite are comparable to that of pure Al. It is speculated that the combustion performance is reduced by the agglomeration observed for the partially burned particles of Al-hydrocarbon composites in the CVE configuration.

# CHAPTER 6

# NEARLY PURE ALUMINUM POWDERS WITH IMPROVED COMBUSTION PERFORMANCE

## 6.1 Introduction

Aluminum powder is an attractive additive for energetic formulations [3, 9] because of its high specific combustion enthalpy, which is greater compared to organic energetic compounds, such as TNT, RDX and HMX. However, utilization of the aluminum combustion energy is limited by its relatively low reaction rates and long ignition delays, which are associated with heterogeneous reactions leading to ignition. Such reactions are rate limited by relatively slow diffusion of reagents through a protective natural alumina layer that is always present on the aluminum surface [27, 62, 75-79]. Different approaches were described in the literature to modify aluminum surface and improve its ignition. Most efforts focused on nanoscale aluminum due to its greater surface to volume ratio and thus most prominent role of the surface reactions in its ignition and combustion mechanisms. It was reported that organic compounds, such as oleic acid [80] and epoxides [17], were used as capping agents on the surface of nano-aluminum. Fluorinated compounds are of specific interest to alter reaction chemistry [16, 81]. Nickel coatings [67, 82-84] were widely studied due to its exothermic reaction with aluminum upon heating. Cryolite [85] was used as an activating agent on the surface of nano-aluminum to influence oxidation. It was also reported that nano-aluminum with

aluminum carbide coating may lead to a decreased amount of the condensed phase in the combustion products [86]. In all previous work, natural alumina layers were replaced by new phases; however, such phases were relatively thick, reducing energy density of the prepared materials.

In this work, a mechanically milled micron-sized aluminum powder with highly developed grain boundaries and surface defects is used instead of nano-aluminum; its surface is protected by a very small amount of a hydrocarbon-based modifier to maintain high energy density of aluminum. Mechanical milling [3, 30] used to prepare this novel Al-based material enables one to achieve unprecedented control over the particle structure and morphology. Al-solid hydrocarbon composites were prepared to replace Al in energetic formulations in Chapter 5. Specifically, paraffin wax and polyethylene were used to create unique metal-hydrocarbon composite structures. However, the addition of a substantial amount of hydrocarbon reduces both the combustion temperature and energy compared to pure Al. The present approach is to only add enough of a hydrocarbon to modify the surface of the prepared powder, while retaining its nearly pure Al composition. When an aluminum powder is ball milled, its original surface coated with alumina is destroyed and a new surface is produced. For milling performed in an inert environment, this new surface is not oxidized. When a hydrocarbon is added as a second soft solid phase, it coats the freshly generated aluminum surface, producing a layer that can protect it from oxidation upon exposure to the atmosphere. During

milling, the hydrocarbon coating is formed at the multiple grain boundaries, while individual grains are pressed together forming final particles. In this work, cyclooctane, a hydrocarbon liquid at room temperature but solid at the liquid nitrogen temperature was used to form a thin protective layer at the surface of the mechanically milled aluminum powder. Excess of cyclooctane is expected to be liquid upon the end of cryomilling and readily removed from the prepared material.

## 6.2 Material Preparation and Characterization

A model 01HD attritor mill by Union Process was used to prepare reactive composites with surface modification. Starting materials were aluminum powder, -325 mesh (< 45 μm), 99.5% pure, by Atlantic Equipment Engineers, and cyclooctane, melting point: 10-13 °C, ≥99% pure, by Sigma-Aldrich. 45 g of Al was mixed with 5 g of cyclooctane and milled for 24 hours in a 750 ml steel milling vial. 10-mm diameter hardened steel balls were used; the ball-to-powder mass ratio was 36 (1.8 kg of milling balls). Cryogenic temperature was achieved by flushing liquid nitrogen through the cooling jacket of the mill. The milling vial was continuously flushed with nitrogen gas. The impeller rotation rate was set to 400 rpm. Solid powders were recovered after milling. Further details describing materials preparation by mechanical milling are given elsewhere [60, 66, 73].

A scanning electron microscope (SEM), a Phenom Tabletop Microscope by FEI Technologies Inc, was used to characterize the prepared powders. Figure 6.1 shows a back-scattered SEM image of a sample. Powders consist of micron-sized, roughly equiaxial particles. Note that the morphology of the prepared materials is different from that of the starting Al powder which comprises smooth, spherical particles.

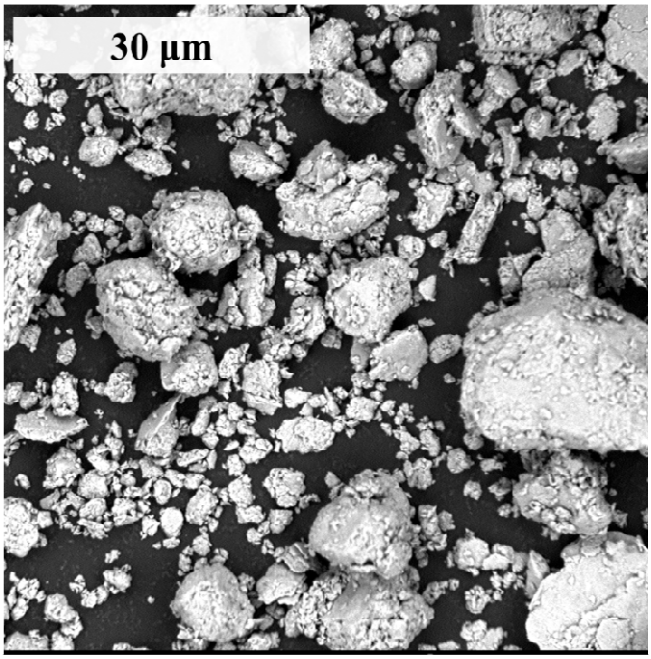


**Figure 6.1** SEM image of the prepared Al-cyclooctane composite powder.

A TA Instruments model Q5000IR thermogravimetric analyzer (TGA) was employed to observe removal of the hydrocarbon retained in the prepared material upon its heating. Alumina pans were used to hold samples for the measurements. 30 mg of as-prepared materials were heated to 773 K at 10 K/min. The balance and furnace were

purged with argon at 20 and 50 ml/min, respectively. Figure 6.2 shows that approximately 2 wt. % of a volatile phase is released from the sample. It appears that the excess of cyclooctane is removed from system by flushing nitrogen gas during or after milling. There are two main mass reduction stages. The first one occurs from 320 to 430 K, which is likely associated with evaporation and boiling of remaining cyclooctane. The second, stronger mass loss occurs at temperatures above the boiling point of cyclooctane (422 K), which indicates that a different, less volatile phase was formed during the milling. No further weight loss was observed when materials were heated above 773K.

Size distributions of the prepared powders were measured using a Beckman-Coulter LS230 Particle Counter. Powders were suspended in deionized water. A surfactant, Micro-90, provided by *Cole-Parmer,* was used as a wetting agent to stabilize particles in the system. Figure 6.3 shows a bimodal size distribution. Volumetric mean particle size is 11.9 μm.

The surface area of the prepared composite particles was measured using a Quantachrome Monosorb BET Surface Area Analyzer. The measurements were performed with both as-prepared powder and with the powder subjected to a controlled heating imitating that achieved in TGA experiments but yielding enough material for the BET analysis. About 1 g of the prepared sample was heated at 5 K/min in air using an Omegalux LMF-3550 furnace. The maximum temperature was 733 K. As discussed

below, no substantial oxidation was observed for the prepared powder in this temperature range. The measured surface areas were 9.4 and 12.8 $m^2/g$ for the as-prepared and heated samples, respectively. For reference, the BET surface area measured for a similarly sized spherical aluminum powder was smaller than 1 $m^2/g$.

X-ray diffraction measurements using a Philips X'pert MRD powder diffractometer showed only peaks of crystalline Al.

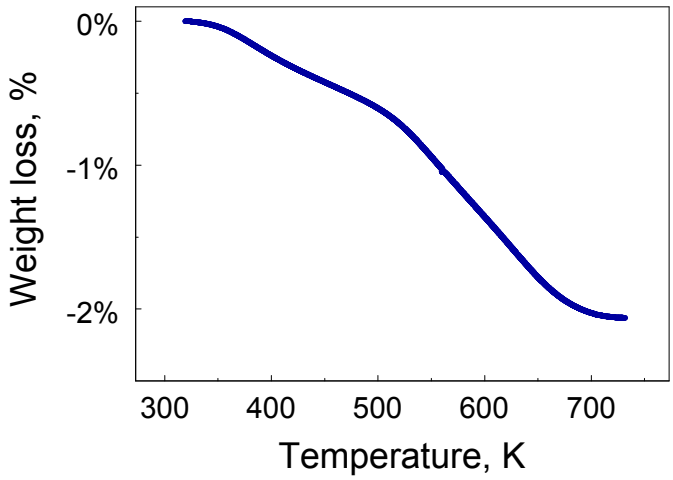


**Figure 6.2** Weight change of the Al-cyclooctane composite powder heated in argon at 10 K/min.

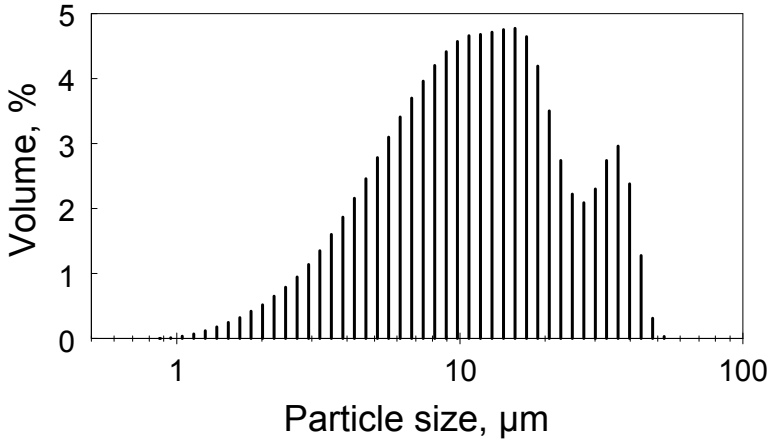


**Figure 6.3** Particle size distribution of the prepared Al-cyclooctane powder.

## 6.3 Experimental

Oxidation was studied by heating powders in the furnace of the Q5000IR TGA analyzer under an oxygen/argon gas flow. Experiments were performed at heating rates varied from 5 to 100 K/min. The maximum temperature was limited to 1273 K. Both the balance and furnace were purged with argon at 10 ml/min and oxygen (purity 99.8 %) at 25 ml/min. The mass of material used in the oxidation experiments varied in the range of 0.4 – 4 mg.

Ignition of the prepared materials in air was studied at a range of heating rates from 3000 to 22000 K/s using an electrically heated filament, as described in Chapter 3 [31]. A small amount of hexane-powder slurry was coated onto a nickel-chromium filament and dried prior to the test. The filament heating rate was controlled by changing the DC voltage and adjustable resistor connected in series with the filament. Ignition was recorded using a high speed camera (MotionPro 500 by Redlake). The

temperature history of the heated filament was measured using a high-speed infrared pyrometer (detector model OS1581 and the monitor model DP1581 by Omega Engineering, Inc.)

Combustion of aerosolized powders was studied using a constant volume explosion (CVE) experiment [68]. A constant powder load (4.65 g) was introduced into the vessel and aerosolized with an air blast delivered from a high-pressure reservoir. Prepared powders and reference aluminum powders with different particle sizes were tested by this technique. Pressure traces recorded by a pressure transducer were analyzed to evaluate the combustion temperature and combustion rate. Experiments with each material were repeated at least three times.

Burning characteristics of individual composite particles in air were investigated using a laser ignition apparatus [69, 71, 87]. Powder particles were fed by an air flow and crossed two laser beams. First, they crossed a beam produced by a 785 nm wavelength, 30-mW laser, and then a second beam of a 125-W $CO_2$ laser. The amplitudes of 785-nm scattered light pulses were measured to determine particle sizes. Four photomultiplier tubes (PMT, Hamamatsu H3164-10), equipped with interference filters (486, 532, 568, and 589 nm), were used to record the light emission from particles ignited by the $CO_2$ laser. Burn times were detected and correlated to the corresponding particle sizes. Color temperature was calculated using emissions at 532 and 589 nm.

The observed AlO emission intensity was evaluated using the ratio of the measured intensity signals calculated by Equation (4.1).

Combustion of individual composite particles in an air-acetylene flame was studied using a modified Bunsen burner [88]. An air-acetylene mixture was fed vertically up through a 5.25-mm diameter nozzle and ignited in room air. The flow rates of air and acetylene were 4719 and 425 mL/min, respectively. The burner included a 2.4-mm diameter stainless steel tube placed coaxially, at the center of the nozzle, and used to inject aerosolized powder particles at the center of the flame. The powder was carried by a nitrogen flow at 944 mL/min. The aerosolized particles were supplied using a custom-designed screw feeder. The feed rate was adjusted to be sufficiently low, so that most of the individual particle emission pulses could be resolved.

Infrared emission of particle combustion were measured by three PMT's (two R3896-03 and one R636-10 by Hamamatsu) equipped with interference filters (700, 800 and 900 nm). Emission pulse durations were determined as burn times for individual particles. The statistical distribution of the measured burn times was correlated with the powder particle size distribution to obtain the particle burn times as a function of their diameters. Two color temperatures were calculated using emission ratios at 900/700 nm and 800/700 nm.

## 6.4 Results

### 6.4.1 Oxidation

Figure 6.4 shows the oxidation weight gains and mass derivative for the prepared composite powder and, for comparison, for a pure aluminum powder with a volumetric mean particle size of 7.2 μm. In the measured temperature range from 273 K to 1273 K, two main oxidation stages are observed for both materials. The two stages in oxidation of Al are known to be respectively associated with a phase transformation of amorphous alumina to its crystalline $\gamma$-$Al_2O_3$ polymorph, and with ensuing thermally activated oxidation of $\gamma$-$Al_2O_3$ [61]. Al-cyclooctane composite starts gaining weight from a temperature between 600 and 700 K, which is much lower than the temperature for the detected oxidation onset for the pure aluminum powder with the comparable (even finer) average particle size. Surprisingly, the weight gain for the first oxidation stage is approximately 49% of the initial weight, which is substantially greater than that for pure Al. A strong peak, corresponding to the first oxidation stage, is also observed on dm/dT trace, indicating a greater oxidation rate compared to Al. The oxidation rate decreases significantly before Al melts. Well after aluminum melting, at about 1000 K, another oxidation stage occurs with a lower, almost constant rate, correlating with the second oxidation stage observed at this same temperature range for pure Al. The second oxidation stage for composites is much weaker compared to Al.

Oxidation results at varied heating rates from 5 to 100 K/min were used to determine oxidation kinetics for prepared powder. Results are described in the oxidation kinetics section.

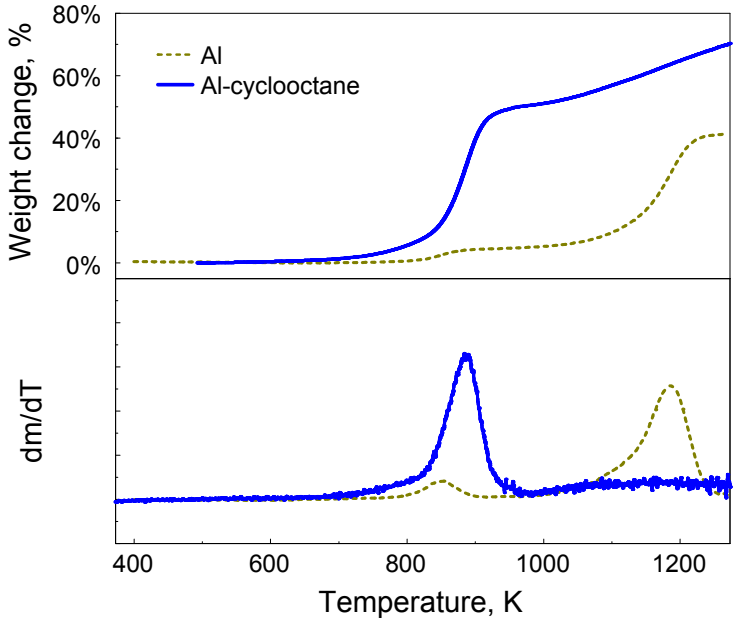


**Figure 6.4** Oxidation weight gains (TGA results) and mass derivative for the prepared Al-cyclooctane composite powder and reference pure Al powder (volumetric mean particle size 7.2 µm) heated at 5 K/min.

### 6.4.2 Ignition

Both the Al-cyclooctane composite powder and reference pure aluminum powder (volumetric mean particle size 7.2 µm) were tested. Ignition temperatures as a function of the heating rate are shown in Figure 6.5; each point represents an individual filament ignition experiment. Ignition moment is defined when a first bright spot is detected on the powder coating in the video recorded at 500 fps. The prepared composite powder

ignited readily with a strong light emission, and at fairly reproducible ignition temperatures at heating rates ranging from 3000 to 23000 K/s. Reference aluminum could not be ignited at heating rates lower than 7000 K/s. Ignition temperatures for the composite powder fall into the range of 950 - 1200 K, which are significantly lower than that for pure aluminum. A trend is clearly noticed that the ignition temperatures increase with increasing heating rates as is expected for a thermally activated ignition mechanism.

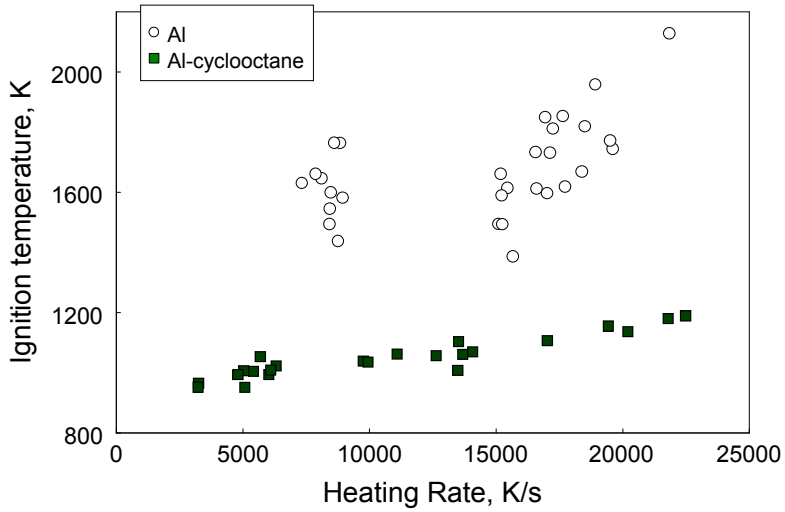


**Figure 6.5** Ignition temperatures for the prepared Al-cyclooctane composite powder and for reference pure Al powder (volumetric mean particle size 7.2 μm) measured using an electrically heated filament at different heating rates in air.

### 6.4.3 Oxidation Kinetics

Ignition results are correlated with oxidation steps observed in TGA by Kissinger method [89]. For TGA data, the onset temperatures of the two distinct oxidation steps are recovered for the heating rates, $\beta$, of 5, 10, 20, 50 and 100 K/min. A plot of $\ln(T^2/\beta)$

versus the reciprocal temperature *1/T* for two oxidation stages is shown in Figure 6.6. Results of ignition temperature measurements at higher heating rates are presented in the same coordinates. Straight lines linearly fitting each group of oxidation data points are extrapolated into the range of high heating rates corresponding to the ignition measurements. Figure 6.6 shows that when heating rates typical of ignition experiments are approached, the second oxidation stage is expected to occur at much higher temperatures, and the first oxidation stage is extrapolated to slightly higher temperatures, as compared to the observed ignition temperatures. The activation energy of the first oxidation step is also greater than that implied by a very small slope of the ignition data points. It is likely, therefore, that the release of volatile hydrocarbon occurring at temperatures lower than the first oxidation step (see Figure 6.2) and not very well resolved in the oxidation traces (cf. Figure 6.4) can be correlated with the observed ignition behavior.

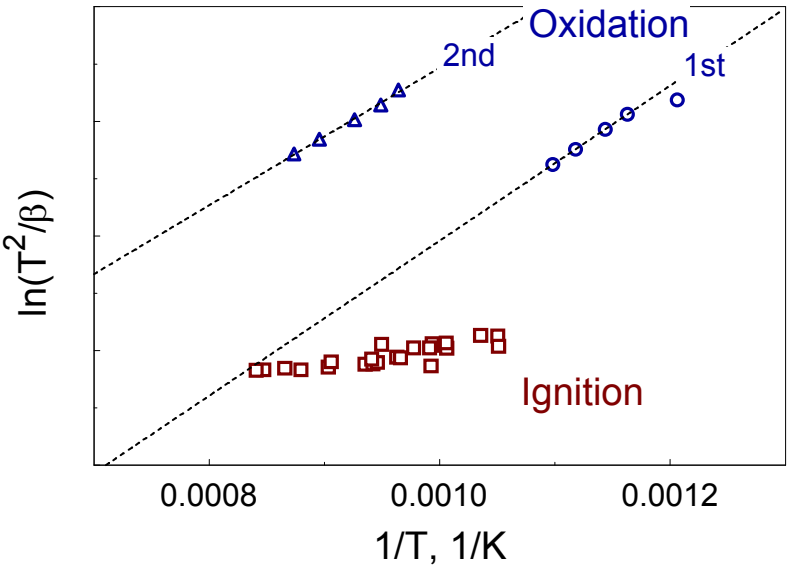


**Figure 6.6** Kissinger plot showing ignition temperatures measured at different heating rates (squares) together with peak positions for oxidation stages (triangles and circles) observed in the TGA traces for Al-cyclooctane.

### 6.4.4 Aerosol Combustion

Three CVE aerosol combustion experiments were performed for Al-cyclooctane and three aluminum powders with different particle sizes. Pressure traces were normalized over initial pressure prior to ignition. A representative result is shown for each aluminum powder, while three traces are presented for Al-cyclooctane in Figure 6.7. For this experiment, the ratio of the maximum explosion pressure, $P_{max}$, over the initial pressure, $P_0$, is roughly proportional to the combustion temperature, while the maximum rate of pressure rise, $dP/dt_{max}$, is an indicator of the combustion rate. A NASA CEA code [90] was used to interpret the CVE experiment and calculate adiabatic pressures corresponding to the experimental conditions, which were 12.58 and 12.56 atm for Al

and Al-cyclooctane, respectively. Combustion efficiencies were calculated by comparing the experimental and calculated pressures. Average values for $P_{max}/P_0$, $dP/dt_{max}$ and combustion efficiency are summarized in Table 6.1.

For the pure aluminum particles, when particle size decreases both the maximum pressure and rate of pressure rise increase, while the time delay of ignition is reduced. Based on its mean particle size, the combustion performance for Al-cyclooctane was expected to fit between those shown for Al powders with average sizes 10.9 and 15.1 μm. However, Al-cyclooctane powder is readily ignited, and produces higher maximum pressure and rate of pressure rise compared to similarly sized pure Al powders, which indicates a higher flame temperature and combustion rate compared to aluminum. The combustion efficiency is also appreciably improved and is close to that of the finest aluminum powder.

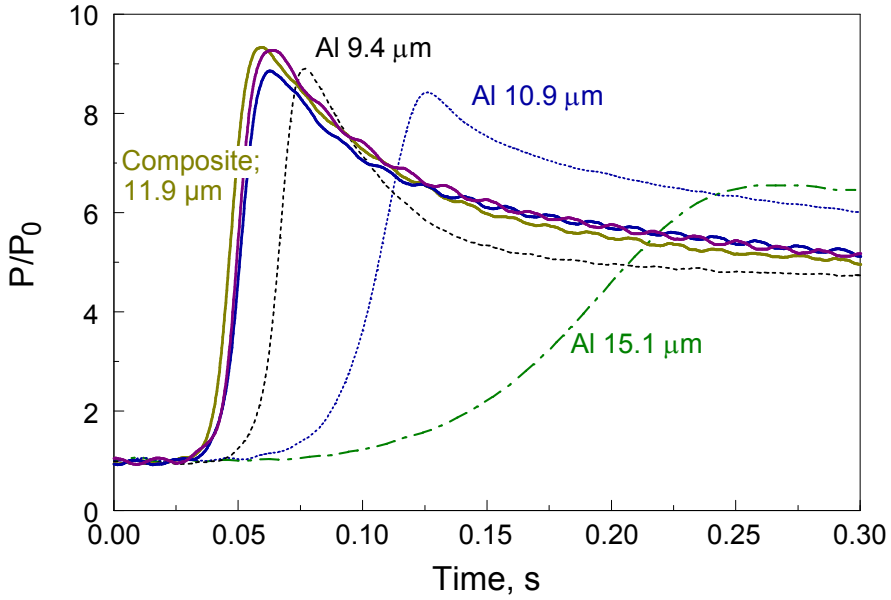


**Figure 6.7** Pressure traces for Al-cyclooctane compared with similar-sized Al powders in CVE experiments.

**Table 6.1** Statistical Results for Samples and References in CVE Experiments

| | Al | | | Al-cyclooctane |
|---|---|---|---|---|
| Mean size, μm | 9.4 | 10.9 | 15.1 | 11.9 |
| $P_{max}/P_0$ | 9.1 | 8.5 | 6.8 | 9.1 |
| $dP/dt_{max}$, atm/s | 380 | 212 | 60 | 537 |
| Efficiency, % | 72.3 | 67.6 | 54.1 | 72.8 |

### 6.4.5 Seeded Flame Combustion

Figure 6.8 shows a characteristic trace of emission intensity and color temperature from the emission intensity ratio for 900 and 700 nm for an Al-cyclooctane particle burning in the combustion products of a laminar air-acetylene flame. Combustion temperatures calculated using the emission intensity ratio for 800 and 700 nm were found to be similar to those obtained using the emission signals at 900 and 700 nm. A fraction of the

temperature trace, corresponding to the emission signal exceeding half of its maximum value is plotted as a thicker line. The color temperatures obtained using this stronger portion of the signal are more reliable and were used to calculate the average temperature for each particle. In general, strong oscillatory pattern in the emission signals is observed during combustion. Despite the oscillation of emission intensity, temperature is relatively stable. Unlike combustion in air, for which emission intensity peaks quickly, emission intensity of particles in the hydrocarbon flame achieves its maximum value in the middle of combustion.

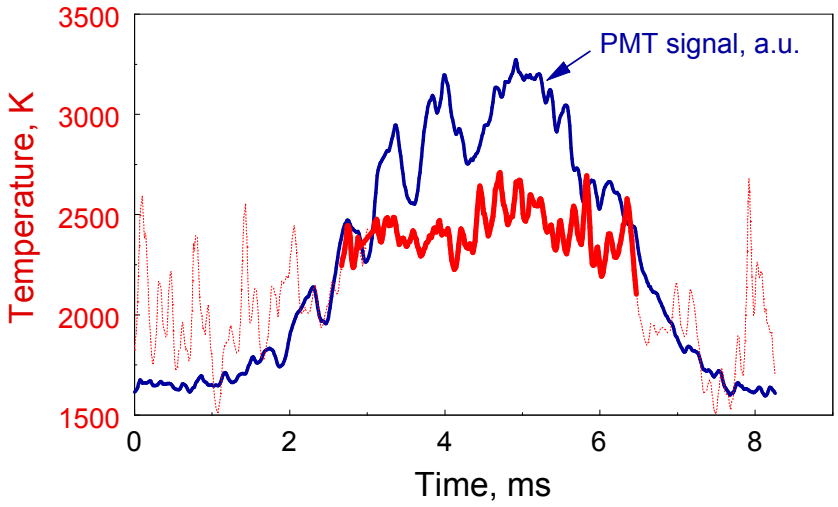


**Figure 6.8** Characteristic traces of emission intensity and temperature for Al-cyclooctane particle burning in an air-acetylene flame. The axis for the PMT signal plotted in a.u. is not shown.

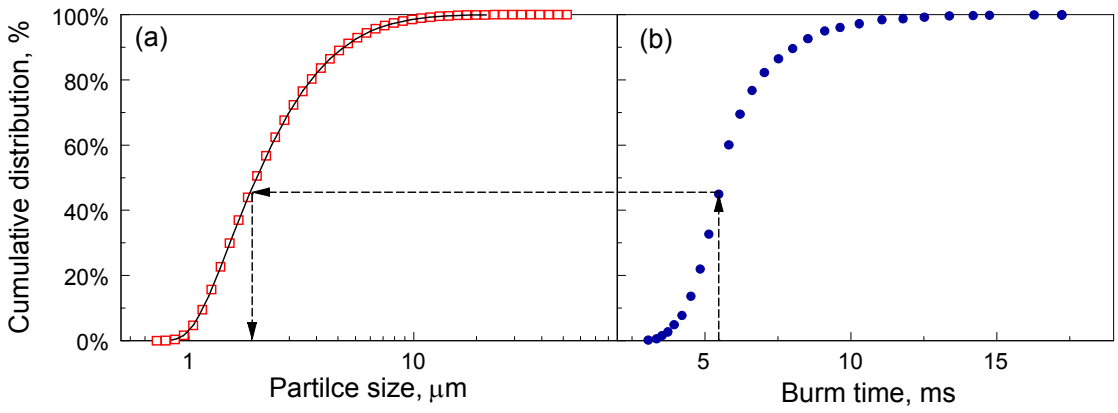


**Figure 6.9** Cumulative distributions illustrating correlation of particle sizes and burn times. (a) Cumulative percentage of particle number vs. particle diameter; (b) Cumulative percentage of particle number vs. burn time.

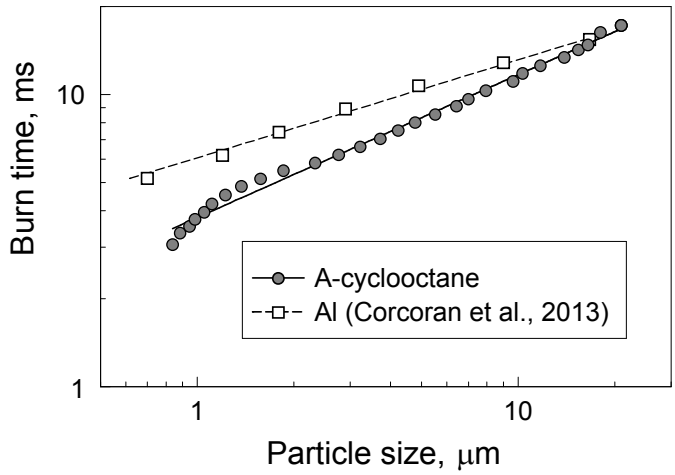


**Figure 6.10** Burn times in flame versus particle size.

The distribution of the measured burn times was correlated with the particle size distribution as shown in Figure 6.9. The burn times for about 2000 particles were quantified from emission traces, and broken in 30 bins. Cumulative particle number distribution as a function of time bin is shown in Figure 6.9 (b). The volume-based

differential particle size distributions shown in Figure 6.3 were transferred into number-based integral distributions as shown by the open squares in Figure 6.9 (a). To recover particle sizes corresponding to burn times, cumulative particle number density was initially obtained for each time bin. For the obtained cumulative particle densities, respective particle sizes were determined using interpolation between individual points represented by the solid line in Figure 6.9 (a).

The resulting burn times versus particle size are shown in Figure 6.10. An equation of $t=a\cdot D^b$, where $t$ is burn time, and $D$ is particle size, was used to fit the results, as shown by the trend-line in Figure 6.10. The exponent value is found to be $b$=0.5, which is roughly consistent with empirical exponents reported for pure aluminum burning in the $N_2/O_2$ gas mixtures [71]. The multiplier $a$=3.79 for the burn times expressed in ms and particle diameter in μm. For comparison, data and a trend line from [88] are also shown for pure Al powder burning in the same, laminar air-acetylene flame. The burn times for both materials are close to each other. For pure Al, the burn times are slightly longer and the effect of particle size on the burn time for pure Al is a bit weaker.

Combustion temperatures measured in this experiment were found to be independent of burn times (and particle sizes, respectively). The mean combustion temperature at 900/700 nm of Al-cyclooctane particles burning in the combustion

products of a hydrocarbon flame was 2414±61 K. The mean combustion temperature at 800/700 nm was 2371±67 K.

### 6.4.6 Single Particle Combustion

Figure 6.11 shows a photograph of Al-cyclooctane particles ignited by a $CO_2$ laser and burning in air. Particles are injected vertically up from the bottom of the image. Each streak represents a particle that crossed the laser beam and ignited. The camera shutter was open for 250 ms while individual particle burn times are only a few ms each, so several subsequently occurring streaks were captured in the image. In the picture, the streaks become brighter, and reach the strongest light emission level soon after particles exit the $CO_2$ laser beam. After the peak intensity, prominent luminous oscillations begin and last until a second peak of the emission intensity is reached. It is also noted that characteristic spear points are formed before particles completely extinguish.

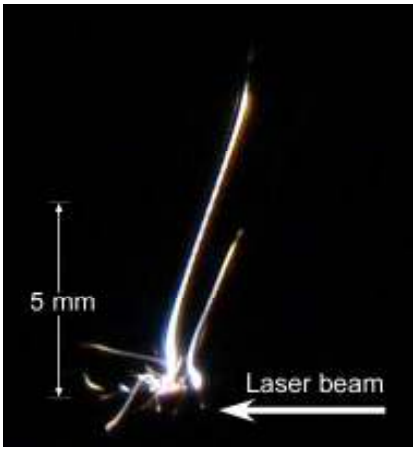


**Figure 6.11** Emission streaks produced by Al-cyclooctane particles ignited by a $CO_2$ laser and burning in air.

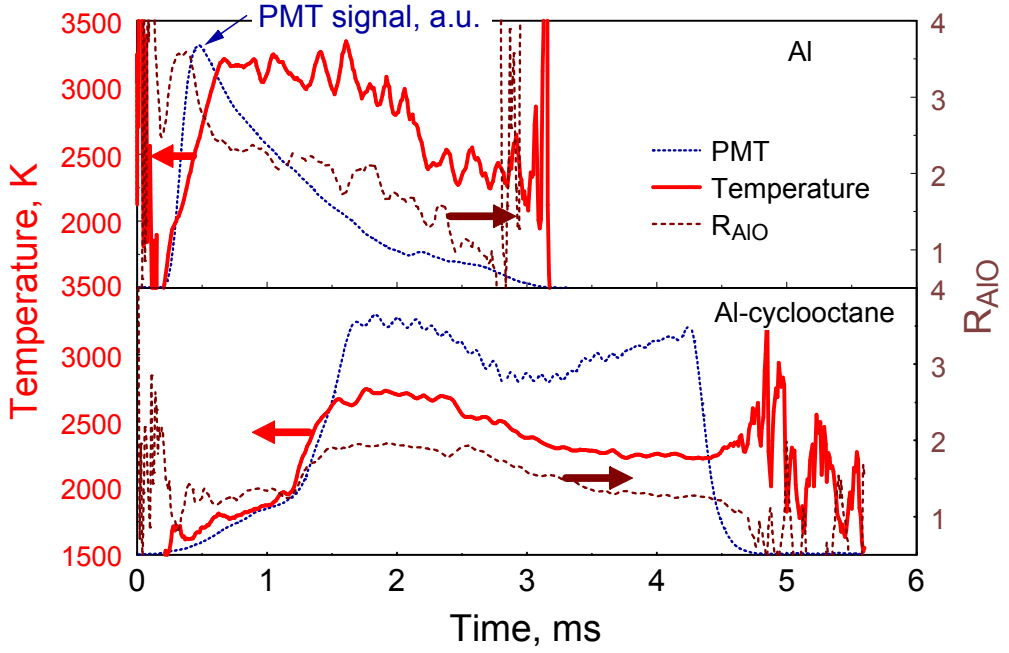


**Figure 6.12** Characteristic traces of emission intensity, temperature, and $R_{AlO}$ for Al and Al-cyclooctane particles burning in air. The axes for PMT signals plotted in a.u. are not shown.

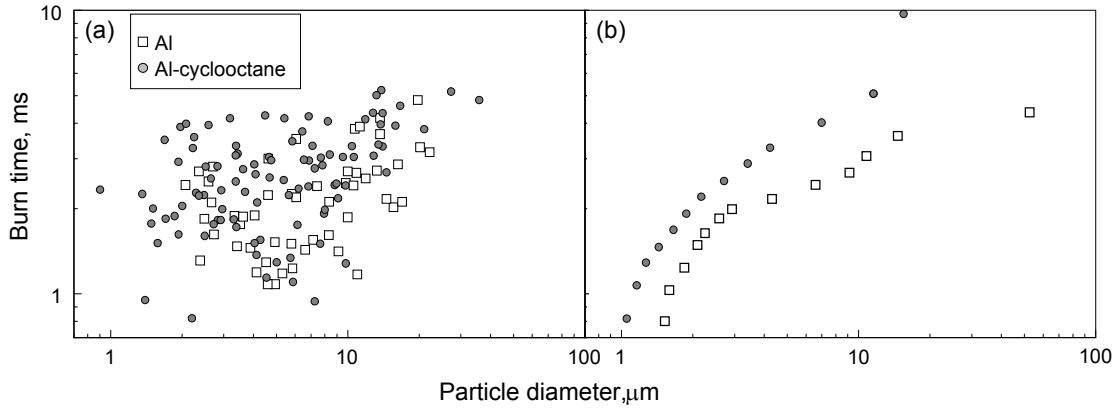


**Figure 6.13** Burn times for Al-cyclooctane and reference Al particles in air.

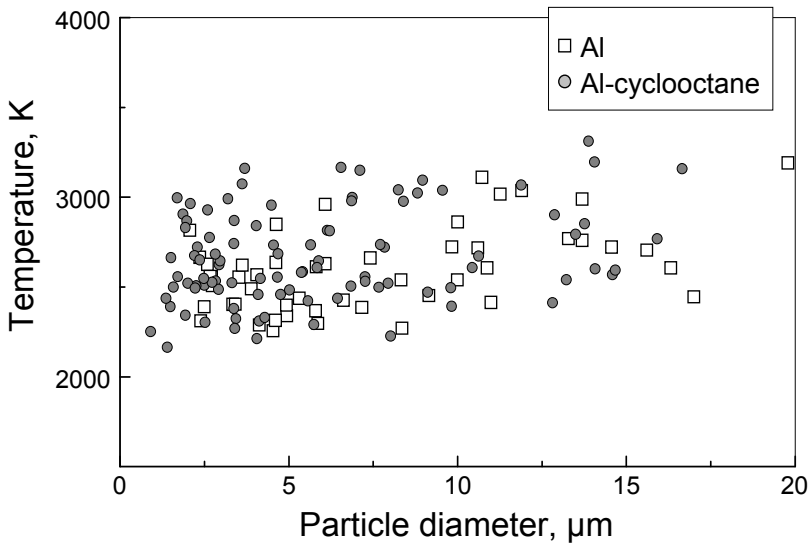


**Figure 6.14** Combustion temperature for Al-cyclooctane, and reference Al particles burning in air.

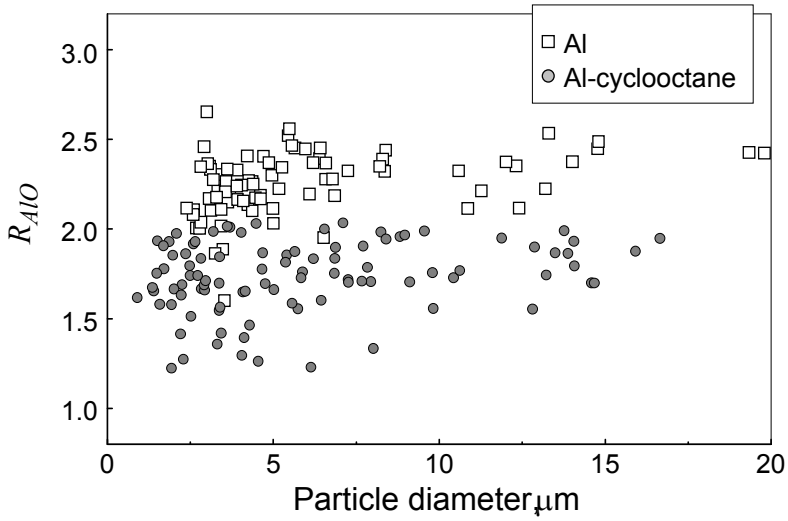


**Figure 6.15** Ratio $R_{AlO}$ (see Equation 4.1) for Al-cyclooctane and reference Al particles burning in air.

Characteristic traces for emission intensity, temperature, and $R_{AlO}$ (cf. Equation (4.1)) for burning Al-cyclooctane and pure Al particles are shown in Figure 6.12. Generally, Al-cyclooctane particles burn longer, show stronger oscillatory patterns in

their emission signals, and their combustion temperatures and $R_{AlO}$ values are lower compared to pure Al. While not as strong as for pure Al, vapor phase reactions are significant for the composite powder, as demonstrated by the value of $R_{AlO}$ >1. Unlike aluminum particles, for which the temperature continues to increase after the peak value of the AlO emission is observed, the temperature for Al-cyclooctane increases simultaneously with AlO emission and black-body optical emission. Both temperature and AlO emission are decreasing during combustion, indicating an increasing role of surface reactions compared to the vapor-phase combustion.

For each particle, its size is correlated with the measured emission time using data processing described in detail elsewhere [71]. The emission time as a function of particle size is plotted in Figure 6.13(a). A substantial scatter in the data for composites is likely due to errors in measuring particle sizes caused by the irregular particle shapes. The $t \sim D^b$ fits for each material are also shown, where $b \approx 0.3$ for both cases. Al-cyclooctane composites appear to burn appreciably longer than similarly sized pure Al particles; the observed effect of particle size on the burn time for each material is very weak.

The measured burn times were also processed neglecting the particle size measurements and simply correlating the statistical distribution of the burn times with particle size distribution, as described above and illustrated in Figure 6.9. The burn times for about 330 and 120 particles were used for Al-cyclooctane and Al, respectively;

12 burn time bins were used. Particle sizes were determined for these burn time bins by matching cumulative distribution between particle size and burn time; results are plotted in Figure 6.13(b). In general, the trends in Figure 6.13 (a) and (b) are similar to each other; however, the effect of particle size on the burn time appears to be stronger, especially for finer particles, in Figure 6.13 (b). An equation of $t=a\cdot D^b$, was used to fit the data (neglecting the least reliable first and last points corresponding to the finest and coarsest size bins). The exponent values are found to be $b$=0.63 and 0.47 for Al-cyclooctane and Al, respectively.

Average flame temperature and average $R_{AlO}$ values were determined using the fractions of the emission signals exceeding 50% of their respective peak values. Figures 6.14 and 6.15 show average flame temperature and $R_{AlO}$, respectively, for both Al-cyclooctane and Al. The flame temperatures for Al-cyclooctane fall into a similar temperature range as for Al, while $R_{AlO}$ is substantially lower indicating a weaker molecular AlO emission compared to Al. Both the flame temperature and $R_{AlO}$ are nearly independent of particle size for both materials. The mean flame temperature for Al-cylcooctane is close to 2680 K, similar to that of the pure Al.

## 6.5 Discussion

The prepared powder, similar to the recently prepared composite powders of Al-wax and Al-polyethylene [91], consists of tightly packed small flakes of aluminum [34, 60]. The prepared composites possess large active surface despite its relatively large mean volume-based particle size of 11.9 μm. The flake surface is likely to be coated with a layer reacted with cyclooctane, replacing natural alumina present for pure Al powders. This layer likely forms during the cryo-milling, when cyclooctane exists as a soft solid interacting with harder but still ductile aluminum particles flattened into flakes by the milling balls. Most of cyclooctane retained in the prepared ball-milled powder is removed upon heating. The weight loss (cf. Figure 6.2) occurring above the boiling point of cyclooctane is indicative of the formation of a surface-stabilized Al-cyclooctane compound. These new phases could not be detected from XRD, suggesting that they either are poorly crystalline, or exist in very thin layers. It is interesting that the loss of this compound upon heating occurs immediately prior to the first oxidation step in the prepared materials. The amplitude of the first oxidation step is rather large, indicating a large surface involved in the reaction. This can be understood assuming that when the protective cyclooctane layer is removed from the surface of aluminum flakes, including the surfaces between consolidated flakes, oxidation can occur at a much larger surface area than the external surface of consolidated particles visible in Figure 6.1. This hypothesis was supported by a BET-measured increase in the surface area of the heated

composite particles. The combined effects of removal of the protective surface layer followed by a strong first oxidation step are suggested to be responsible for the low-temperature ignition of the prepared materials. The lack of direct correlation between kinetic trends for the first oxidation step and ignition in Figure 6.6 is probably explained by an inter-dependency between the processes of cyclooctane release and oxidation, which both alter the surface properties of the prepared powders.

The results of single particle combustion experiments are generally consistent with recent experiments with powder particles in the same size range [70-73, 87, 92]. The effect of particle size on the burn time is relatively weak and the particle combustion temperatures are the same as those for pure Al. However, the results of experiments using air-acetylene flame are in an apparent conflict with the experiments using particles ignited by $CO_2$ laser and burning in air. The burn times in Figure 6.10 are longer than those shown in Figure 6.13 for both Al and Al-cyclooctane powders. This observation can be interpreted considering that the oxidizing environment was substantially different in the two combustion experiments described. Calculation from CEA code shows that $CO_2$ and water are the main combustion products for air-acetylene flame under experimental conditions. Further, the effect of oxidizer may also need to be considered to explain why pure Al particles burn faster than the prepared composite particles in air (Figure 6.13) but somewhat slower in the air-acetylene flame (Figure 6.10). It is possible that the released cyclooctane generates a boundary layer surrounding a burning

particle and including products of cyclooctane decomposition, which are expected to be similar to the combustion products forming in the air-acetylene flame. The presence of such a layer in air would reduce accessibility of the particle surface to oxygen. However, in air-acetylene flame this layer may not be affecting the transport of oxidizing species to the particle surface. Therefore, effects of particle surface morphology on its burn rate may dominate, and the surface increased due to the release of cyclooctane may accelerate not only ignition but also combustion of the prepared powders, compared to spherical aluminum.

It is also interesting to note that despite a somewhat longer burn times observed for the composite particles in air, in CVE experiments both maximum pressure and rate of pressure rise were improved. This can be qualitatively explained considering the following two points:

1. The flame propagation in CVE experiment is defined by both ignition and burn rate of the ignited particles. A strong reduction in the ignition temperature, as illustrated in Figure 6.5, can lead to a more readily established flame propagation in the vessel and thus increase in both $P_{max}$ and $dP/dt_{max}$.
2. Combustion in the vessel occurs in a fuel-rich environment and particles may be competing for oxidizer, unlike the single, laser-ignited particle experiment, where oxidizer is plentiful. Mixing of the oxidizer may be noticeably enhanced by release of the cyclooctane from the particle surfaces which does not happen for

the case of pure Al.

## 6.6 Conclusions

Nearly pure aluminum particles with a modified surface were prepared by cryomilling aluminum and cyclooctane (a liquid at room temperature but solid at the liquid nitrogen temperature used during milling). Despite a small quantity of hydrocarbon (~2 wt. %) added to the metal, not only oxidation and ignition but also combustion characteristics of the prepared powder are significantly different from those of pure aluminum. The differences appear to be attributed to the unique morphology of the prepared powders. Al-cyclooctane powder oxidizes at a substantially lower temperature; its first oxidation step is much stronger and faster compared to that observed for a pure Al powder with the same particle sizes. Ignition temperatures are also substantially reduced compared to Al. It is suggested that the combined and inter-dependent effects of release of the volatile hydrocarbon additive and oxidation of the generated unpassivated surface lead to an improved ignition for the prepared material. For aerosolized powder clouds, ignition delay is shortened, and both combustion temperature and burn rate are improved compared to pure Al. For the individual composite particle combustion in air, burn time is longer, combustion temperature is comparable, and AlO emission is lower compared to Al. This is interpreted by suggesting a stronger role of surface reaction processes for the prepared composite particles. For composite particles burning in a hydrocarbon flame,

burn times are shorter compared to the pure Al, most likely due to the surface area increased as a result of release of a volatile hydrocarbon coating and available for the reaction. The effect of particle size on burn time in the latter case is approximately described by a $d^{1/2}$ law.

# CHAPTER 7

# CONCLUSIONS AND FUTURE WORK

## 7.1 Conclusions

Cryomilling has been successfully applied to prepare new aluminum-based materials comprising an aluminum matrix with iodine and hydrocarbon inclusions. The prepared Al-$I_2$ composite powders are effective in neutralizing spores or bacteria based on the results of biological experiments from University of Cincinnati. The prepared Al-hydrocarbon composites were found to have strong potential in replacing pure aluminum as fuel additive

As presented in Chapter 2, micron-sized, stable Al-$I_2$ composite powders were prepared using mechanical milling. In such compounds, iodine is chemically bound to Al and is stabilized to higher temperatures compared to elemental iodine and $AlI_3$. In addition to poorly crystalline $AlI_3$, other iodine compounds were contained in the mechanically alloyed powders. Milling conditions are adjusted to in order to obtain desired composites with different iodine concentrations, and to observe the effects of milling parameters on material properties. Milling at liquid nitrogen temperature is more effective in preparing stabilized Al-$I_2$ compounds than milling at room temperature. Milling directly in liquid nitrogen is more effective in producing equiaxial and/or smaller particle size; however the iodine is not well stabilized in the powders prepared in the

liquid nitrogen bath. In fully stabilized mechanically alloyed samples, most of iodine was incorporated into Al matrix as a stable phase which is released after the material was heated above 673 K (400 ºC).

A detailed study of iodine release and oxidation kinetics is reported in Chapter 3. The TGA measurements suggest that iodine is present in the prepared composites in at least three different forms. Two weakly bound forms volatilize similarly to elemental iodine and $AlI_3$. A strongly bound form is retained in aluminum until the material is heated up to nearly the Al melting point. Two different samples prepared in this effort contained different fractions of weakly and strongly bound iodine forms; however, the iodine release and oxidation behaviors were qualitatively similar for both samples. Oxidation of the prepared materials in TGA shows that the low-temperature oxidation begins sooner than for pure aluminum, and the second oxidation step is accelerated by Al melting unlike for pure aluminum oxidizing in $O_2$. Study of reaction kinetics indicates that the second oxidation step likely correlates with the release of strongly-bound form of iodine, and the ignition kinetics correlates well with that of the low-temperature release of iodine. Ignition of the prepared composites occurs at substantially lower temperatures than for pure Al.

A study of oxidation, ignition and combustion behaviors of Al-$I_2$ composites is presented in Chapter 4. Material prepared with increased iodine concentrations shift their first oxidation step to lower temperatures. Both overall iodine concentration and its

stability in the Al matrix are observed to affect ignition and combustion characteristics of the Al-$I_2$ composite powders. Qualitatively, greater iodine concentrations lower ignition temperatures but do not affect the combustion temperatures substantially. Burn times of individual Al-$I_2$ composite particles are slightly longer and their combustion temperatures are somewhat lower compared to the pure Al. However, improvements in both rate of pressure rise and maximum pressure were observed in constant volume explosion tests with powders containing 15 and 20 wt. % of $I_2$. The composite with 20 wt. % of $I_2$ with fairly good stability and fast oxidation and combustion rates is considered as the optimized drop-in replacement for pure aluminum powder in aluminized explosives expected to provide biocidal effects.

Preparation of Al-solid hydrocarbon composites, their characterization and study of their oxidation, ignition and combustion behaviors are discussed in Chapter 5. Unlike iodine, hydrocarbons are not altered chemically while being embedded in aluminum matrix. Upon heating, they volatilize at their characteristic volatilization temperatures. For both Al-wax and Al-polyethylene (PE) prepared materials, their ignition temperatures are reduced substantially compared to pure aluminum. Al-hydrocarbon materials oxidize at substantially lower temperatures and noticeably faster compared to pure Al powders. Individual particle burn times are longer, the combustion temperatures are similar, and values of AlO emission are lower for Al-hydrocarbon particles compared to Al. For aerosolized powder clouds, burn rates for the Al-wax or Al-PE composite are

comparable to that of pure Al. It is speculated that the combustion performance is reduced by the agglomeration observed for the partially burned particles of Al-hydrocarbon composites in the CVE configuration.

In order to improve overall energy density and combustion rate for aerosolized powders, liquid cyclooctane was used to prepare composites in Chapter 6. Nearly pure aluminum particles with a modified surface were prepared by cryomilling aluminum with cyclooctane. Despite a small quantity of hydrocarbon (~2 wt. %) added to the metal, not only oxidation and ignition but also combustion characteristics of the prepared powder are significantly different from those of pure aluminum. Al-cyclooctane powder oxidizes at a substantially lower temperature; its first oxidation step is much stronger and faster compared to that observed for a pure Al powder with the same particle sizes. Ignition temperatures are also substantially reduced compared to Al. For aerosolized powder clouds, ignition delay is shortened, and both combustion temperature and burn rate are improved compared to pure Al.

## 7.2 Future Work

X-ray diffraction is used to analyze the phase in Al-$I_2$ and Al-hydrocarbon composites. For Al-$I_2$ materials, only Al and $AlI_3$ phases were observed. For Al-hydrocarbon, only Al phase is observed. It appears that XRD is ineffective to understand other possible phases, which may exist as thin layer on the surface of particles or lie between grain

boundaries of aluminum. Other analytical techniques such as TEM or XPS can be used to characterize the phase composition in these composite materials.

Al-$I_2$ composites are observed to perform well in neutralization of viable aerosolized microorganisms. It appears that the maximum iodine content for a practical, stable composition is about 20 wt. %. Preparation of a stable composition with higher iodine content may be possible with different starting materials. Moreover, the mechanism how the iodine release will affect the inactivation should be better understood. Thus, materials can be further optimized to obtain better biocidal effects.

Al-cyclooctane appears to be nearly pure aluminum with good ignition and combustion performance. Results show that the improved ignition behavior may be due to an increase in surface area upon heating. Further investigation can be performed to observe whether cyclooctane has chemically altered the aluminum surface. In addition, it is of interest to optimize the material by milling Al with different hydrocarbons to reduce the milling time.

In the single particle combustion experiment, it appears that all the composites burn longer than aluminum. It is not clear whether they burn slower or more completely than aluminum. However, this question can be answered by collecting and analyzing the combustion products from single particle experiments. Furthermore, the burn times of these particles can be compared to Beckstead's results [93].

## APPENDIX A

## Al-Mg COMPOSITES WITH IMPROVED COMBUSTION RATE

In this appendix, the characterization results of Al-Mg composites are presented. Such materials were synthesized using cyclooctane as a process control agent. Milling parameters are the same as used in Chapter 6 except the starting materials and milling time.

**Table A.1** Al-Mg Samples Prepared in Attritor Mill

| Sample ID | Mass load, g | | | Milling time, h |
|---|---|---|---|---|
| | Al | Mg | hydrocarbon | |
| Al-cyclooctane | 45 | - | 5 | 19 |
| Al-Mg | 36 | 9 | 5 | 18 |

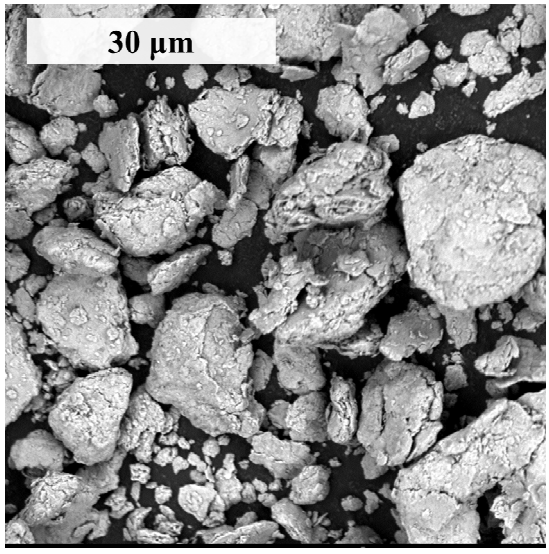


**Figure A.1** SEM image of Al-Mg composite.

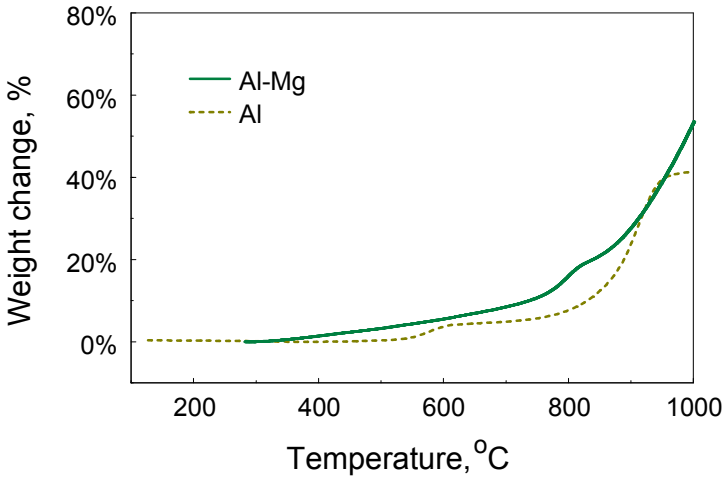


**Figure A.2** Oxidation traces of Al-Mg and reference Al at 5 K/min in TGA.

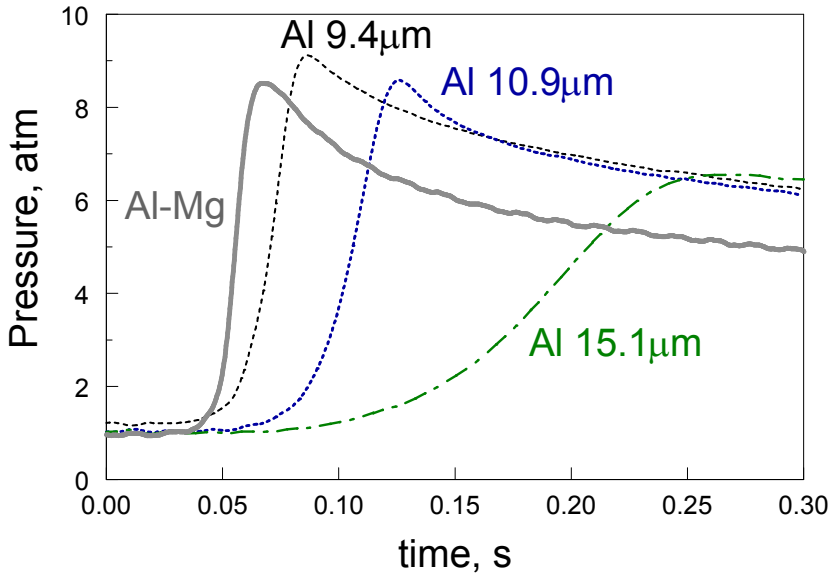


**Figure A.3** Pressure traces for Al-Mg composite powder and reference Al measured in CVE experiments. The experimental conditions are described in Chapter 6.

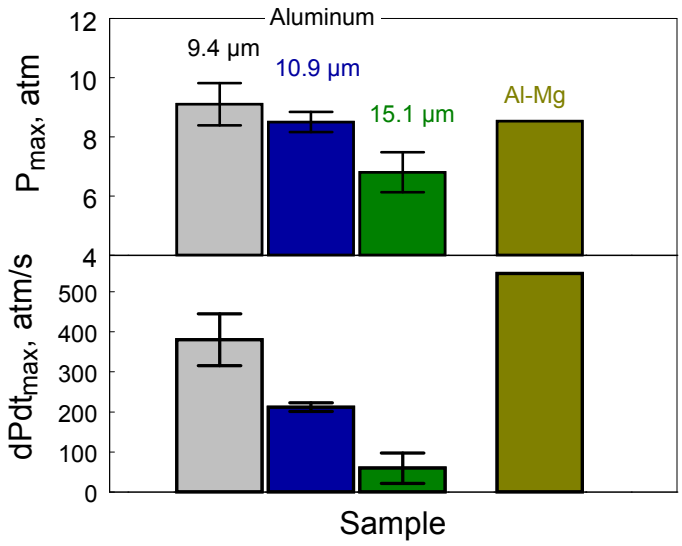


**Figure A.4** Maximum pressure and maximum rate of pressure rise for Al-Mg composites and reference Al measured in CVE experiments. The experimental conditions are described in Chapter 6.

## APPENDIX B

## MASS SPECTRUM OF $I_2$ AND Al-$I_2$ COMPOSITES

Mass spectrometer (MS) was used to characterize products for both iodine and Al-$I_2$ composites upon heating. Elemental iodine was heated up to 353 K (80 ºC) by a plate heater. It was exposed to ambient air during the MS measurement. Al-$I_2$ composites were heated in a Netzsch DSC STA409PC furnace using a heating rate of 20K/min. Mass spectrometer was connected to the outlet of furnace to analyze the products.

It was observed that solid iodine tends to absorb moisture and turns into a liquid phase quickly. It is very likely that iodine reacts with water to produce HI and HIO according to the chemistry. However, MS results of elemental $I_2$ showed only I and HI fragments. Similarly, only I and HI fragments were observed for Al-$I_2$ composites.

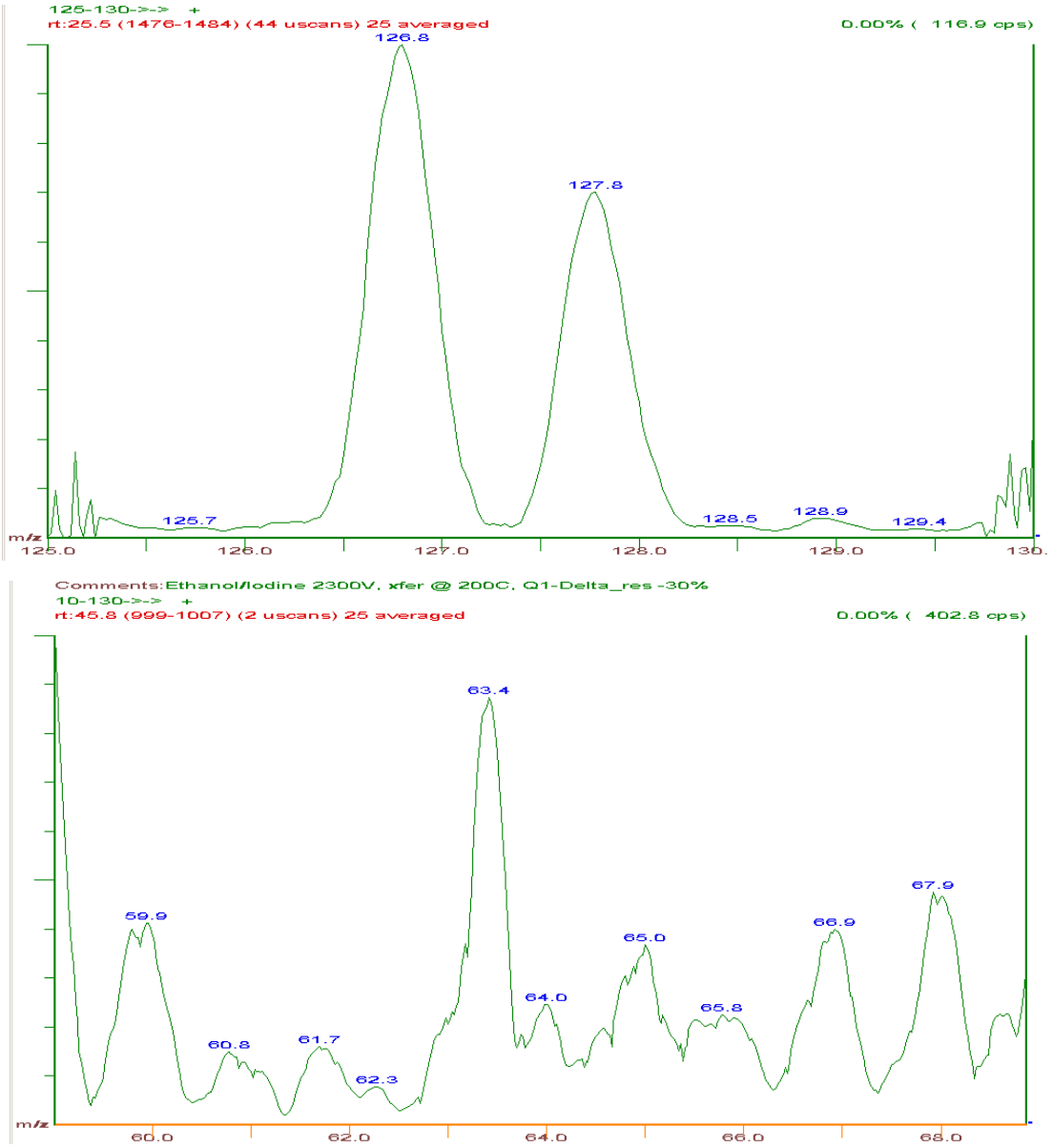


**Figure B.1** Characteristic peaks in mass spectrum. The x-axis is mass to charge ratio, and the y-axis represents the intensity. 126.8 and 127.8 are the peaks for singly charged I and HI fragments, respectively; 63.4 is the peak for doubly charged I.

# APPENDIX C

## ADDITIONAL DATA FOR SINGLE PARTICLE EXPERIMENTS

Additional results of single particle experiment were presented for Al-$I_2$ samples investigated in Chapter 4. Particle size distributions, which are shown in Figure 4.1 are used to compare with that implied from the amplitudes of the scattered light pulses measured in this experiment. In the processing, the value of particle refraction coefficient was adjusted to achieve the best match between the two size distributions. Considering coarse particles are not well represented in the current combustion experiment, the best match was not based on that for the whole range of particle size, but actually based on that for the fine particles. Figure C.1 show the best matches chosen for different sample A, B, C and D. The match is not perfect for the whole range of particle size for each material, but salient features of the powder size distributions are represented well for sample A, B and D.

The measured emission time as a function of the particle diameter is shown in Figure C.2 for samples B, C and D; data points of sample A are not enough to make such result plot. Filled symbols in Figure C.2 represent particles with longest emission times. These longest times are selected following a consistent data processing routine [69, 70]. Thus, data represented by open symbols in Figure C.2 are removed from further analysis.

All emission traces selected as shown by filled symbols in Figure C.2 (including, in addition, traces for sample A) were processed to determine the average flame temperature and $R_{AlO}$. Results of flame temperature and $R_{AlO}$ are plotted as a function of particle size in Figure C.3 and Figure C.4, respectively.

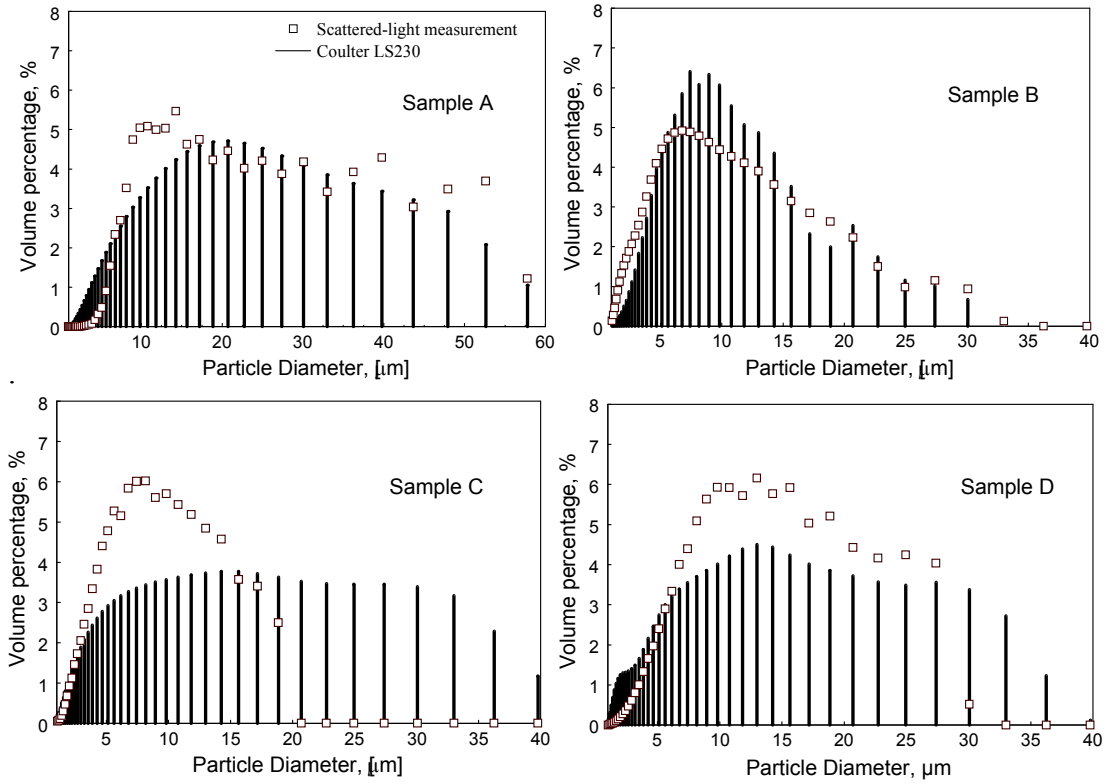


**Figure C.1** Particle size distribution measured in the commercial device (Coulter LS230) and the scattered-light measurement for Al-$I_2$ samples (cf. Chapter 4).

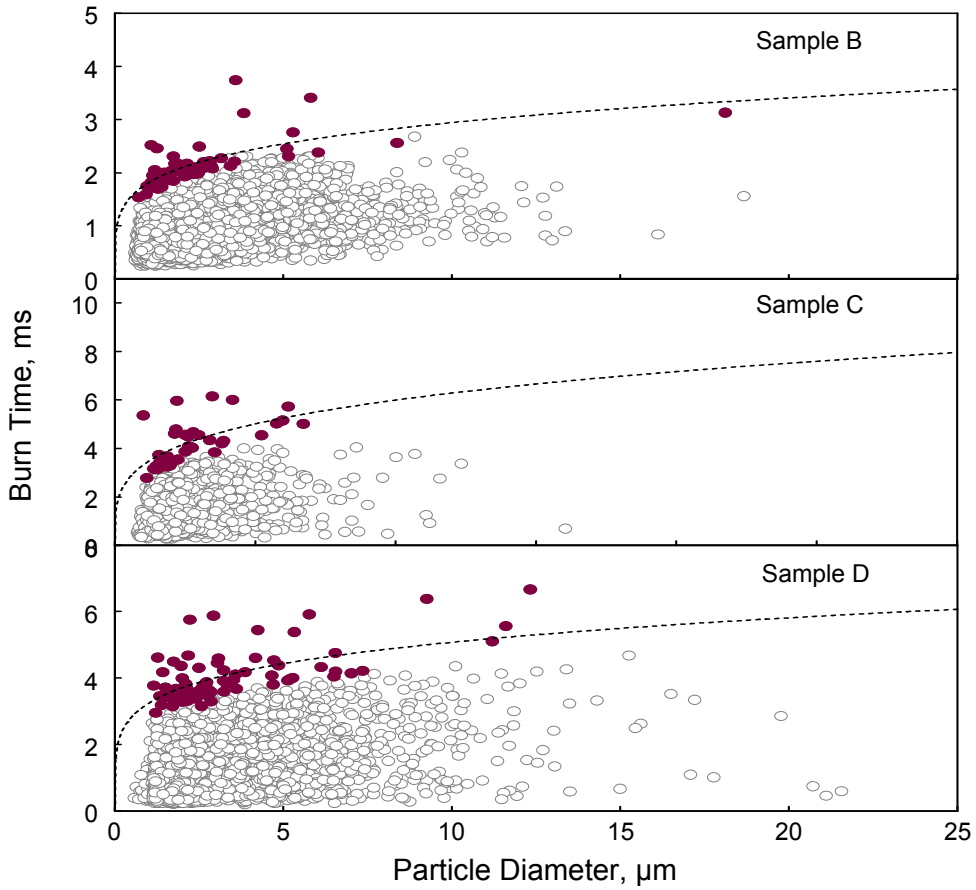


**Figure C.2** Burn times as a function of particle size for sample B, C and D (cf. Chapter 4) in air.

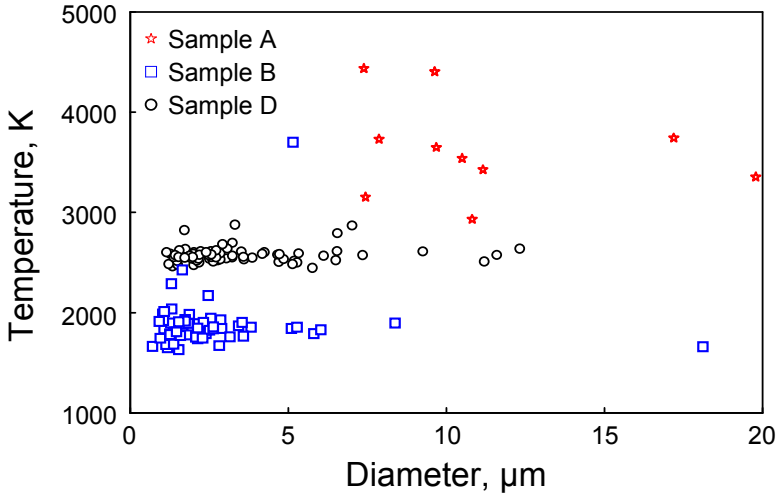


**Figure C.3** Measured flame temperatures for different Al-$I_2$ composites.

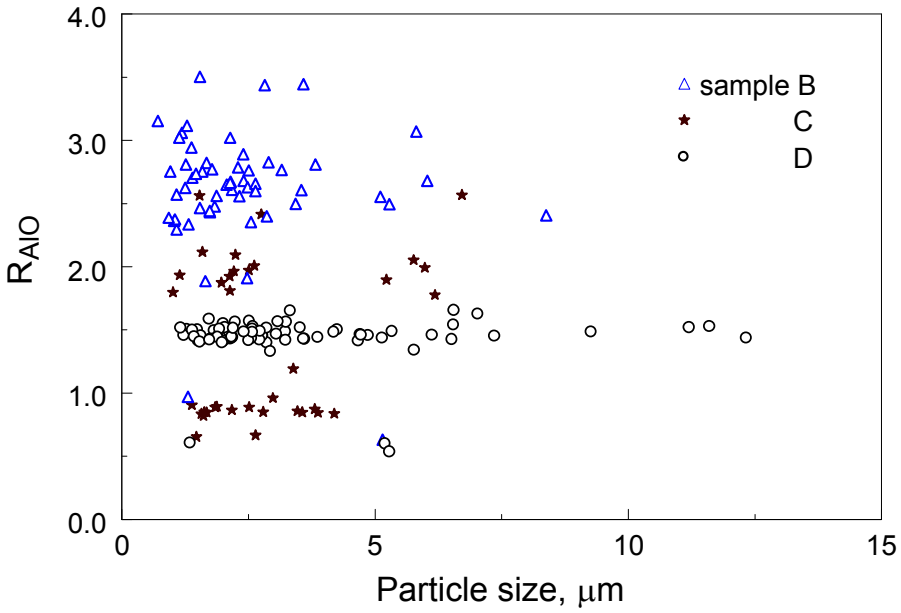


**Figure C.4** Measured AlO ratio for different Al-$I_2$ composites.

## APPENDIX D

## FLAME TEMPERATURE MEASUREMENT

Al-wax powders were seeded into an air-acetylene flame in a modified Bunsen burner [94]. Emission spectrum was measured at different heights of combustion flame. Flame temperature was determined by analyzing the emission spectrum.

**Figure D.1** Rotated photograph of air-acetylene flame with seeded Al-wax powders. Flame conditions were the same as for Al-cyclooctane in Chapter 6.

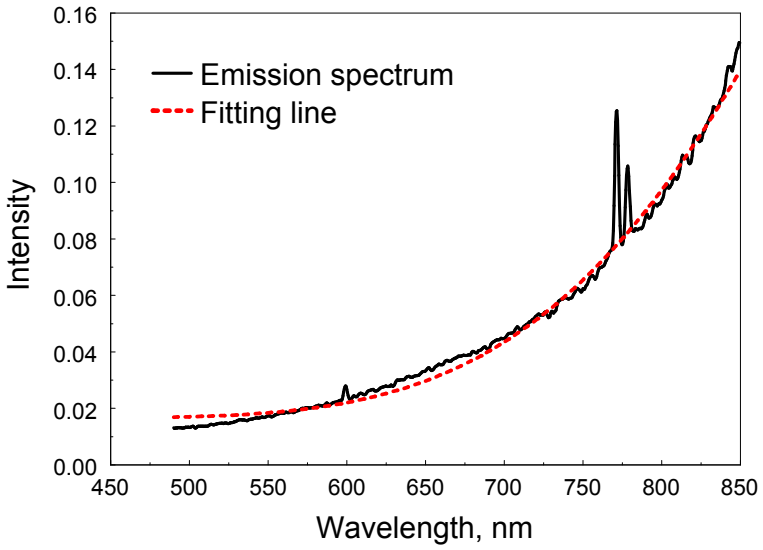


**Figure D.2** An example of measured spectrum and the fitting line for the obtained flame temperature. Note that three characteristic atomic lines appear in the spectrum.

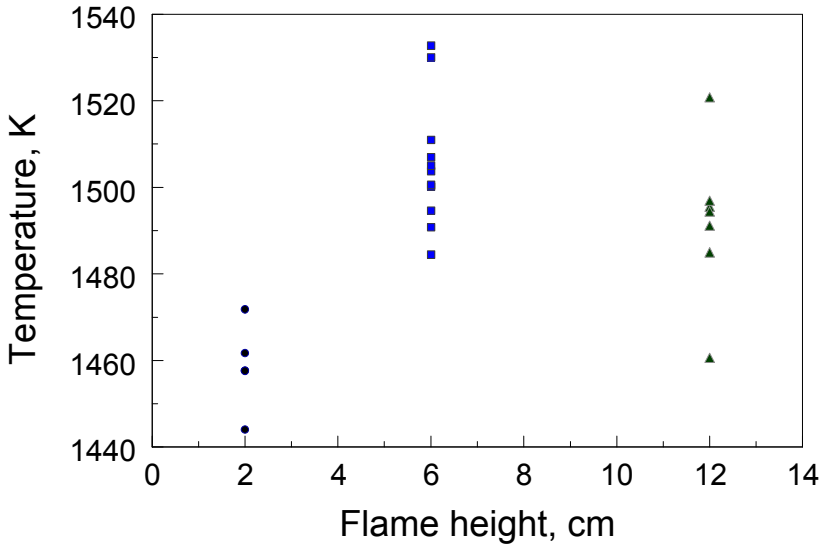


**Figure D.3** Flame temperatures at different flame heights.

# APPENDIX E

## HEAT LOSS FROM SINGLE PARTICLE COMBUSTION

The objective is to assess heat loss from individual particle during combustion assuming that there is no vapor flame surrounding the particle. The inputs for the calculation are temperature profile, burn time and particle size obtained from single particle experiment [66, 71]. In this assessment, the measured temperature was considered to be particle surface temperature. The heat loss was calculated considering the variation of both particle size and temperature during combustion.

Particle size evolution was calculated assuming that reduction of particle size follow the $d^{0.2}$ law, which is consistent with the result observed for Al-$I_2$ materials. The mass and heat transfer were considered to occur in a transition regime. The convection and radiation heat loss were evaluated according to ref. [95]. Emissivity was 0.8. The reaction enthalpies for Al and $I_2$ are 837,850 J/mole and 18,8361 J/mol, respectively. The total energy was obtained by assuming Al and iodine are fully oxidized.

Results showed that magnitude of convection is generally 1-2 orders larger than that of radiation. The ratio of heat loss over theoretical heat is plotted as a function of particle size for Al-$I_2$ samples (see Figure E.1) and Al particles (see Figure E.2). There is a significant fraction of small particles presented in Al-$I_2$ samples having the ratio larger than 1, which means that the heat loss was over estimated for these particles.

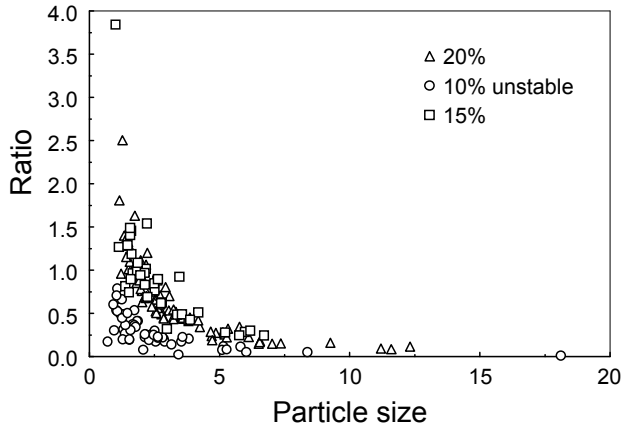


**Figure E.1** The ratio of heat loss over theoretical heat as a function of particle size for Al-$I_2$ materials.

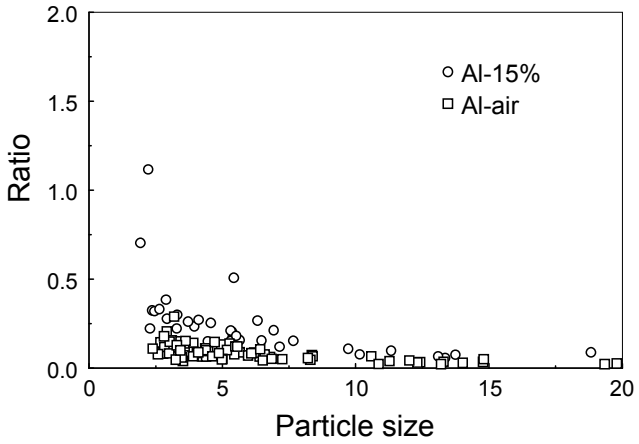


**Figure E.2** The ratio of heat loss over theoretical heat as a function of particle size for Al particles in different burning environment.

## APPENDIX F

## INACTIVATION OF AEROSOLIZED BIOLOGICAL SPORES

The prepared Al-$I_2$ composites were fed into a hydrocarbon flame in a modified Bunsen burner to evaluate their biocidal effect on Bacillus atrophaeus (BG) spores. The detailed results are available in ref. [94]. The inactivation of BG spores is studied with different composite materials, and the main results are shown in Figure F.1. A strong inactivation potential is observed for Al-$I_2$ composites. The experimental apparatus was designed at NJIT in collaboration with Prof. Grinshpun's group at University of Cincinnati. The experiments were conducted at University of Cincinnati.

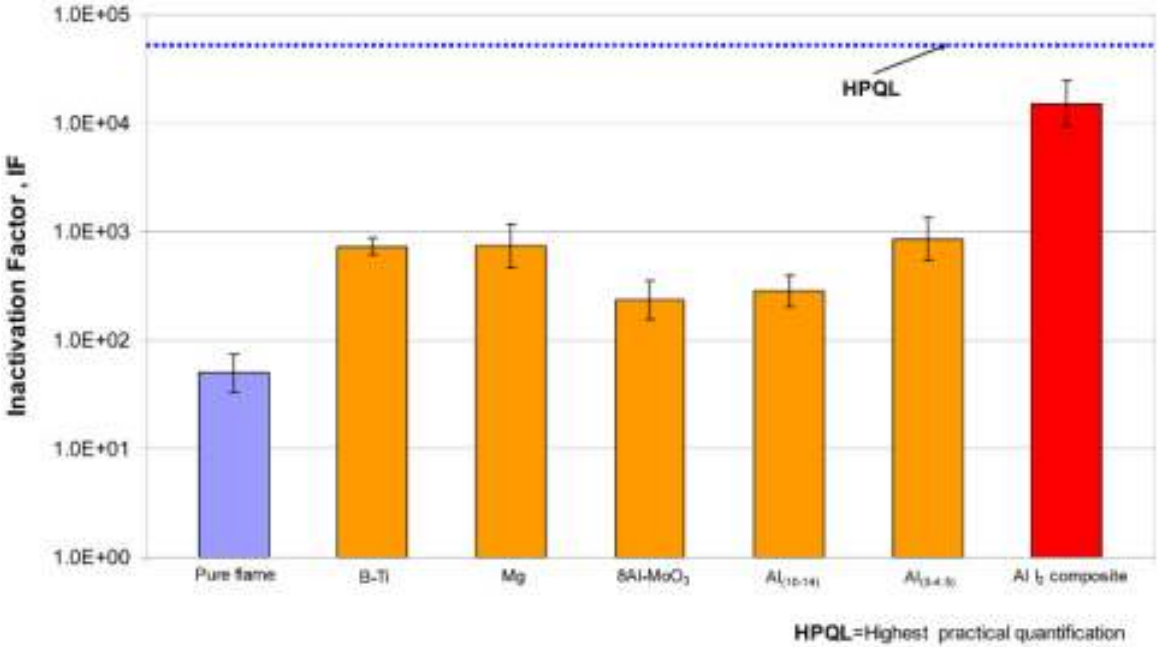


**Figure F.1** The inactivation of aerosolized Bacillus atrophaeus (BG) spores by combustion of different materials.

## REFERENCES


[1] J. P. Agrawal and J. E. Field, "Recent trends in high-energy materials," *Progress in Energy and Combustion Science,* vol. 24, pp. 1-30, 1998.

[2] P. F. Pagoria, G. S. Lee, A. R. Mitchell, and R. D. Schmidt, "A review of energetic materials synthesis," *Thermochimica Acta,* vol. 384, pp. 187-204, 2002.

[3] E. L. Dreizin, "Metal-based reactive nanomaterials," *Progress in Energy and Combustion Science,* vol. 35, pp. 141-167, 2009.

[4] U. R. Nair, S. N. Asthana, A. S. Rao, and B. R. Gandhe, "Advances in high energy materials," *Defence Science Journal,* vol. 60, pp. 137-151, 2010.

[5] A. S. Cumming, "New trends in advanced high energy materials," *Journal of Aerospace Technology and Management,* vol. 1, pp. 161-166, 2009.

[6] T. B. Brill and K. J. James, "Kinetics and mechanisms of thermal decomposition of nitroaromatic explosives," *Chemical Reviews,* vol. 93, pp. 2667-2692, 1993.

[7] D. M. Badgujar, M. B. Talawar, S. N. Asthana, and P. P. Mahulikar, "Advances in science and technology of modern energetic materials: An overview," *Journal of Hazardous Materials,* vol. 151, pp. 289-305, 2008.

[8] N. H. Yen and L. Y. Wang, "Reactive metals in explosives," *Propellants, Explosives, Pyrotechnics,* vol. 37, pp. 143-155, 2012.

[9] R. A. Yetter, G. A. Risha, and S. F. Son, "Metal particle combustion and nanotechnology," *Proceedings of the Combustion Institute,* vol. 32 II, pp. 1819-1838, 2009.

[10] V. I. Rozenband and N. I. Vaganova, "A strength model of heterogeneous ignition of metal particles," *Combustion and Flame,* vol. 88, pp. 113-118, 1992.

[11] E. L. Dreizin, "Phase changes in metal combustion," *Progress in Energy and Combustion Science,* vol. 26, pp. 57-78, 2000.

[12] E. L. Dreizin, "Effect of phase changes on metal particle combustion processes," *Combustion, Explosion and Shock Waves,* vol. 39, pp. 681-693, 2003.

[13] C. K. Law, "A simplified theoretical model for the vapor-phase combustion of metal particles," *Combustion Science and Technology,* vol. 7, pp. 197-212, 1973.

[14] P. W. Cooper, *Explosives engineering*. New York, NY: Wiley-VCH, 1996.

[15] C. Rossi, K. Zhang, D. Estève, P. Alphonse, P. Tailhades, and C. Vahlas, "Nanoenergetic materials for MEMS: A review," *Journal of Microelectromechanical Systems,* vol. 16, pp. 919-931, 2007.

[16] R. J. Jouet, A. D. Warren, D. M. Rosenberg, V. J. Bellitto, K. Park, and M. R. Zachariah, "Surface passivation of bare aluminum nanoparticles using perfluoroalkyl carboxylic acids," *Chemistry of Materials,* vol. 17, pp. 2987-2996, 2005.

[17] S. W. Chung, E. A. Guliants, C. E. Bunker, D. W. Hammerstroem, Y. Deng, M. A. Burgers, P. A. Jelliss, and S. W. Buckner, "Capping and passivation of aluminum nanoparticles using alkyl-substituted epoxides," *Langmuir,* vol. 25, pp. 8883-8887, 2009.

[18] J. Sun, M. L. Pantoya, and S. L. Simon, "Dependence of size and size distribution on reactivity of aluminum nanoparticles in reactions with oxygen and MoO3," *Thermochimica Acta,* vol. 444, pp. 117-127, 2006.

[19] M. L. Pantoya and J. J. Granier, "Combustion behavior of highly energetic thermites: Nano versus micron composites," *Propellants, Explosives, Pyrotechnics,* vol. 30, pp. 53-62, 2005.

[20] J. J. Granier and M. L. Pantoya, "Laser ignition of nanocomposite thermites," *Combustion and Flame,* vol. 138, pp. 373-383, 2004.

[21] K. B. Plantier, M. L. Pantoya, and A. E. Gash, "Combustion wave speeds of nanocomposite Al/Fe2O3: The effects of Fe2O3 particle synthesis technique," *Combustion and Flame,* vol. 140, pp. 299-309, 2005.

[22] V. E. Sanders, B. W. Asay, T. J. Foley, B. C. Tappan, A. N. Pacheco, and S. F. Son, "Reaction propagation of four nanoscale energetic composites (Al/M0O3, Al/WO3, Al/CuO, and Bi2O3)," *Journal of Propulsion and Power,* vol. 23, pp. 707-714, 2007.

[23] Y. L. Shoshin, R. S. Mudryy, and E. L. Dreizin, "Preparation and characterization of energetic Al-Mg mechanical alloy powders," *Combustion and Flame,* vol. 128, pp. 259-269, 2002.

[24] Y. L. Shoshin and E. L. Dreizin, "Particle combustion rates for mechanically alloyed Al-Ti and aluminum powders burning in air," *Combustion and Flame,* vol. 145, pp. 714-722, 2006.

[25] Y. Aly, M. Schoenitz, and E. L. Dreizin, "Aluminum-metal reactive composites," *Combustion Science and Technology,* vol. 183, pp. 1107-1132, 2011.

[26] C. E. Aumann, G. L. Skofronick, and J. A. Martin, "Oxidation behavior of aluminum nanopowders," *Journal of Vacuum Science and Technology B: Microelectronics and Nanometer Structures,* vol. 13, pp. 1178-1183, 1995.

[27] B. J. Henz, T. Hawa, and M. R. Zachariah, "On the role of built-in electric fields on the ignition of oxide coated nanoaluminum: Ion mobility versus fickian diffusion," *Journal of Applied Physics,* vol. 107, pp. 024901-1-024901-9, 2010.

[28] S. Valliappan, J. Swiatkiewicz, and J. A. Puszynski, "Reactivity of aluminum nanopowders with metal oxides," *Powder Technology,* vol. 156, pp. 164-169, 2005.

[29] K. Sullivan and M. R. Zachariah, "Simultaneous pressure and optical measurements of nanoaluminum thermites: Investigating the reaction mechanism," *Journal of Propulsion and Power,* vol. 26, pp. 467-472, 2010.

[30] M. Schoenitz, T. S. Ward, and E. L. Dreizin, "Fully dense nano-composite energetic powders prepared by arrested reactive milling," *Proceedings of the Combustion Institute,* vol. 30 II, pp. 2071-2078, 2005.

[31] D. Stamatis, Z. Jiang, V. K. Hoffmann, M. Schoenitz, and E. L. Dreizin, "Fully dense, aluminum-rich Al-CuO nanocomposite powders for energetic formulations," *Combustion Science and Technology,* vol. 181, pp. 97-116, 2009.

[32] S. M. Umbrajkar, S. Seshadri, M. Schoenitz, V. K. Hoffmann, and E. L. Dreizin, "Aluminum-rich Al-MoO3 nanocomposite powders prepared by arrested reactive milling," *Journal of Propulsion and Power,* vol. 24, pp. 192-198, 2008.

[33] C. Suryanarayana, "Recent developments in mechanical alloying," *Reviews on Advanced Materials Science,* vol. 18, pp. 203-211, 2008.

[34] C. Suryanarayana, "Mechanical alloying and milling," *Progress in Materials Science,* vol. 46, pp. 1-184, 2001.

[35] X. Zhu, M. Schoenitz, and E. L. Dreizin, "Oxidation of mechanically alloyed Al-rich Al-Ti powders," *Oxidation of Metals,* vol. 65, pp. 357-376, 2006.

[36] X. Zhu, M. Schoenitz, and E. L. Dreizin, "Mechanically alloyed Al-Li powders," *Journal of Alloys and Compounds,* vol. 432, pp. 111-115, 2007.

[37] M. Schoenitz and E. L. Dreizin, "Structure and properties of Al-Mg mechanical alloys," *Journal of Materials Research,* vol. 18, pp. 1827-1836, 2003.

[38] C. L. Yeh and K. K. Kuo, "Ignition and combustion of boron particles," *Progress in Energy and Combustion Science,* vol. 22, pp. 511-541, 1996.

[39] T. M. Tillotson, A. E. Gash, R. L. Simpson, L. W. Hrubesh, J. H. Satcher Jr, and J. F. Poco, "Nanostructured energetic materials using sol-gel methodologies," *Journal of Non-Crystalline Solids,* vol. 285, pp. 338-345, 2001.

[40] A. Prakash, A. V. McCormick, and M. R. Zachariah, "Synthesis and reactivity of a super-reactive metastable intermolecular composite formulation of Al/KMnO4," *Advanced Materials,* vol. 17, pp. 900-903, 2005.

[41] S. Apperson, R. V. Shende, S. Subramanian, D. Tappmeyer, S. Gangopadhyay, Z. Chen, K. Gangopadhyay, P. Redner, S. Nicholich, and D. Kapoor, "Generation of fast propagating combustion and shock waves with copper oxide/aluminum nanothermite composites," *Applied Physics Letters,* vol. 91, pp. 243109-1-243109-3, 2007.

[42] E. J. Lavernia, B. Q. Han, and J. M. Schoenung, "Cryomilled nanostructured materials: Processing and properties," *Materials Science and Engineering A,* vol. 493, pp. 207-214, 2008.

[43] D. B. Witkin and E. J. Lavernia, "Synthesis and mechanical behavior of nanostructured materials via cryomilling," *Progress in Materials Science,* vol. 51, pp. 1-60, 2006.

[44] C. Badiola, M. Schoenitz, X. Zhu, and E. L. Dreizin, "Nanocomposite thermite powders prepared by cryomilling," *Journal of Alloys and Compounds,* vol. 488, pp. 386-391, 2009.

[45] G. Amitai, H. Murata, J. D. Andersen, R. R. Koepsel, and A. J. Russell, "Decontamination of chemical and biological warfare agents with a single multi-functional material," *Biomaterials,* vol. 31, pp. 4417-4425, 2010.

[46] M. A. Hobosyan, A. Kazansky, and K. S. Martirosyan, "Nanoenergetic composite based on I2O5/Al for biological agent defeat," in *Technical Proceedings of the 2012 NSTI Nanotechnology Conference and Expo*, Santa Clara, CA, 2012, pp. 599-602.

[47] C. Farley and M. Pantoya, "Reaction kinetics of nanometric aluminum and iodine pentoxide," *Journal of Thermal Analysis and Calorimetry,* vol. 102, pp. 609-613, 2010.

[48] S. A. Grinshpun, A. Adhikari, C. Li, T. Reponen, M. Yermakov, M. Schoenitz, E. Dreizin, M. Trunov, and S. Mohan, "Thermal inactivation of airborne viable Bacillus subtilis spores by short-term exposure in axially heated air flow," *Journal of Aerosol Science,* vol. 41, pp. 352-363, 2010.

[49] S. A. Grinshpun, C. Li, A. Adhikari, M. Yermakov, T. Reponen, M. Schoenitz, E. Dreizin, V. Hoffmann, and M. Trunov, "Method for studying survival of airborne

viable microorganisms in combustion environments: Development and evaluation," *Aerosol and Air Quality Research,* vol. 10, pp. 414-424, 2010.

[50] M. Schoenitz and E. Dreizin, "Oxidation processes and phase changes in metastable Al-Mg alloys," *Journal of Propulsion and Power,* vol. 20, pp. 1064-1068, 2004.

[51] Y. L. Shoshin, M. A. Trunov, X. Zhu, M. Schoenitz, and E. L. Dreizin, "Ignition of aluminum-rich Al-Ti mechanical alloys in air," *Combustion and Flame,* vol. 144, pp. 688-697, 2006.

[52] R. H. Chen, C. Suryanarayana, and M. Chaos, "Combustion characteristics of mechanically alloyed ultrafine-grained Al-Mg powders," *Advanced Engineering Materials,* vol. 8, pp. 563-567, 2006.

[53] M. Gugelchuk, *Encyclopedia of Reagents for Organic Synthesis*. New York, NY: John Wiley & Sons, 2001.

[54] J. D. Corbett and S. von Winbush, "The solubility of some metals in their molten halides1," *Journal of the American Chemical Society,* vol. 77, pp. 3964-3966, 1955.

[55] T. S. Ward, M. A. Trunov, M. Schoenitz, and E. L. Dreizin, "Experimental methodology and heat transfer model for identification of ignition kinetics of powdered fuels," *International Journal of Heat and Mass Transfer,* vol. 49, pp. 4943-4954, 2006.

[56] S. Vyazovkin, "Modification of the integral isoconversional method to account for variation in the activation energy," *Journal of Computational Chemistry,* vol. 22, pp. 178-183, 2001.

[57] M. J. Starink, "The determination of activation energy from linear heating rate experiments: A comparison of the accuracy of isoconversion methods," *Thermochimica Acta,* vol. 404, pp. 163-176, 2003.

[58] S. M. Umbrajkar, C. M. Chen, M. Schoenitz, and E. L. Dreizin, "On problems of isoconversion data processing for reactions in Al-rich Al-MoO3 thermites," *Thermochimica Acta,* vol. 477, pp. 1-6, 2008.

[59] S. M. Umbrajkar, M. Schoenitz, and E. L. Dreizin, "Exothermic reactions in Al-CuO nanocomposites," *Thermochimica Acta,* vol. 451, pp. 34-43, 2006.

[60] S. Zhang, M. Schoenitz, and E. L. Dreizin, "Mechanically alloyed Al-I composite materials," *Journal of Physics and Chemistry of Solids,* vol. 71, pp. 1213-1220, 2010.

[61] M. A. Trunov, M. Schoenitz, and E. L. Dreizin, "Effect of polymorphic phase transformations in alumina layer on ignition of aluminium particles," *Combustion Theory and Modelling,* vol. 10, pp. 603-623, 2006.

[62] M. A. Trunov, M. Schoenitz, X. Zhu, and E. L. Dreizin, "Effect of polymorphic phase transformations in Al2O3 film on oxidation kinetics of aluminum powders," *Combustion and Flame,* vol. 140, pp. 310-318, 2005.

[63] M. Schoenitz, C. M. Chen, and E. L. Dreizin, "Oxidation of aluminum particles in the presence of water," *Journal of Physical Chemistry B,* vol. 113, pp. 5136-5140, 2009.

[64] K. S. Martirosyan, L. Wang, and D. Luss, "Novel nanoenergetic system based on iodine pentoxide," *Chemical Physics Letters,* vol. 483, pp. 107-110, 2009.

[65] B. R. Clark and M. L. Pantoya, "The aluminium and iodine pentoxide reaction for the destruction of spore forming bacteria," *Physical Chemistry Chemical Physics,* vol. 12, pp. 12653-12657, 2010.

[66] S. Zhang, M. Schoenitz, and E. L. Dreizin, "Iodine release, oxidation, and ignition of mechanically alloyed Al-I composites," *Journal of Physical Chemistry C,* vol. 114, pp. 19653-19659, 2010.

[67] S. L. Vummidi, Y. Aly, M. Schoenitz, and E. L. Dreizin, "Characterization of fine nickel-coated aluminum powder as potential fuel additive," *Journal of Propulsion and Power,* vol. 26, pp. 454-460, 2010.

[68] P. R. Santhanam, V. K. Hoffmann, M. A. Trunov, and E. L. Dreizin, "Characteristics of aluminum combustion obtained from constant-volume explosion experiments," *Combustion Science and Technology,* vol. 182, pp. 904-921, 2010.

[69] R. J. Gill, S. Mohan, and E. L. Dreizin, "Sizing and burn time measurements of micron-sized metal powders," *Review of Scientific Instruments,* vol. 80, pp. 064101-1-064101-7, 2009.

[70] R. J. Gill, C. Badiola, and E. L. Dreizin, "Combustion times and emission profiles of micron-sized aluminum particles burning in different environments," *Combustion and Flame,* vol. 157, pp. 2015-2023, 2010.

[71] C. Badiola, R. J. Gill, and E. L. Dreizin, "Combustion characteristics of micron-sized aluminum particles in oxygenated environments," *Combustion and Flame,* vol. 158, pp. 2064-2070, 2011.

[72] C. Badiola and E. L. Dreizin, "On weak effect of particle size on its burn time for micron-sized aluminum powders," *Combustion Science and Technology,* vol. 184, pp. 1993-2007, 2012.

[73] S. Zhang, C. Badiola, M. Schoenitz, and E. L. Dreizin, "Oxidation, ignition, and combustion of Al·I2 composite powders," *Combustion and Flame,* vol. 159, pp. 1980-1986, 2012.

[74] B. Z. Eapen, V. K. Hoffmann, M. Schoenitz, and E. L. Dreizin, "Combustion of aerosolized spherical aluminum powders and flakes in air," *Combustion Science and Technology,* vol. 176, pp. 1055-1069, 2004.

[75] S. Mohan, L. Furet, and E. L. Dreizin, "Aluminum particle ignition in different oxidizing environments," *Combustion and Flame,* vol. 157, pp. 1356-1363, 2010.

[76] B. J. Henz, T. Hawa, and M. R. Zachariah, "Atomistic simulation of the aluminum nanoparticle oxidation mechanism," in *48th AIAA Aerospace Sciences Meeting*, Orlando, FL, 2010, p. 0336.

[77] S. Chowdhury, K. Sullivan, N. Piekiel, L. Zhou, and M. R. Zachariah, "Diffusive vs explosive reaction at the nanoscale," *Journal of Physical Chemistry C,* vol. 114, pp. 9191-9195, 2010.

[78] A. Rai, K. Park, L. Zhou, and M. R. Zachariah, "Understanding the mechanism of aluminium nanoparticle oxidation," *Combustion Theory and Modelling,* vol. 10, pp. 843-859, 2006.

[79] M. Schoenitz, B. Patel, O. Agboh, and E. L. Dreizin, "Oxidation of aluminum powders at high heating rates," *Thermochimica Acta,* vol. 507-508, pp. 115-122, 2010.

[80] W. K. Lewis, A. T. Rosenberger, J. R. Gord, C. A. Crouse, B. A. Harruff, K. A. S. Fernando, M. J. Smith, D. K. Phelps, J. E. Spowart, E. A. Guliants, and C. E. Bunker, "Multispectroscopic (FTIR, XPS, and TOFMS−TPD) investigation of the core−shell bonding in sonochemically prepared aluminum nanoparticles capped with oleic acid," *The Journal of Physical Chemistry C,* vol. 114, pp. 6377-6380, 2010.

[81] C. A. Crouse, C. J. Pierce, and J. E. Spowart, "Synthesis and reactivity of aluminized fluorinated acrylic (AlFA) nanocomposites," *Combustion and Flame,* vol. 159, pp. 3199-3207, 2012.

[82] Y. Yavor and A. Gany, "Analysis and improvement of aluminum combustion in solid propellants," in *52nd Israel Annual Conference on Aerospace Sciences* Tel-Aviv and Haifa, Israel, 2012, pp. 1310-1322.

[83] D. A. Yagodnikov and A. V. Voronetskii, "Experimental and theoretical study of the ignition and combustion of an aerosol of encapsulated aluminum particles," *Combustion, Explosion and Shock Waves,* vol. 33, pp. 49-55, 1997.

[84] J. Cheng, H. H. Hng, H. Y. Ng, P. C. Soon, and Y. W. Lee, "Improved thermal properties of Al powders coated with submicron-sized hollow nickel particles," *Journal of Materials Research,* vol. 24, pp. 3220-3225, 2009.

[85] C. Johnson, T. J. Foley, and K. T. Higa, "Influence of activating compounds on oxidation mechanisms of aluminum powders," *Material Research Society Proceeding,* vol. 896, pp. 159-164, 2005.

[86] E. A. Lebedeva, I. L. Tutubalina, V. A. Val'tsifer, V. N. Strel'nikov, S. A. Astaf'eva, and I. V. Beketov, "Agglomeration of the condensed phase of energetic condensed systems containing modified aluminum," *Combustion, Explosion and Shock Waves,* vol. 48, pp. 694-698, 2012.

[87] E. L. Dreizin, C. Badiola, S. Zhang, and Y. Aly, "Particle combustion dynamics of metal-based reactive materials " *International Journal of Energetic Materials and Chemical Propulsion,* vol. 10, pp. 297-319, 2011.

[88] A. L. Corcoran, Hoffmann, V.K., Dreizin, E.L., "Aluminum particle combustion in turbulent flames," *Combustion and Flame,* vol. 160, pp. 718-724, 2013.

[89] H. E. Kissinger, "Reaction kinetics in differential thermal analysis," *Analytical Chemistry,* vol. 29, pp. 1702-1706, 1957.

[90] B. J. McBride and S. Gordon, "Computer program for calculation of complex chemical equilibrium compositions and applications II. users manual and program description," NASA Glenn Research Center, Cleveland, OH1996.

[91] S. Zhang, M. Schoenitz, and E. L. Dreizin, "Oxidation, ignition and combustion of Al-hydrocarbon composite reactive powders," *International Journal of Energetic Materials and Chemical Propulsion,* vol. 11, pp. 353-373, 2012.

[92] P. Lynch, H. Krier, and N. Glumac, "A correlation for burn time of aluminum particles in the transition regime," *Proceedings of the Combustion Institute,* vol. 32, pp. 1887-1893, 2009.

[93] M. W. Beckstead, "Correlating aluminum burning times," *Combustion, Explosion and Shock Waves,* vol. 41, pp. 533-546, 2005.

[94] S. A. Grinshpun, A. Adhikari, M. Yermakov, T. Reponen, E. Dreizin, M. Schoenitz, V. Hoffmann, and S. Zhang, "Inactivation of aerosolized Bacillus atrophaeus (BG) endospores and MS2 viruses by combustion of reactive materials," *Environmental Science and Technology,* vol. 46, pp. 7334-7341, 2012.

[95] S. Mohan, M. A. Trunov, and E. L. Dreizin, "On possibility of vapor-phase combustion for fine aluminum particles," *Combustion and Flame,* vol. 156, pp. 2213-2216, 2009.